Grain boundary and Se diffusion investigations in CdSe-CdTe thin-film photovoltaics

TAGHREED FEHAID S ALTAMIMI

Grain boundary and Se diffusion investigations in CdSe-CdTe thin-film photovoltaics

Taghreed Fehaid S Altamimi

A thesis presented for the degree of Doctor of Philosophy

Department of Physics
Durham University
United Kingdom

April 2024

Grain boundary and Se diffusion investigations in CdSe-CdTe thin-film photovoltaics

Taghreed Fehaid S Altamimi

Abstract:

Cadmium telluride (CdTe) solar cells are a very attractive thin-film photovoltaic technology because of low-cost manufacturing and high light absorption coefficient. Electron hole pairs generated by photons absorbed in the solar cell have a finite lifetime, due to radiative or non-radiative recombination processes. One path towards increasing the efficiency of CdTe solar cells is to minimise non-radiative recombination at grain boundaries. This work aims to combine cathodoluminescence (CL) contrast (optoelectrical properties) and electron backscatter diffraction (structure properties) to investigate the effect of grain boundary misorientation on non-radiative recombination. At the range between 35°-55° misorientation angle, the CL contrast was significantly high, which indicates that those regular grain boundaries are strong non-radiative recombination centres. For coincident site lattices (CSL) such as $\Sigma 3$, $\Sigma 5$, $\Sigma 7$ and $\Sigma 9$ which have high symmetry, the CL contrast was much smaller, which means those special grain boundaries are not harmful to the device. The reduced recombination velocity was also measured, and the results shown to be consistent with the contrast measurements. Se diffusion from CdSe to CdTe by using standard and bevel cross-sections has also been investigated for two samples with different external quantum efficiency (EQE) and thicknesses (i.e. 100 and 400 nm) of the CdSe layer. The results showed that both devices have voids at the inter-diffusion layer, although for the 400 nm CdSe sample voids were more numerous. Rapid diffusion of Se along the CdTe grain boundaries led to small grains at the interface region, due to Kirkendall voids and solute pinning of the grain boundaries, which resulted in a lower EQE for the 400 nm CdSe device. Transmission electron microscopy (TEM) diffraction patterns confirmed a zinc blende cubic structure throughout the absorber layer, which suggests that the lower EQE is not due to a change in the crystal structure, as has previously been reported in the literature. The Se diffusion coefficient is calculated using scanning TEM energy dispersive X-ray (EDX). The diffusion coefficient measured is 7.2×10^{-12} cm^2/s, which is an order of magnitude smaller than the literature value.

Declaration

The work in this thesis is based on research carried out in the Department of Physics, Durham University, United Kingdom. No part of this thesis has been submitted elsewhere for any other degree or qualification and it is all my own work unless referenced to the contrary in the text.

List of publications

T.F.S. Altamimi, J.F. Leaver, J.D. Major, B.G. Mendis, "Combined CL and EBSD investigation of non-radiative grain boundary recombination in CdTe-CdSe thin-film photovoltaics", 40th European Photovoltaic Solar Energy Conference and Exhibition 2023. (DOI:10.4229/EUPVSEC2023/2CV.2.39 020132).

T.F.S. Altamimi, J.F. Leaver, K. Durose, J.D. Major, B.G. Mendis, "Se inter-diffusion limits absorber layer grain growth in CdSe-CdTe photovoltaics", Submitted to the journal.

Acknowledgements

In the name of Allah, the Most Gracious and the Most Merciful. Alhamdulillah, I am grateful to Allah for giving me the strength and blessings to complete this thesis. I want to express my immense gratitude to everyone who has supported me throughout the past four years of this journey.

First and foremost, I am indebted to my supervisor, Dr. Budhika Mendis, for his invaluable feedback and guidance. I am also thankful for his efforts in proofreading this thesis. I had the privilege of collaborating with Liverpool University and Cambridge University. I extend my thanks to Dr. Jon Major and Jacob for their assistance in developing the devices and providing necessary data. I also appreciate Dr. Gunnar at Cambridge University for his help in acquiring the TRCL data used in this work. Special thanks to Leon and David for their efforts in the lab, especially during challenging times.

I am grateful to Professor Basheer Alshammari for his constructive comments and suggestions throughout my PhD journey. I also acknowledge the valuable knowledge gained from postgraduate courses in the first year, thanks to Douglas Halliday, Fernando Dias, Aiden Hindmarch, and Halim Kusumaatmaje.

None of this would have been possible without the generous support from the Saudi government and Hail University. I am thankful to my colleagues Oliver, Roy, and Kaviya for their assistance and support. I also appreciate the librarians, research assistants, and study participants from the university who have inspired me.

I am grateful for the opportunity to work with Ustinov College as a resident tutor. Many thanks to Brenda Ryder and Gary Scaf at Ustinov College and Del Atkinson for being part of the inter-group committee in the physics department.

I must mention my family, especially my mother, who has been my constant source of support and guidance. Her prayers and love have been invaluable to me. I am also thankful to my children, Rayan and Sara, whose belief in me kept me motivated throughout this journey.

I extend my gratitude to my friends Refaa, Nouf, Suncice, and Aziza for their support and companionship. Special thanks to my dear friend Nuzhat for her assistance and encouragement.

The pages that follow are the result of countless hours of dedication over four years.

Contents

List of Figures

List of Tables

Chapter 1

Introduction

1.1 Photovoltaic Technology

In recent years the phenomenon of global warming has received attention all over the world by researchers. Since 1880 the average surface temperature has risen by about 1 °C (about 2 °F) [1]. Figure 1.1 shows the average annual global temperatures since 1880 to 2022. In 2019, Earth's global surface temperature was the second warmest year (the warmest year was in 2016) as recorded by NASA and the National Oceanic and Atmospheric Administration [1,2]. Climate issues have become increasingly important, especially since the last five years have been the warmest for the last 140 years [1].

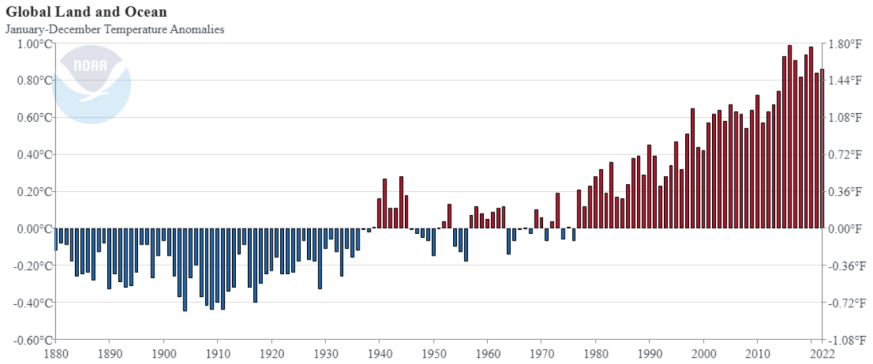

Figure 1.1: *Global surface temperature since 1880; here zero temperature represents the long-term average temperature for the whole planet; blue and red bars show the difference below or above average for each year [3]*

The most significant factor which led to this issue is increased levels of greenhouse gases in the atmosphere such as carbon dioxide. These gases are produced as a result of using fossil fuels such as oil, coal and gas [4]. In fact, there are many implications of this on the environment and health (e.g. water and air pollution) [5]. In order to reduce the impediments of the dependence on fossil fuels, there is a need to focus and improve renewable energy, especially solar cells, because solar energy compared with other renewable sources (e.g. wind and water) has the most amount of energy source from the sun [4].

Today solar power is cheaper than energy from traditional fossil fuels, in most parts of the world. (PV) technology is used to generate electricity, and many experts predict that by the middle of the century, PV systems will be used to produce a lot of energy. [6]. According to the technical characteristics, existing PV technologies can be divided into three generations.

Si wafer technology is the foundation for first-generation PV cells. This generation includes monocrystalline and polycrystalline silicon PV cells. These cells are all single-junction structures. The structure's theoretical maximum efficiency is around 33% [7]. In general, first-

generation PV cells last longer and are more efficient than other types of PV cells. However, their manufacturing process costs more in terms of energy consumption and time, due to the fact that silicon wafers are produced from sand (SiO_2) as a raw material, which is an energy intensive process with several stages of extraction, purification and preparation. Thin-film PV technology is used to manufacture second-generation PV cells (single-junction devices). The manufacturing cost consumption in terms of semiconductor material is significantly lower when compared to first-generation cells. They are made of very thin layers of semiconductor materials, as opposed to first-generation cells. These cells manufacturing processes are simple and use fewer materials, so they are less expensive than first-generation cells. Their efficiencies are however lower because of internal defects, such as grain boundaries [8].

Silicon is a semiconductor that is abundant on earth in the form of sand and is the foundation of the microelectronics industry that has produced computers, smartphones, and many other electronic devices. A single junction monocrystalline silicon cell achieved a record efficiency of 26.7% [9]. The process of making silicon solar panels requires growing very pure, large single crystals. Then, these crystals are cut into wafers and assembled into solar panels. This manufacturing process is costly and therefore, significant research is still needed to improve the efficiency and reduce the cost further [6].

Thin-film PV is being actively researched to resolve this cost challenge. The semiconductors are strongly light absorbing and can therefore be made thin (layer thickness of several micrometres). Furthermore, there are a variety of methods to deposit the thin-films cheaply and efficiently. This means that both capital and energy expenditures are low [6].Amorphous silicon (a-Si), copper indium gallium diselenide (CIGS), cadmium telluride (CdTe), and other materials are utilised to create thin film solar cells [10].

CdTe solar cells have become one of the most promising thin-film PV technologies, with increasing efficiency over time - in the 1980s, cells with efficiencies of around 10 % were common, and by the 1990s, efficiencies of around 15% were possible using a glass/SnO_2/CdS/CdTe structure [11]. More recently, solar cells with efficiencies of around 16.7% have been achieved using sputtered Cd_2SnO_4 and Zn_2SnO_4 for the transparent conducting oxide (TCO) layers [12]. Followed by the highest recorded efficiency of 22.1% by First Solar [6]. The most recent performance improvements resulted in part from improving the optical properties of the cell, getting rid of parasitic absorption in CdS, and adding a lower band gap CdSe as a window layer to get more light transimation into the absorber layer [13].

Although CdTe photovoltaic technology is now being produced on a large scale and has

levelized cost of electricity that is competitive with conventional electricity generation sources, there is still a significant amount of foundational research and development that must be done before this technology can realise its full potential [6]. CdTe is becoming a popular choice for roof-top solar systems and building-integrated photovoltaics. As an example, Figure 1.2 shows some of CdTe PV in Europe, Asia and the United States.

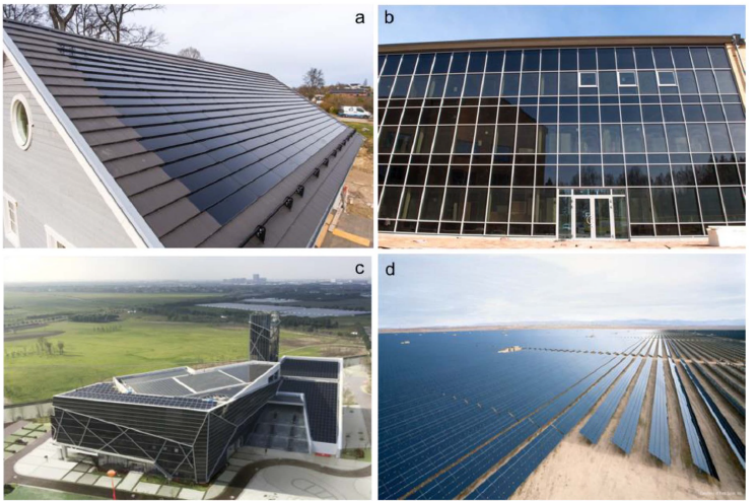

Figure 1.2: *(a) Houses with solar panels made from CdTe cells in Europe,(b) office building with semi-transparent CdTe panels in Europe. (C) Exhibition hall of artistic CdTe panels in Asia,(d) Topaz solar plant owned by BHE renewables in the United States. [6]*

Copper indium gallium selenide, Cu(In,Ga)Se_2 or CIGS, is another example of mainstream thin-film technology. In the mid 1970s, a single-crystal device with an efficiency of 12% was first reported [14]. Following this, CIGS thin-film absorbers, processing, and contacts have significantly improved, yielding 23.4% record cell efficiency [6]. The performance gap between an individual cell and module (comprising many cells) is not unique to CIGS. CIGS module production process is more complex than CdTe module production, since the ratio of indium to gallium must be carefully controlled in order to achieve the optimum band gap, or band gap grading within the absorber layer (alloying $CuInSe_2$ with Ga increases the band gap). The theoretical efficiency limit for CIGS with bandgap of 1.14 eV is 33.5% [15]. However, cell efficiency is predicted to reach as high as 25% in the near future [16].

Moreover, copper zinc tin sulfide (CZTS) is a new absorber material thin-film which has been explored. Like CIGS, CZTS has favourable optical and electronic properties, making it a good choice for thin-film solar panels. CZTS-based thin-film solar cells have been developing rapidly for the last ten years, reaching a record cell efficiency of 12.7% [17]. However, this conversion efficiency is relatively lower than the theoretical conversion efficiency limit of 32.2%. They are a potential low-cost replacement for CIGS cells. In addition, copper, zinc,

tin, and sulfur are sufficiently abundant elements on Earth and not toxic or harmful to the environment as other solar cells elements such as In and Ga in CIGS or Cd in CdTe [18].

The maximum theoretical efficiency limit for a single p-n junction solar cell was first calculated by William Shockley and Hans Quiesser [19]. They found the peak of the highest efficiency was around 30% with a bandgap between 1.3-1.5 eV. When using non-concentrated sunlight, a single solar cell's efficiency is constrained by the Shockley-Queisser limit. Accordingly, each photon with energy above the band gap will produce a single electron-hole pair, which will eventually thermalise to the band edges of the semiconductor. Therefore, some fraction of the absorbed photon energy is lost as heat, and will not produce electricity. To achieve the highest efficiency, a trade-off must be made between high short circuit current density (J_{sc}), which is attained by using a low band gap semiconductor that absorbs a larger portion of the incident solar spectrum, and high open circuit voltage (V_{oc}), which is attained by using a high band gap semiconductor that allows for a larger built-in voltage. Therefore to get the best performance from a semiconductor, there is a trade off that leads to an optimum band gap value. In light of this, the efficiency of a single junction solar cell can be calculated as a function of the absorber band gap for a specific solar spectrum. The maximum efficiency of converting light to electric power for AM 1.5G illumination is about 33% for band gaps in the range 1.3-1.5 eV [20].

The energy flow within the sun results in a surface temperature of around 5800 K, so the spectrum of the radiation from the sun is similar to that of a 6000 K blackbody. Gas molecules in the atmosphere absorb, scatter, and reflect solar radiation. The amount of radiation reaching the earth is less than what entered the top of the atmosphere. We can classify it into two categories, direct radiation which represents radiation from the sun that reaches the earth without scattering, and diffuse radiation which is scattered by the atmosphere and clouds. The amount of atmosphere that must be overcome before solar radiation reaches the surface of the Earth is represented by the air mass. When the sun is directly overhead at sea level, the air mass (AM) equals 1.0. We are particularly concerned with solar radiation that reaches the Earth surface, or terrestrial radiation. The American Society for Testing and Materials (ASTM) publishes three spectra - AM 0 (for space application), AM 1.5 Direct and AM 1.5 Global for a 37° tilted surface [21]. Figure 1.3 shows all these three solar spectra with black body spectrum at 6000 K.

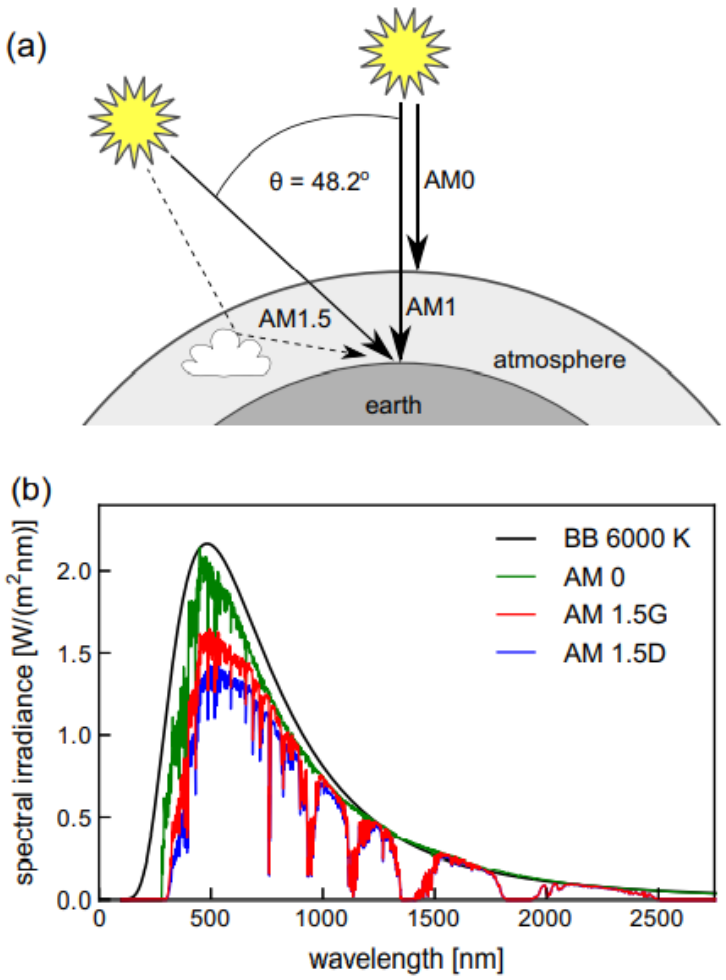

Figure 1.3: *(a) The spectral irradiance outside the Earth's atmosphere (AM 0) and on the Earth's surface for direct sunlight are shown by a solid arrow (AM 1.5). Also shown is the direct sunlight together with the scattered contribution from the atmosphere (solid and dashed arrow) at 48.2°incident angle. (AM 1.5G) (b) The spectral irradiance for AM0,1.5G and 1.5D, along with the black body spectrum at 6000 K temperature (BB6000 K). [20]*

1.2 Semiconductor Physics

When a large number of atoms come together to form a semiconductor, the atomic energy levels become reorganised into bands as the atoms interact, so that each energy band consists of many closely spaced energy levels. To explain the electrical properties of semiconductors, we need to consider two energy bands, the valence band, and the conduction band. For the material to conduct it must have electrons that are free to move within its conduction band or holes in its valence band. The difference in energy between the valence band and the conduction band is called the band gap. In insulators, the bandgap is large (>6 eV) and it is hard for the electron to be promoted from the valence band into the conduction band. However, in a semiconductor material, the bandgap is smaller (1-6 eV) and allows the

electrons from the valence band to transition to the conduction band, thereby increasing the conductivity [22].

1.2.1 Intrinsic or undoped semiconductors

At 0K temperature, all the outer electrons take part in covalent bonding. But we can increase the conductivity by heating; an electron can break the bond, and become free to move into the conduction bands, and this means the resistance of the material is reduced. The absence of the negative charge of an electron in the valence band leaves behind a positive charge (a hole). If the semiconductor is further heated more covalent bonds are broken resulting in more electrons jumping to the conduction band and more positive holes created in the valence band. So if the temperate of the semiconductor increases, the resistance is decreased and the conductivity increases, due to the higher concentration of charge carriers (electrons and holes). Since electrons and holes are both created during thermal generation the number of electrons and holes is equal. Therefore the Fermi level is located at approximately the middle of the band gap as shown in Figure 1.4(a).

1.2.2 Extrinsic or doped semiconductor

The conductivity can be altered by adding impurity atoms to the semiconductor. This can be done in two different ways. First doping with a group 5 impurity atom, such as arsenic (As), will result in an extra electron for a group 4 semiconductor, such as silicon. The energy level for the new extra electron, known as the donor level, will be in the band gap and specifically below the conduction band known as the donor level. The electrons in this level even at room temperature can gain enough energy to jump into the conduction band and contribute to the conductivity. The semiconductor is called an n-type extrinsic semiconductor, because the majority of the conduction is due to the negative electrons in the conduction band, Figure 1.4(b). Second, if the impurity atom is from group 3, such as indium (In), only three outer electrons are available for bonding with the silicon atoms. As a result, we will have a hole and a new energy level in the band gap that is located just above the valence band. This is called an acceptor level. The electrons in the valence band need only a small amount of energy (meV) to move to the acceptor level leaving a hole in the valence band. Here we have a p-type extrinsic semiconductor and the majority of charge carriers are positive holes. The conductivity in this type of semiconductor is due to the motion of the positive holes in the valence band, Figure 1.4(c). With a doped semiconductor, the electrons do not equal the

number of holes, as we see in an n-type semiconductor the majority of charge carriers are electrons, while in p-type semiconductors the majority of charge carriers are holes [23].

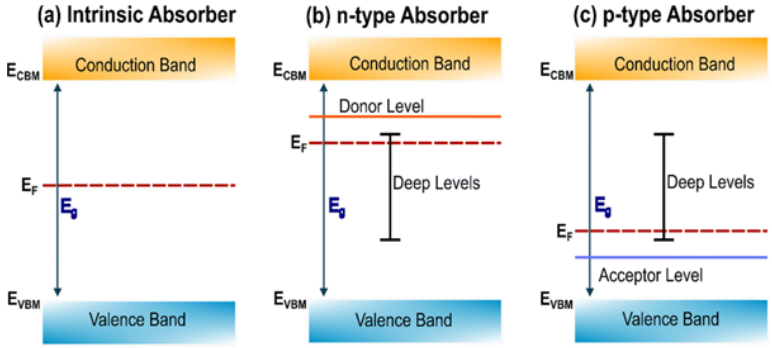

Figure 1.4: *The position of the Fermi level (E_F) relative to the valence band maximum (E_{VBM}) and conduction band minimum (E_{CBM}) for (a) intrinsic, (b) n-type and (c) p-type semiconductors, as well as the location of the donor and acceptor energy levels. [24]*

1.3 Thin-film solar cells

Solar cells or photovoltaic device materials rely on using sunlight for generating electricity [25]. It can absorb the light from the sun and convert it to electricity. This process occurs in many steps: after absorbing the photon via the material, the electron-hole pairs generated must be separated into free charge carriers by a built-in electric field. The free charge carries must then be collected by their respective electrodes to create the electric current [4, 26]. The way to fabricate the solar cell photovoltaic device is by using a semiconductor p-n junction [4].

Homojunction and heterojunction are both two types of p-n junction dependent on semiconductors that are used to form it. A homojunction is formed by two of the same semiconductor material with different doping, while a heterojunction is formed between two different semiconductors [23, 27] . The function of this junction is to flow the current in only one direction using a built-in electric field [23]. Consider the p and n-type semiconductors in contact. The majority carrier concentration gradient will cause diffusion. This means, majority carriers in p-type (holes) will diffuse to the n-side and the majority carriers in n type (electrons) will diffuse to the p-side. As the electrons and holes diffuse across the pn-junction they recombine, leaving no free electrons or free holes in the inter-diffusion region. When holes diffuse to the n-side it will leave negative ions (ionised acceptors) near the junction. On the other side, electrons diffused to the p-side will leave positive ions (ionised donors) near the junction. As shown in Figure 1.5 there are negative charges near the junction in p-side and there are

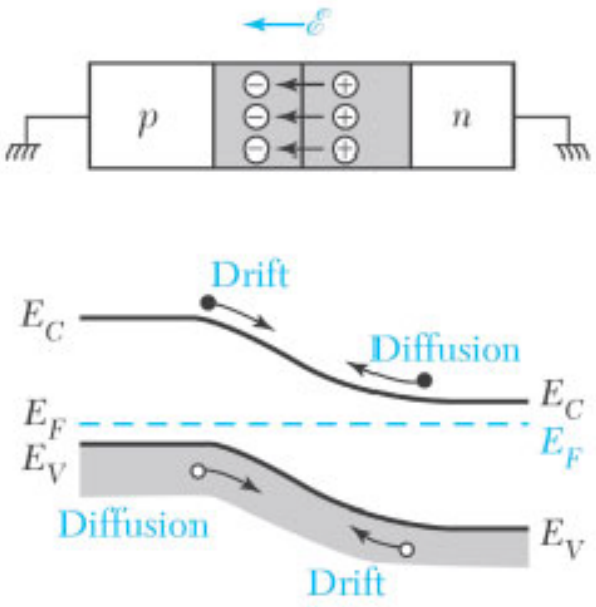

Figure 1.5: *p-n junction in thermal equilibrium (E_c: conduction band minimum , E_v: valence band maximum, E_F: Fermi level). [23]*

positive charges near the junction in n-type. This region is called the space charge region or depletion region. This will lead to an electric field from the positive side (n) to the negative side (p) [23]. There is also the built- in potential (diffusion potential) which describes the difference in the potential across the p-n junction [28].

At thermal equilibrium the drift current due to the electric field equals the diffusion current [23]. If forward bias is applied (positive voltage on p-side and negative voltage on n-side), the space charge region width and potential barrier will be decreased, so that a large current will flow across the junction. On the other hand, when reverse bias is applied (positive voltage on n-side and negative voltage on p-side), the space charge width and potential barrier will increase and there is very little current across the junction [23]. This is illustrated in Figure 1.6.

Solar cells absorb the light that is incident on the material; if the photon energy is bigger than the band gap of the material it can excite the electron from the valence band to the conduction band, leaving a hole in the valence band. This process to generate electrons and holes in the material is called photo-generation [28]. In a p-n heterojunction there are defects because of using two different semiconductor materials which may have different lattice parameters leading to strain at the interface [4]. These defects enhance the recombination between holes and electrons. Therefore, photo-generation creates charge carriers but some of these carries will be lost due to recombination, which can take place at the p-n junction as

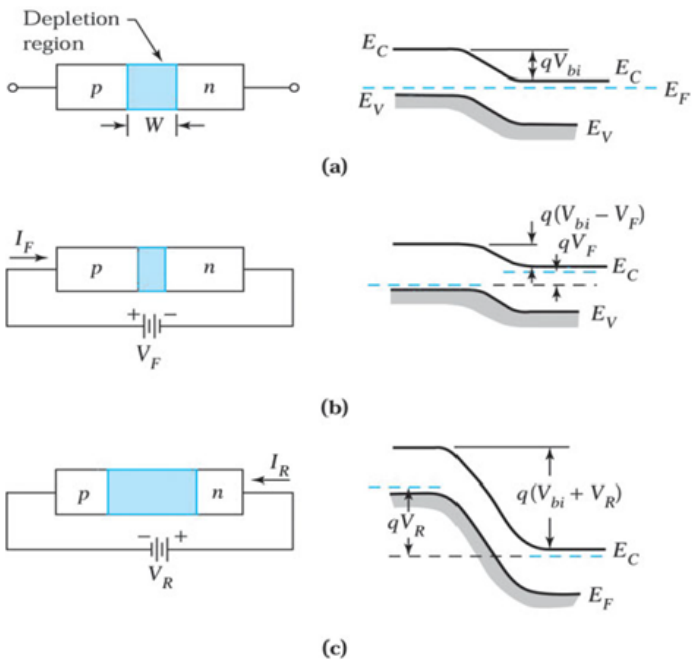

Figure 1.6: *p-n junction in (a) thermal equilibrium (b) forward bias (C) reverse bias (W: the depletion width, q: electron charge, V_{bi}: built-in potential, V_F: forward voltage, V_R: reverse voltage). [23]*

well as within the bulk semiconductor material. The recombination rate strongly determines the performance of the solar cells. Therefore, the best solar cell materials should have high optical absorption, direct band gap and low density of recombination centres [4].

Solar cell performance parameters are described below together with the effect of these parameters on device performance. The solar cell efficiency (η) is the power extracted from the device divided by the power of the incident sunlight [29].

$$\eta = \frac{\text{output power}}{\text{input power}} \tag{1.3.1}$$

A current density-voltage (JV) curve can help determine many important factors for solar cell operation, such as efficiency, open-circuit voltage, short circuit current density, maximum power point and fill factor, as shown in Figure 1.7.

J_{sc} represents the zero bias current density (the current density at zero value of voltage). V_{oc} is the voltage at zero value of current or open circuit condition, and it is sensitive to temperature more than J_{sc} [30]. The product of current and voltage gives the power, and the maximum power point (MPP) represents the maximum power output (P_{MPP}) that a solar cell can achieve. Fill factor is the shape (i.e. squareness) of the curve [4]. V_{oc}, J_{sc} and FF are three

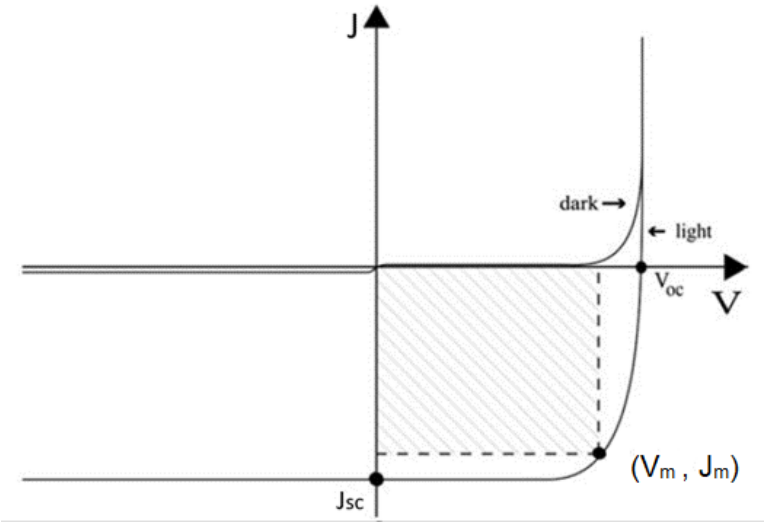

Figure 1.7: *JV curve under dark and light condition.J_m and V_m are the current density and voltage at the maximum power point [4].*

critical factors for solar cell efficiency and are related by:

$$P_{MPP} = J_m \times V_m \tag{1.3.2}$$

$$FF = \frac{V_m \times J_m}{V_{oc} \times J_{sc}} \tag{1.3.3}$$

$$\eta = \frac{V_m \times J_m}{P_{in}} = \frac{(V_{oc} \times J_{sc} \times FF)}{P_{in}} \tag{1.3.4}$$

Where J_m, V_m are the current density and voltage at the maximum power point and P_{in} is the power of the incident sunlight.

1.4 CdTe solar cells.

Thin-film solar cells based on cadmium telluride (CdTe) are excellent photovoltaic devices. It can supply clean energy from the sun for all [31]. In addition, it is a suitable alternative to expensive silicon solar cells. It has a direct bandgap of 1.45 eV which is very well suited to the solar spectrum. CdTe can also efficiently absorb all the incident sunlight because of the high absorption coefficient of approximately 10^4 per cm. [31, 32].For example, only 1 µm is enough to absorb 92% of the sunlight. In comparison, silicon solar cells require approximately

a thickness of 200 µm to reach this value of efficiency [31]. Figure 1.8 shows the recorded efficiencies for CdTe solar cells since 1972.

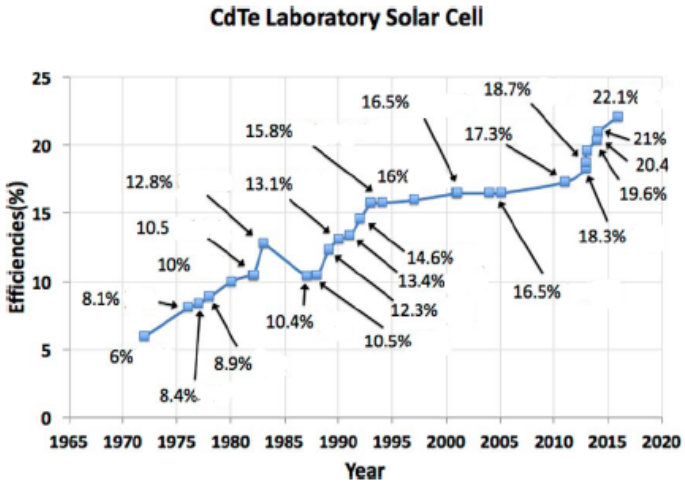

Figure 1.8: *CdTe solar cell efficiencies since 1972. [32]*

There have been many efforts to develop the efficiency of CdTe solar cells which is currently at a record cell efficiency of 22.1% [32]. The first CdS/CdTe solar cell in 1972 by Bonnet and Rabenhorst had an efficiency of only 6% [31]. First Solar and Antec Solar energy are two companies that produce CdTe solar cells. In Japan, Matsushita Battery produced screen printed and sintered CdTe solar cells for the indoor market such as Panasonic calculators [31]. However, CdTe has an issue with the toxicity of cadmium; the use of this material is harmful to both producer and the consumer [32]. There are many stages to consider starting with the mining and production of CdTe, production of solar cell modules, the active life which is more than 20 years and finally after the end of lifetime, disposal and recycling issues [31]. The short-term advantages of CdTe thin-film devices are, however, its longevity (i.e. environmental stability), reliability and conversion efficiency [12].

Figure 1.9 shows the typical superstrate configuration device structure for a CdS/CdTe solar cell. The light is incident from the glass superstrate side. In order to allow the most amount of light to reach the absorber layer, transparent conducting materials are deposited on the glass. In CdTe solar cells, fluorine-doped tin oxide (FTO) is commonly utilized with thin highly doped transparent layers providing sufficient conductivity, Since it is thermally and chemically stable, it can tolerate the additional layers in the device stack being deposited at high temperatures. The next layer is a thin deposited layer of CdS approximately 100 nm thick or less. This layer acts as an 'n-type window' layer for the incident light and consequently must be made as thin as possible in order to maintain a high photo-current.

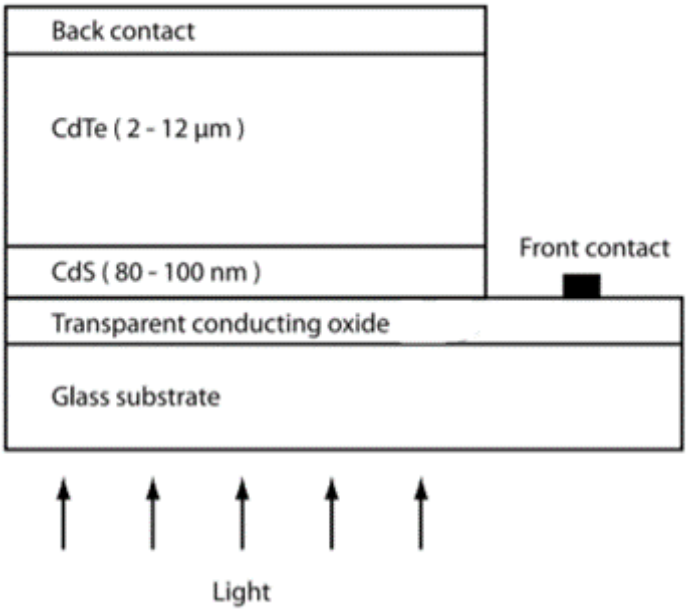

Figure 1.9: *A schematic diagram of CdS/ CdTe solar cell consisting of glass/transparent conducting oxide/CdS/CdTe and metal back contact layers [33]*

Light absorption largely takes place within the CdTe layer, which is deposited as a p-type semiconductor with a few µm of thickness. Finally, the back electrode is a conducting metal such as gold [33]. In contrast, the substrate configurations with reversed deposition order are much less common, because of the fact that substrate configurations have been shown to be remarkably less efficient than superstrate configuration [34].

There are several methods for depositing CdTe thin-films, such as physical vapour deposition (PVD), chemical vapour deposition (CVD) and close-spaced sublimation (CSS). Each of these methods has its own advantages and disadvantages, and the optimal deposition method depends on various factors such as the desired film quality, efficiency, and commercial viability. However, the CSS method has been used to fabricate the best CdTe-based thin film solar cells [35].

In this research, samples were prepared by using the close-spaced sublimation (CSS) method by collaborators in the University of Liverpool. (CSS) is a technique used to deposit thin-films of materials onto a substrate. This technique is commonly used in the production of thin-film solar cells, as it can deposit high-quality films with good uniformity over large areas. In this process, the substrate should be positioned facing the source material with a small gap between the two, typically only a few millimetres, which allows for controlled deposition of the material [36,37]. The substrate should be clean and free from any dust or other contaminants,

and it is important to have high-quality CdTe source material in order to produce high-quality films. The deposition of CdTe is achieved by heating the source material (CdTe powder) in a vacuum at the optimum range of temperature 500°C -600 °C [38], causing the material to sublime into the vapour phase and deposit as a thin-film on a substrate. Figure 1.10 shows the deposition setup. The source and substrate are separated by spacers made of quartz and are supported by graphite blocks, which are heated with quartz lamps in a vacuum tube [36]. Overall, close space sublimation is a useful technique for producing high-quality thin-films with precise control over deposition, making it a valuable process in many industries.

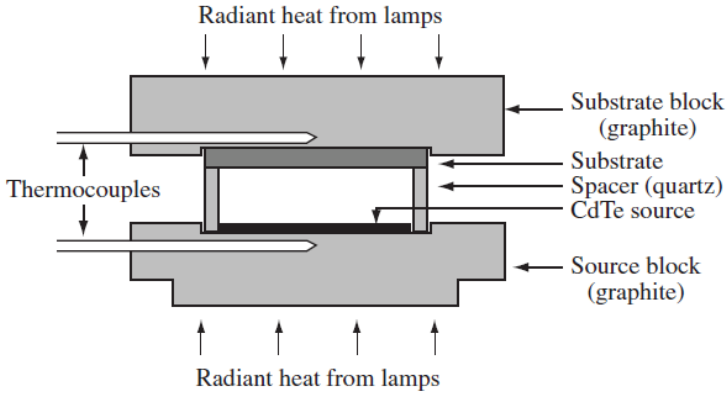

Figure 1.10: *CSS deposition system. [36]*

This thesis will examine CdTe solar cells with more focus on grain boundaries as an important defect that leads to efficiency losses in the device, as well as the role of Se alloying in producing higher efficiency Cd(Se,Te) solar cells. In the following sections, we will therefore present a more in-depth review of the various aspects of CdTe device technology that is relevant to this thesis.

1.5 Grain boundaries in CdTe solar cell

A grain boundary is one of the most critical defect in the material and can be defined as the interface region between two grains [39]. It reduces the device efficiency because of energy states within the bandgap associated with dangling bonds at the grain boundary [31]. These energy levels in the bandgap work as traps for electrons and holes thereby increasing Shockley-Read-Hall (SRH) non-radiative recombination [31].

Fundamentally, polycrystalline materials such as CdTe solar cells contain many grain boundaries. These defects influence the electrical and structural properties of semiconductors or

solar cells, due to the fact that the dangling un-passivated bonds and grain boundaries create a very high density of trap states. These trap states across the bandgap cause recombination as shown in Figure1.11.

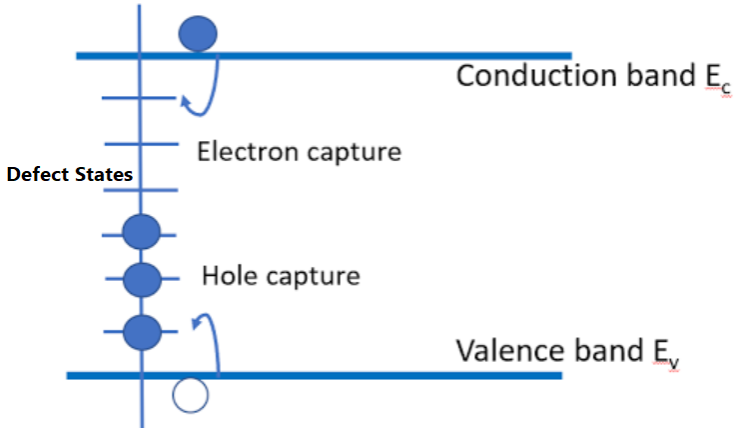

Figure 1.11: *Schematic of grain boundary recombination showing electron and hole capture at defect states. [40]*

Grain boundaries (GBs) are planar defects where the crystal orientation changes across it, through a rotation about a fixed axis. The atoms at the grain boundary are located in the wrong place or have the incorrect number of nearest neighbours (dangling bonds), and therefore have high energy. The grain boundary geometry can be described by a misorientation angle. The misorientation defines the change in crystallographic orientation relationship, which happens during the rotation, between the lattices of the neighbouring grains (i.e. between the two grains at the grain boundary) [41]. We can describe this mathematically: when one lattice rotates by an angle of rotation (θ), around the axis of rotation (UVW), the misorientation can be specified by an angle-axis pair. Tilt boundaries are formed if the grain boundary plane is parallel to the misorientation axis. Twist boundaries are formed if the grain boundary plane is perpendicular to the misorientation axis, as shown in Figure1.12 [41].

We can divide grain boundary types depending on the magnitude of rotation. In fact, there are several types of grain boundaries, the most significant will be discussed in the following sections.

1.5.1 Low-Angle and High-Angle Boundaries

Symmetrical low-angle tilt is a type of grain boundary, that occurs in crystalline materials. A low-angle tilt boundary occurs when the two grains are tilted with respect to each other by a small angle, typically less than 15° [42]. This boundary is a series of parallel edge

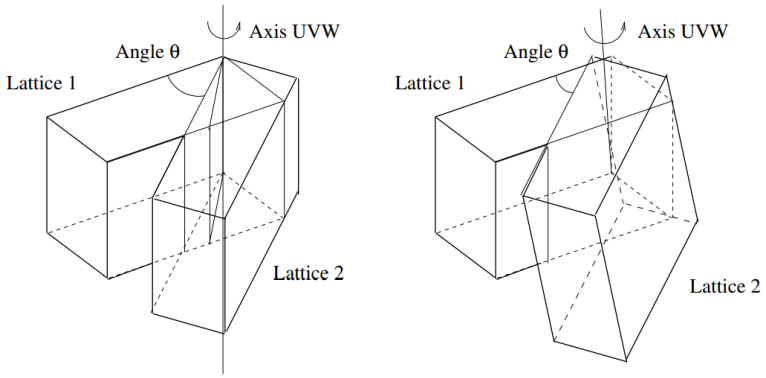

Figure 1.12: *The misorientation is defined by the rotation angle (θ) about the common axis UVW. The left-hand diagram is a tilt boundary, while the right-hand diagram is a twist boundary [41].*

dislocations, which are linear defects that occur when there is a mismatch in the crystal lattice between adjacent grains (Figure 1.13). The dislocations enable the grains to accommodate the misalignment and reduce the energy associated with the boundary.

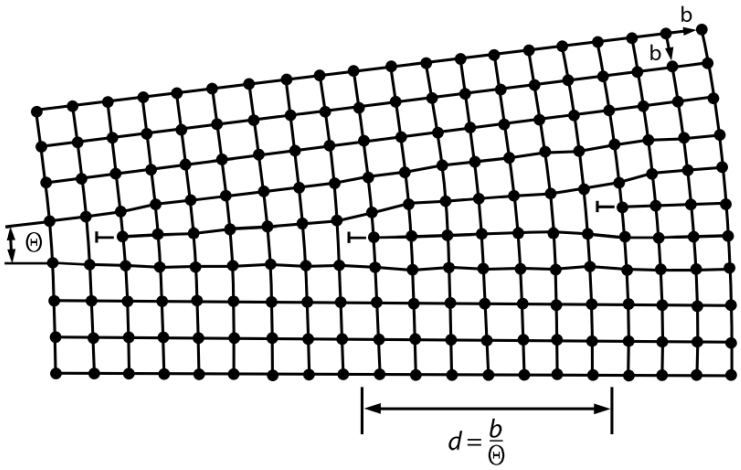

Figure 1.13: *Low-angle tilt grain boundary with an array of edge dislocations separated by seven lattice planes [33].*

The energy of a low-angle grain boundary depends on the spacing of the dislocations, where each dislocation has a Burger vector magnitude b. The tilt angle (θ) between the two grains is determined by the length of the Burger vector (b) and the spacing between neighbouring dislocation lines (d) [33]:

$$d = \frac{b}{\theta} \tag{1.5.1}$$

From this formula, there is an inverse relationship between d and θ, At very small values of (θ) the dislocation spacing is very large, and in contrast, the number of dislocations per unit

grain boundary length increases with the rotation angle [42].

Figure 1.14 shows the variation of grain boundary energy with misorientation angle. When θ exceeds 10-15°, the dislocation spacing is so small that the dislocation cores overlap. This makes it impossible to physically identify the individual dislocations. If θ is greater than 10-15°, the boundary is known as a high-angle grain boundary. High-angle boundaries generally have large areas of poor fit and have a relatively open structure. This means that the bonds between the atoms are broken or highly distorted, which leads to high energy. These are known as 'random' grain boundaries [43].

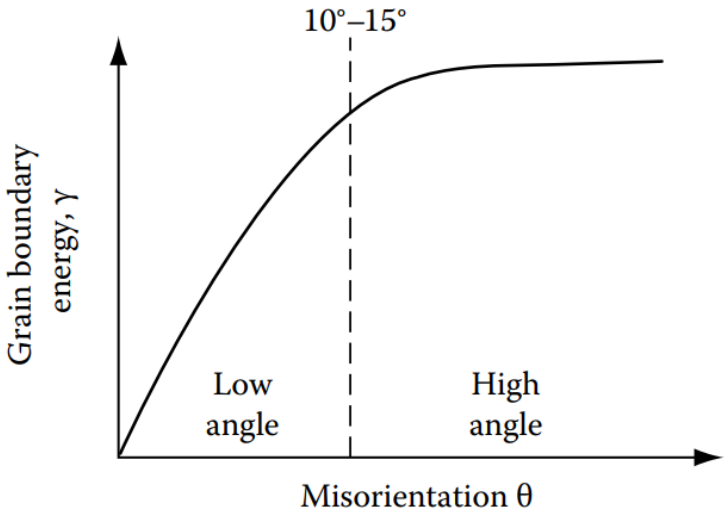

Figure 1.14: *Grain boundary energy as a function of the misorientation angle [43].*

.

Some high-angle boundaries do not have an open, disordered structure, as there are certain orientations and planes at which the two lattices fit together well, without too much distortion of the atoms. They have significantly lower energies than random boundaries. For example, Figure 1.15 shows the grain boundary energy as a function of twist misorientation angle for copper which has a face-centred cubic (FCC) crystal structure. It shows that the minimum energy appeared around some special angle ranges such as 60° [43]. These special grain boundaries are known as 'coincident site lattices' (CSL). The 60° CSL is a special class of grain boundary, known as a twin boundary, where the grains on either side of the boundary are mirror reflected (Figure 1.16) [33].

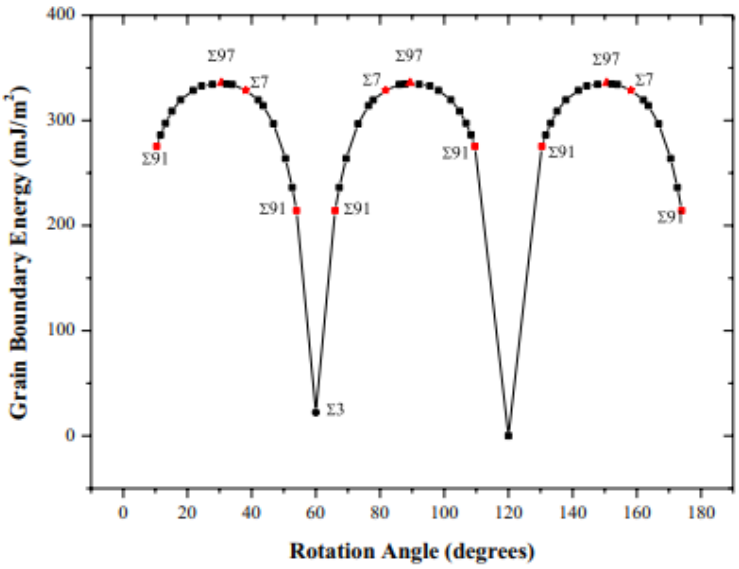

Figure 1.15: *GB energy as a function of the rotation angle for <111> twist [44].*

1.5.2 The Coincidence Site Lattice (CSL)

The atoms at the grain boundary tend to occupy the lowest energy positions. If we overlap two crystals with different orientation, it is possible that some of the atoms in both crystals will occupy the same positions (i.e. coincidence sites). Periodicity of these coincidence sites forms the Coincidence Site Lattice (CSL) [42]. The CSL can be defined as the smallest lattice of coincident sites for the two crystals. CSLs are characterised by a parameter called the coincidence index Σ, the ratio of total number of lattice points to the number of lattice points in coincidence [45].An alternative definition of Σ is:

$$\Sigma = \frac{Coincidence\ unit\ cell\ volume}{Crystal\ lattice\ unit\ cell\ volume} \tag{1.5.2}$$

The parameter Σ determines how similar the crystal lattice is to the CSL. The larger the value of Σ, the fewer number of coincidences sites at grain boundaries. In contrast, a small value of Σ comes with a large number of coincidences sites [42].

One example of CSL is the Σ 3 (111) twin boundary in face centre cubic (FCC) crystals. The twin boundary plane can be either (111) or (211), and correspond to 'coherent' and 'incoherent' twin boundaries. Σ3 coherent twin has the lowest energy, due to the nearest neighbour bonding being unchanged across the interface, and it is therefore beneficial to have a large amount of coherent twin boundaries relative to the total grain boundary area [41]. Σ3 incoherent twin boundary does not have energy as low as the coherent twin due to some

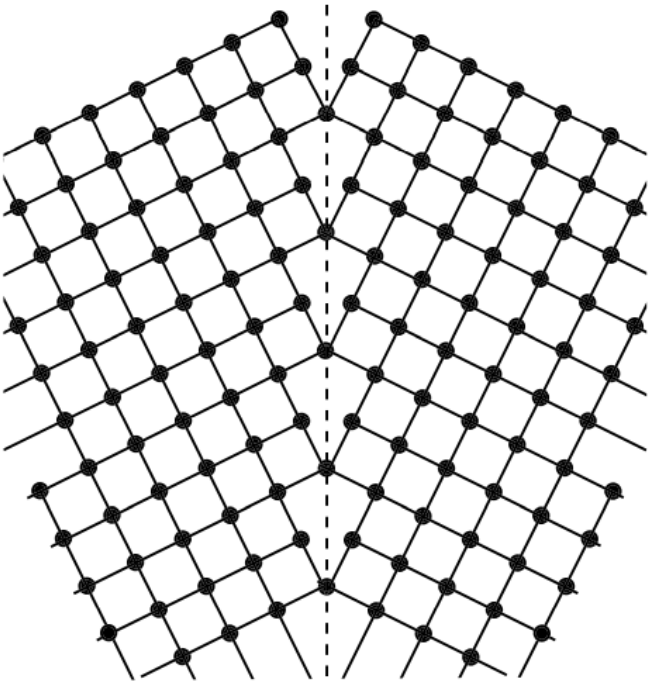

Figure 1.16: *Twin grain boundary in a cubic crystal [33].*

strain of the nearest neighbour bonds, but still the energy is lower compared to a random high angle grain boundary [41].

1.5.3 Para and ortho twin

Para and ortho twinning refers to different types of crystal twinning, where there are two physically different, polar opposite types of GB [46]. In a face-centred cubic structure there is only one type of atom, which occupies all the lattice points. Therefore, there is no possibility for para-ortho twinning to occur in the simple FCC structure. On the other hand, the zinc blende structure consists of two interpenetrating face-centred cubic lattices, such as CdTe, each containing one type of atom (cadmium or tellurium), allowing for the possibility of para-ortho twinning. The terms ortho and para refer to the orientation of the constituent Cd and Te atoms in the crystal lattice [47]. Inverted (para) twin occurs when two crystal domains are related by a 180° rotation around a specific [111] axis, leading to wrong Cd-Cd or Te-Te bonds at the interface as shown in Figure 1.17(a). On the other hand, Figure 1.17(b) shows upright (ortho) twin, which has the perfect Cd-Te bonding formed across the GB interface. This twin has very low energy and few sub-bandgap states compared to the inverted (para)

twin which has larger energy and deeper gap states in the bandgap [46].

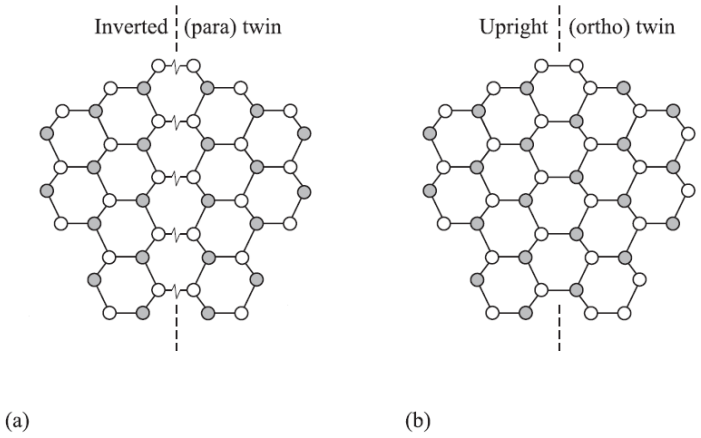

Figure 1.17: *(a)The inverted twin GBs, which have wrong (Cd-Cd or Te-Te) bonds at the GB interface. (b) the upright twin GBs, which have perfect (Cd-Te) bonds at the GB interface. [46].*

1.6 Chlorine treatment.

CdTe thin-film does not generate high efficiency after just the deposition step due to the high density of deep gap states which lead to non-radiative recombination at grain boundaries. At the interface between neighbouring grains, the periodic lattice structure terminates, resulting in dangling bonds and the formation of defect gap states. Depending on the degree of misorientation between grains, the atomic arrangement at the grain boundary can produce a density of states within the energy gap of bulk CdTe. These grain boundary defect states act as recombination centres for the photogenerated charge carriers and lead to a reduction in solar cell efficiency. One way to reduce the negative impact of grain boundaries is by increasing the grain size to reduce their density. This can be achieved by promoting grain growth. Another way is by passivating them. This involves treating the surface of the semiconductor with a material that can react with the dangling bonds at the grain boundary and eliminate their recombination activity. One effective passivation method is using a chlorine doping process [48]. This chlorine activation step is achieved by depositing a thin layer of $CdCl_2$ on the CdTe back surface and annealing at 350-450°C in air for 20 minutes [4]. At this temperature, the $CdCl_2$ dissociates introducing chlorine into the CdTe. This modifies the grain boundaries of the CdTe layer through chlorine segregation, which can increase the carrier lifetime and improve the efficiency of the solar cell [49]. Figure 1.18 shows the high concentration of chlorine at the GBs.

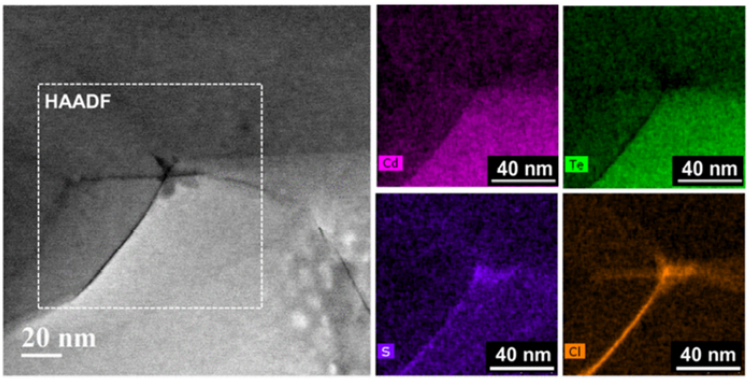

Figure 1.18: *Energy dispersive X-ray (EDX) maps acquired in the transmission electron microscope (TEM) showing that S and Cl segregate at the GBs, while Cd and Te do not. [50]*

Moreover, Mao *et al.* [51], measured chlorine concentration in polycrystalline CdTe films using Time of Flight Secondary Ion Mass Spectroscopy (ToF-SIMS). They found that more than 90% of chlorine concentration was at the GBs. There was also a saturation level of chlorine concentration at GBs, and the solar photovoltaic device performance declined when the chlorine concentration at GB is below the saturation level. Figure 1.19(a,b) shows an electron backscattered diffraction (EBSD) image and a Cl ToF-SIMS image for the same CdTe area. It is observed that the chlorine is heavily concentrated at the grain boundaries of the CdTe, with a variation in the intensity of the chlorine concentration at the different grain boundaries.

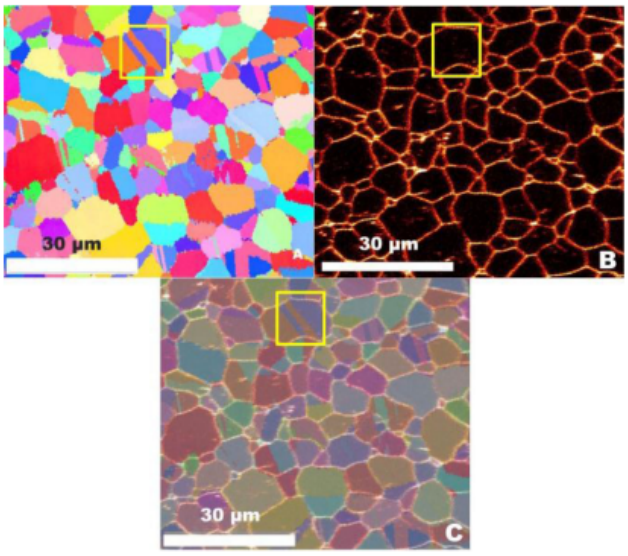

Figure 1.19: *Images showing; (a) the EBSD grain structure, (b) the ToF-SIMS 2D Cl map, and (c) an overlay of these two images. [51]*

Chlorine treatment also improves the crystalline quality of the CdTe layer and reduces defects, as CSS CdTe deposited layers are observed to have high densities of stacking faults. Abbas *et al.* [52], found that chlorine activation can improve the device performance by removeing the stacking faults in the CdTe grains. Figure 1.20 shows the low efficiency of the as-deposited cell (without activation using cadmium chloride) compared to the high efficiency for the cadmium chloride treated device. Therefore, the process of passivation by using $CdCl_2$ has a significant advantage for CdTe solar cells performance, and the CdTe as-fabricated device must undergo a chemical treatment by doping with chlorine in order to achieve high efficiency.

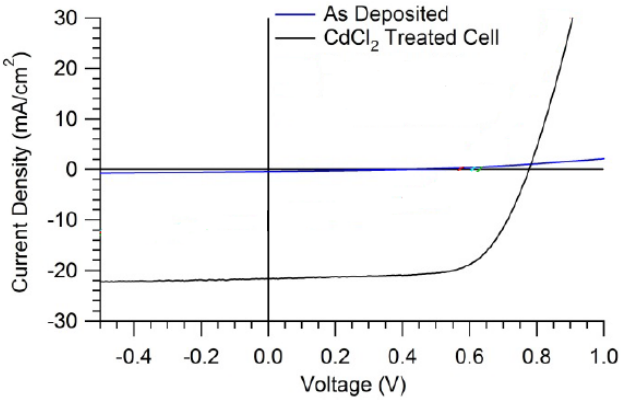

Figure 1.20: *J-V curves of as-deposited and chlorine treated cadmium telluride cells. [52]*

1.7 CdSeTe solar cells

Improving the efficiency of CdTe devices can be achieved through the use of $CdTe_xSe_{1-x}$ alloy. The increase in efficiency of CdSeTe solar cells is partly a result of higher short circuit current density J_{sc}. This is because selenium from a CdSe window layer or CdSeTe layer can diffuse into CdTe and reduce the bandgap. In one study where a 800 nm CdSeTe layer was used to fabricate high efficiency CdTe cells, the 1.5 eV band gap of CdTe decreased to 1.4 eV, and the current density increased from about 26 to over 28 mA/cm^2 [53]. By replacing the CdS window layer with CdSe, the quantum collection efficiency for short and long wavelengths will increase leading to larger J_{sc} values [54, 55]. Zheng *et al.* [56], recorded an increase in the cell efficiency from 16 % to 22% with an increase in the photocurrent. They also conclude that Se can passivate grain boundaries and improve the carrier lifetime of grain-interior [56]. Se diffusion can enhance solar cell performance parameters, including fill factor (FF) and power convention efficiency (PCE) because the solubility and diffusion of Se in CdTe is higher than S [54]. The lower band gap in principle would also decrease the

V_{oc}, although in some devices this is mitigated by the increase in carrier lifetime, so that any changes to the V_{oc}, are small [48]. Paudel and Yan [55] reported that the J_{sc} can be enhanced in both short and long wavelength regions by using CdSe as the window layer, as Se has a higher solubility in CdTe compared to S, which leads to stronger interdiffusion at the CdSe/CdTe interface. As a result, $CdTe_xSe_{1-x}$ alloys with high x values are formed. These alloys have a lower bandgap than pure CdTe due to the bowing effect, where the bandgap of the alloy is affected by the composition of the alloy. The amount of Se diffused into CdTe was affected by the thickness of the CdSe window layers. For example, varying the thickness of CdSe layer from 0 nm to 750 nm, the measured band gap decreased from 1.475 eV to 1.354 eV. The highest cell efficiency was with a 100nm thickness of CdSe, and when the thickness of the CdSe layer was increased to 350 nm, the average J_{sc} decreased to 15.4 mA/cm^2.

Figure 1.21 shows the external quantum efficiency (EQE) of the different thicknesses of CdSe window layer. There is a reduced blue response when the CdSe thickness increased to 350 nm and 750 nm. The redshift for the absorption edge increased when the thickness of the CdSe window layer increased. This improved redshift is due to the band gap reduction of the absorber layer.

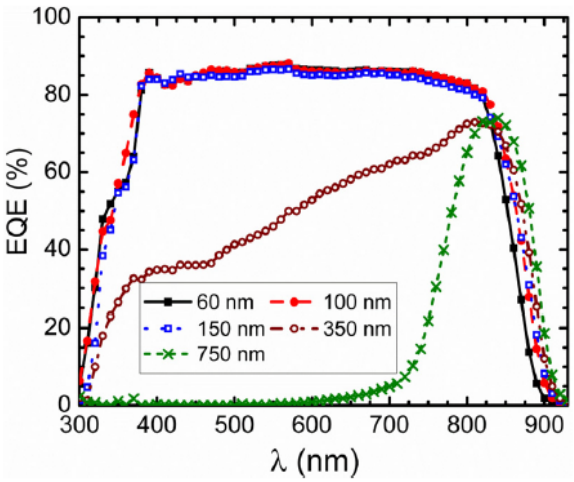

Figure 1.21: *EQE spectra for CdTe cells with CdSe window layers of different thicknesses. [55]*

The CdSeTe layer (which is formed during the growth of CdTe) has the ability to convert the incident photon to current, and this depends on Se concentration and crystal structure. At higher Se concentrations the crystal structure transforms from cubic zinc blende to hexagonal wurtzite, which is found to be photo-inactive [54]. This is the reason for the large drop in EQE for thicker CdSe layers. Another study showed that the CdSeTe and CdTe thicknesses

are crucial to the overall device efficiency, as it was observed that the thinner layer of CdSeTe at the front of the device appeared to have higher efficiency when compared with the thicker CdSeTe devices [57]. It was found that the CdSe window layer thickness of 100nm has the highest performance parameters. For example, V_{oc} for 100 nm CdSe layer is higher than the same layer with 50 nm thickness [54].

Fiducia *et al.* [48], used cathodoluminescence (CL) and secondary ion mass spectrometry (SIMS) to show that selenium enables higher luminescence efficiency and longer diffusion lengths in the selenium alloyed CdTe thin-film, indicating that selenium passivates critical defects in the bulk of the absorber layer. They examined selenium diffusion into the CdTe layer on a shallow 7° bevel cross-section of CdSeTe/ CdTe solar cells (Figure 1.22a). Figure (1.22b) shows the SIMS map of the selenium concentration on the bevel surface. There is a gradual decrease in the selenium concentration with distance away from the front interface. In the interdiffused CdTe region, the selenium concentration around the grain structure of the absorber was non-uniform with increased selenium concentration at the grain boundaries. This is clear in the high-magnification image shown in Figure (1.22d). Moreover, CL panchromatic images have been acquired in the same bevelled area. Figure (1.22c) shows that at the CdTe region, the luminescence intensity is fairly low, but at the bottom of the bevel at the CdSeTe region, the luminescence intensity is much higher. The higher luminescence intensity indicates that Se alloying in CdTe reduces non-radiative recombination and therefore improves the overall lifetime.

1.8 Project aims and thesis outline

The aim of this study is to provide new insight into the understanding of the relationship between grain boundaries and the efficiency of CdSeTe solar cells. To gain more efficiency for CdSeTe solar cells, there is a need to understand the role of grain boundaries in the recombination, and the role of Se diffusion, in order to reduce the CdSe-CdTe interface and grain boundary recombination. Electron microscopy was used in this project as a valuable tool for investigating the microstructure and optical properties of solar cells at the nanoscale. It can produce high-resolution images of the solar cell microstructure and analyse the chemical composition. This can help characterise CdTe solar cells and identify defects, such as grain boundaries.

The specific project aims are:

1- To combine cathodoluminescence (CL) and Electron BackScatter Diffraction (EBSD) to

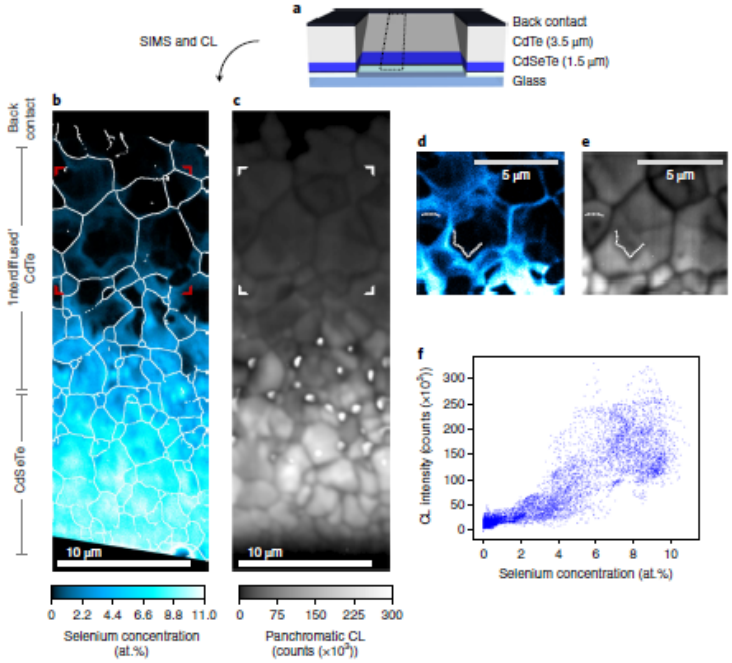

Figure 1.22: *a, A schematic of the CdSeTe/CdTe device structure with 7° bevel cross section. b, A SIMS elemental map of the selenium distribution on the bevelled surface. c, A panchromatic CL image for the same area. d, A high-magnification selenium map of the region at the top of the bevel. e, high-magnification CL map corresponding to the SIMS map in d. f, A plot of the selenium concentration versus CL counts for equivalent regions. [48]*

study the effect of CdTe grain boundaries on the recombination process. The grain boundary character was determined by EBSD. CL is then performed on the same area to obtain information on recombination. Recombination is monitored by the decrease in CL intensity at the grain boundary; the larger the decrease in CL intensity the stronger the non-radiative recombination at the grain boundary and therefore the more harmful to the device performance.

2- To investigate the microstructural changes taking place during Se diffusion in CdSe/CdTe solar cells. A combination of CL and transmission electron microscopy (TEM) is used to explore the large decrease in EQE for thick CdSe layers (Figure 1.21)

3- To quantify diffusion of Se into CdTe. The diffusion coefficient is extracted by analysing chemical composition profiles measured in the TEM, as well as by monitoring the band gap changes due to Se using CL. The diffusion coefficient is essential for optimising processing parameters (e.g. deposition time and temperature) of CdSeTe solar cell devices.

The thesis is organised into the following chapters: in chapter three we use correlative CL and EBSD to investigate the effect of grain boundary misorientation on the recombination process. We found the twin boundaries $\Sigma 3$ appeared more frequently in the sample than

other misorientation angles. This is in agreement with Abou-Ras *et al* for CIGS thin-film solar cells. [58], Moreover, we noticed that this kind of grain boundary Σ3 has the lowest rate of recombination, which is in good agreement with other theoretical results which use Density Function Theory (DFT). For example, Tong *et al.* [59] found that Σ3 grain boundaries did not introduce deep band gap states. However, a high recombination rate was generally observed at misorientation angles between 35-55° and the highest recombination was at 35.34°, indicating that this angle might be harmful to the device. This was in disagreement with Moseley *et al.* [60] results, which found that regular grain boundaries are not as active as strong non-radiative recombination centers.

In chapter four we used TEM, beveled cross-section cathodoluminescence and time-resolved cathodoluminescence to characterise two samples with different CdSe layer thicknesses (100 nm and 400 nm). We found a small grain size and Kirkendall voiding at the CdSe-CdTe inter-diffusion layer for the thicker CdSe layer sample. We suspect that Se is pinning the grain growth. Together with the Kirkendall voiding the small grain size leads to higher rates of recombination, as evidenced by a significant drop in CL intensity in the inter-diffused region. TEM results confirm the zinc-blende cubic structure which shows that the large drop in EQE is therefore not due to the wurtzite structure of CdSe as in [54], but due to the solute pinning which affected grain growth and formed Kirkendall voids. Time-resolved cathodoluminescence measurements of the carrier lifetime shows that the inter-diffused CdSe/CdTe layer has a slower decay and longer lifetime compared to the CdTe layer.

Finally, in chapter five, we analyse the Se diffusion process in more detail to establish the diffusion coefficient. This has been done using energy dispersive X-ray (EDX) spectroscopy in the TEM, and the Se diffusion coefficient that measured in this work was 7.2×10^{-12} cm^2/s. Time-resolved cathodoluminescence measurements of the carrier lifetime shows that the inter-diffused CdSe/CdTe layer has a slower decay and longer lifetime compared to the CdTe layer. Moreover, The band gap variation on the bevel cross-section have been calculated using CL spectrum imaging in the scanning electron microscope (SEM), where band gap values were decreased from bulk CdTe layer (1.51 eV) to the inter-diffusion CdSeTe layer (1.42 eV).

Chapter 2

Experimental Techniques

This chapter provides a background overview of the experimental methods and techniques that are used to collect data in this thesis. The majority of techniques used in this research to investigate CdTe-CdSe solar cells are based on electron microscopy. Therefore, an in-depth discussion will be presented on electron microscopy, and apart from reviewing instrumentation such as scanning electron microscopy (SEM), focused ion beam (FIB), and transmission electron microscopy (TEM) we also introduce a more in-depth explanation of the major techniques used, which includes cathodoluminescence (CL) for optoelectronic properties measurement, and electron backscatter diffraction (EBSD) for grain boundary misorientation.

2.1 Sample preparation

The CdTe-CdSe samples used in this research were fabricated and deposited by Drs Jacob Leaver and Jon Major at the University of Liverpool, with structure glass/ FTO/ SnO_2/ CdSe/ CdTe/ Au as shown in Figure 2.1. The device was grown on fluorine-doped tin oxide (FTO) coated glass substrates (TEC15M). Two different types of samples were produced. Series A where the CdSe window layer had a thickness of 100nm, but with different close space sublimation (CSS) gas pressure values during CdTe deposition, i.e. 0, 25, 50 and 100 torr. The second series B had the same device structure, but with different thicknesses of the CdSe window layer i.e. 50 nm, 100 nm, 200 nm and 400 nm, with the CdTe being deposited under 5 torr of CSS pressure.

2.2 Introduction to Electron Microscopy

The main aim of this thesis is to study how the CdSeTe solar cell electrical and optical properties changes depending on the microstructure, such as grain boundary misorientation or Se inter-diffusion. In light of this aim, it is necessary to characterise the electrical and optical properties of our sample at nanometre length scales. There are various techniques used to characterise solar cells. In this thesis scanning electron microscopy (SEM), cathodoluminescence (CL), focused ion beam (FIB), electron backscatter diffraction (EBSD), and transmission electron microscopy (TEM) is used to investigate the CdSeTe solar cell properties. These techniques provide information about surface topography, layer structure, material composition, and optoelectronic properties.

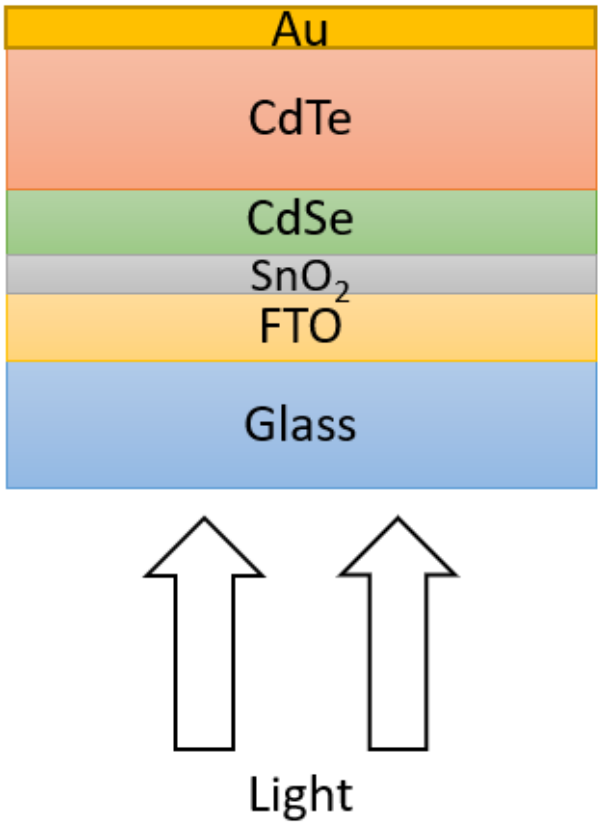

Figure 2.1: *Schematic diagram of CdTe-CdSe solar cell used in this study.*

Electron microscopy refers to a family of instruments and techniques that uses electromagnetic lenses and fast-moving electrons for the analysis of the material. The human eye can distinguish features larger than about 100 µm. Electron microscopy has the ability to identify or determine much smaller features (up to a few nanometers) in the specimen, and the microscope resolution is the minimum distance between two features that can be recognised clearly as two separate objects. To gain this resolution, the wavelength should be smaller than the distance between the two objects. de Broglie suggested that electron has dual nature, which means it can also behave as waves. The de Broglie equation expresses the electron wavelength according to the following formula [61].

$$\lambda = \frac{h}{p} = \frac{h}{mv} \tag{2.2.1}$$

where λ is the de Broglie wavelength, h is Planck's constant, p is the momentum, m is the mass and v is the speed. The electron wavelength in an SEM is of the order of picometers (10^{-12} pm). However, due to lens aberrations, the spot size of the beam is typically a few nanometers.

When the electrons in the form of a wave passes through an aperture, diffraction will occur. Electrons from a point source cannot be concentrated into a perfect dot due to diffraction. Instead, the image will appear as a small bright spot surrounded by weaker subsidiary maxima, having a diameter larger than the source as shown in Figure 2.2. This bright disk surrounded by dark rings is called an Airy disc [62]. The radius of the Airy disc is calculated by:

$$d = \frac{0.61\lambda}{\sin\alpha} = \frac{0.61\lambda}{\alpha} \tag{2.2.2}$$

where d is the radius of the Airy disc (the resolution), λ is the electron wavelength and α is the maximum angle of diffraction.

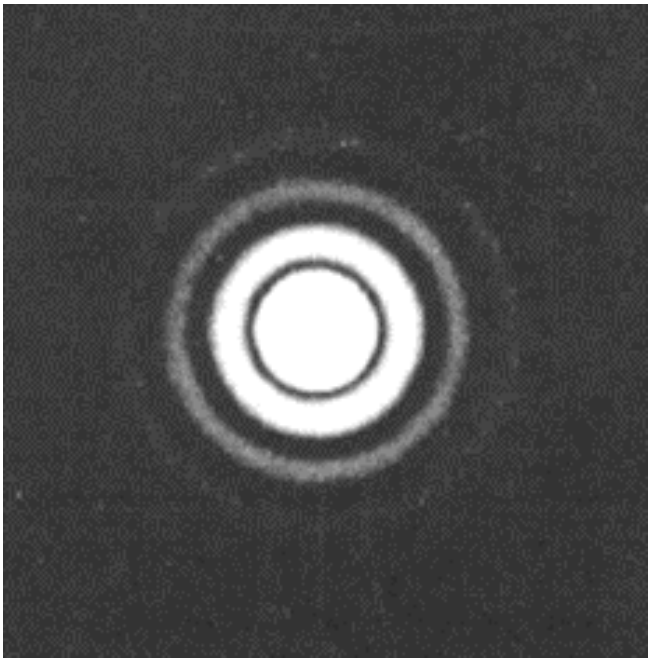

Figure 2.2: *Airy disc with central bright spot surrounded by dark halos. [62]*

The spatial resolution of an electron microscope depends on the size of the electron beam spot which in turn depends on the wavelength of the electrons and the optical system that produces it [63]. The resolution of the microscope based on the Rayleigh criterion is the ability to distinguish two points as separate depending on the relative overlap of Airy discs for the two points, as shown in Figure 2.3 (a). The two objects can be recognised from one another when the centres of two central peaks are separated by a distance equal or larger than the radius of the Airy disc, as shown in Figure 2.3(b) [64].

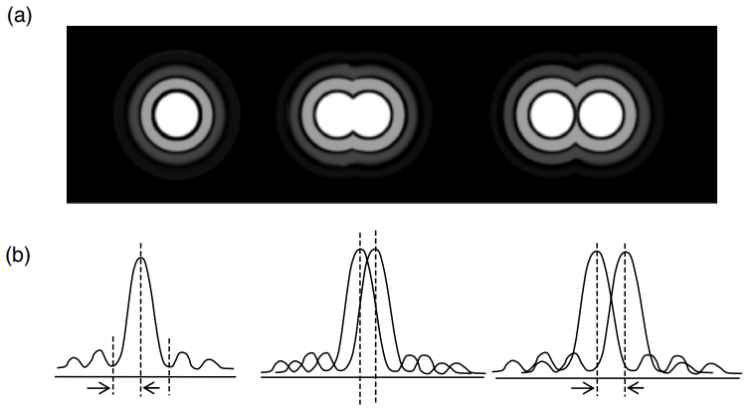

Figure 2.3: *Schematic illustration of resolution depending on (a) Airy disc overlap and (b) intensity profiles . [64]*

2.3 Scanning Electron Microscope (SEM)

Scanning electron microscope (SEM) is one of the most powerful tools that scientists use for analysing and characterising the material microstructure. This tool produces high resolution images that give physical and chemical information about the sample. These images can uncover many properties such as morphology, defects, and grain boundaries, as well as optical emission (cathodoluminescence) [65]. An SEM contains three main parts, the electron column, the specimen chamber and computer controls, as shown in Figure 2.4. Electron column has the electron gun which generates the electron beam followed by the condenser electromagnetic lenses. It can focus the electron beam into a small diameter, and in the last section of the column, there are scan coils and an objective lens as shown in Figure 2.5, [61].

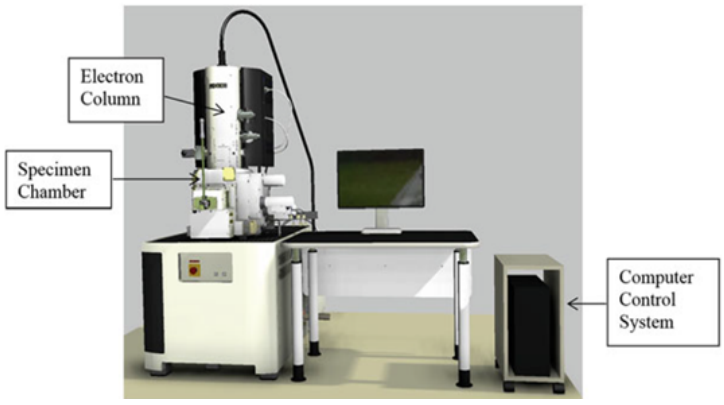

Figure 2.4: *Three main sections of the SEM. [61]*

Electrons are accelerated from the cathode to the sample via thermionic or field emission under voltage differences typically in the range 5-30 kV [66]. The electron beam emitted

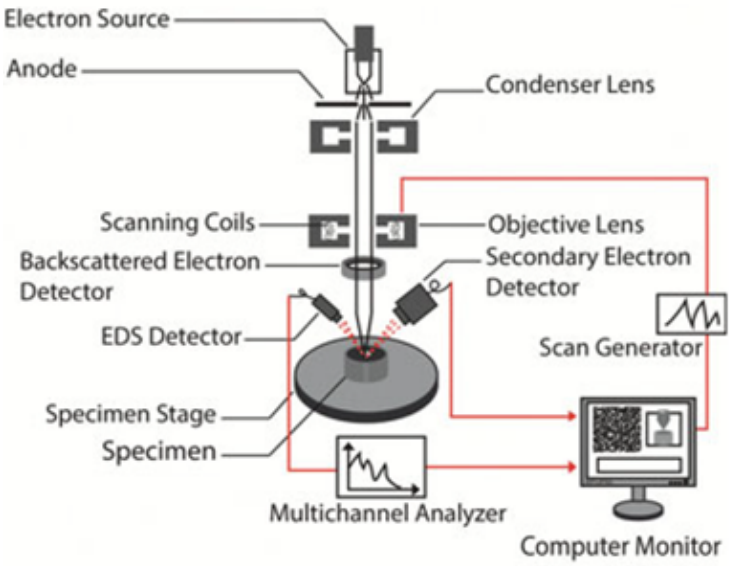

Figure 2.5: *Schematic of the SEM. [61]*

from the gun has a wide diameter of approximately 20 nm (for field emission) which can be demagnified by the condenser lenses. A set of electromagnetic lenses is used to focus the electron beam into a narrow spot [61]. Scanning coils before the final objective lens raster the electron beam across the surface of the specimen. The intensity of the signal generated by the rastered electron beam forms the SEM image [66]. This image is formed by signals of either backscattered electrons (BSE), secondary electrons (SE), X-rays or light cathodoluminescence (CL), as a result of the interaction between the electron beam and the sample [65]. Finally detectors can detect these signals and display it on a monitor [61].

The operation principle of SEM is to focus a beam of electrons by electromagnetic lenses over the sample. The beam of electron upon striking the surface forms a spot. The beam is then scanned from point to point over the sample. At each point interaction of the electron beam with the sample will produce a signal which shows the local properties of the sample. Hence the respective pixels in the image give details about surface topography, material composition, layer structure, or optoelectronic properties, depending on the signal being mapped.

When a beam of primary electrons strike the surface of the material they will not stop there but be scattered elastically and inelastically in the material, hence forming an interaction volume. The interaction volume extends inside the material like a pear shape as shown in Figure 2.6. The size and dimensions of the pear shape depend upon the energy of primary electrons, the density of the material, as well as the atomic number of the material. The interaction volume and depth of penetration increase with larger beam energy and decrease with higher specimen atomic number, since specimens with greater atomic numbers have

more "'stopping power' [64].

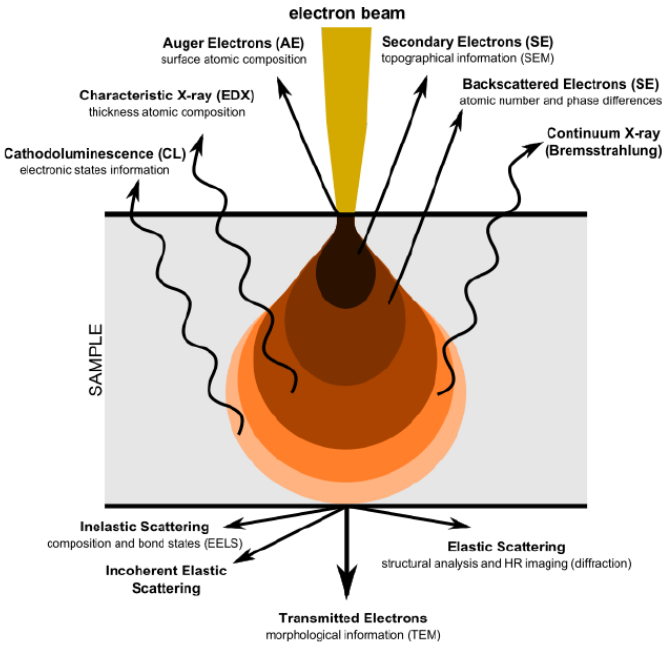

Figure 2.6: *Interaction volume showing the various signals generated by an electron beam. [67]*

Below some of the more common electron beam and sample interaction signals are described in more detail:

Secondary Electrons

One of the most commonly used signals generated close to the specimen surface are secondary electrons (SE). They have very low energy of around 3–5 eV, because only electrons generated within a few nanometers from the sample surface are detected. Figure 2.7 (a) demonstrate the secondary electrons are produced when an incident primary electron interacts inelastically with atomic electrons, i.e. the incident electron transfers part of its kinetic energy to the atomic electrons. The intensity of the signal depends on the number of secondary electrons reaching the surface [68]. There is a difference in secondary electron intensity which will be detected from a flat surface or a tilted surface because a higher fraction of electrons from a tilted surface will travel near the surface to generate more secondary electrons. Regions where secondary electrons are prevented from reaching the detector will appeared darker in contrast. Therefore, secondary electron SEM imaging is helpful to obtain topographic contrast of the sample as shown in Figure 2.8 [64], [65].

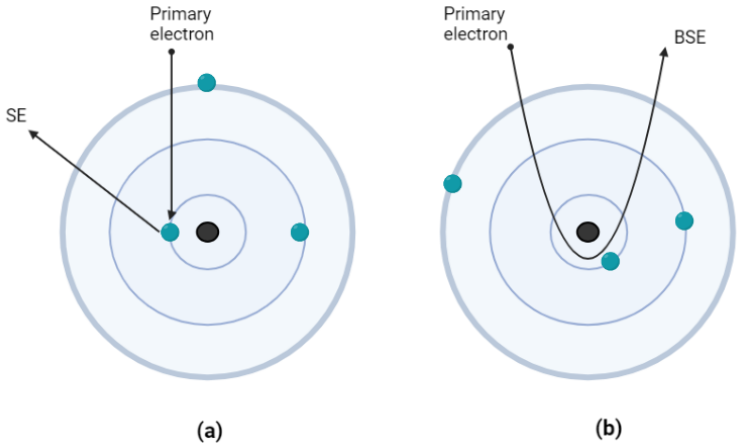

Figure 2.7: *Formation of secondary electrons (a) and backscattered electrons (b).*

Backscatter Electrons

Backscatter electrons (BSEs) are another useful signal for SEM imaging. The detection of BSEs can provide compositional information of the sample. Backscattered electrons are produced when the primary electron interacts with the atom nuclei elastically as in Figure 2.7 (b). The interaction causes a deviation of the primary electron by an angle more than 90°. Backscattered electrons have a high energy similar to the incident primary electron. Because they are generated from greater specimen depths, they form images with less topographic contrast compared to secondary electrons. Backscatter electrons are influenced by atomic number, as elements with high atomic numbers have more backscattered electrons. Therefore, backscattered imaging in SEM provides us with information about the atomic number (i.e. chemical composition) of the sample.

Characteristic X-rays

When the primary electron beam strikes the sample, it can collide with another electron in the inner shell of an atom and remove it from its orbit, leaving a vacancy behind. An electron from an outer electronic shell with higher energy can fill this vacancy. The difference in the energy during this transition to a lower energy shell is released as X-rays, which is called characteristic X-ray radiation. The energy of the X-ray emitted during this electronic transition is unique for each chemical element, electronic shell (K, L, M), and electronic transition (α, β, γ), Figure 2.9 . The energy of this characteristic X-ray can be detected by a dispersive X-ray energy detector. Therefore, characteristic X-ray radiation analysis is useful for determining the abundance of elements and the chemical characterisation of the

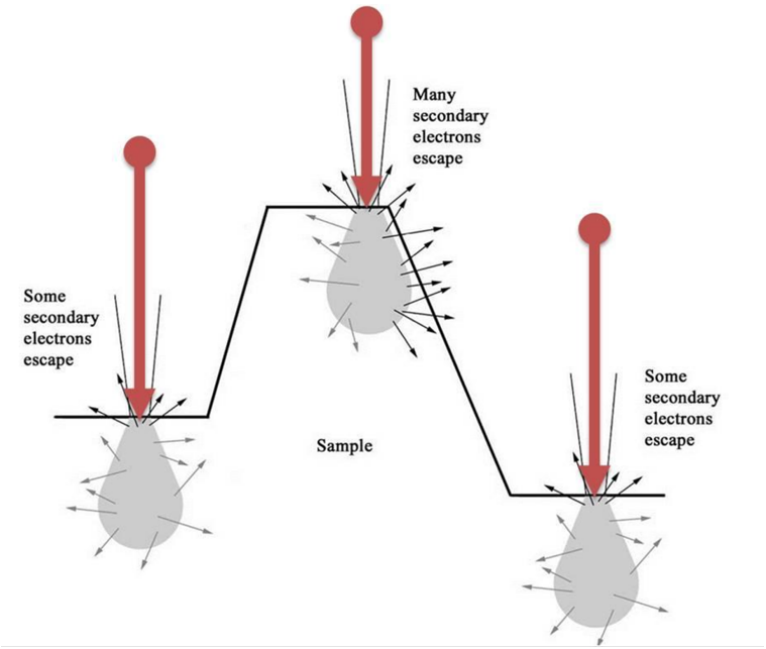

Figure 2.8: *Topographic contrast due to variations in secondary electron emission. The side walls of the asperity has a higher secondary electron intensity compared to the flat regions [69]*

sample [68].

Cathodoluminescence signal

The light emitted from the specimen when exposed to the electron beam is called cathodoluminescence. When a high energy electron beam strikes a semiconductors material in SEM, it causes valance band electrons to be promoted into the conduction band, leaving a hole behind. These electron-hole pairs can then recombine to generate cathodoluminescence. A dedicated SEM detector is used to collect the light signal and to analyze its specturm [70]. More details about the cathodoluminescence technique and radiative recombination mechanisms are given below.

2.3.1 Cathodoluminescence Technique

Cathodoluminescence (CL) is a unique technique that provides optoelectronic information about the material [66]. CL is able to detect the light (photons) emitted during radiative electron-hole pair recombination. Using this technique, recombination at grain boundaries can be studied [66]. When the high energy electron beam bombards the sample of a semiconductor material, it yields intrinsic and extrinsic CL emissions. The inelastic scattering of a high energy electron can break the weak bond of a valence electron to promote it to

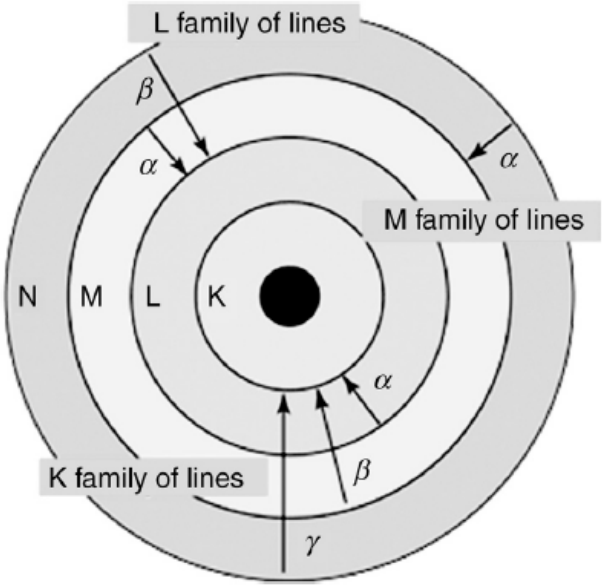

Figure 2.9: *K, L, and M families of characteristic X-rays. [68]*

the conduction band, leaving a hole in the valence band. When a positive hole and free electron recombine, a photon will be emitted as a result of the energy difference (intrinsic CL emission). On the other hand for extrinsic materials which have impurity atoms, it can create energy levels in the bandgap which allow for additional recombination pathways, such as donor acceptor pair recombination (extrinsic CL emission). Therefore, CL is a powerful technique for analysing charge carrier recombination behaviour. By using this technique dopant concentration and charge carrier lifetime can be analysed [65].

SEM-CL microscopy has the same setup process for standard SEM. However, CL radiation is collected by a parabolic mirror and detected by a photomultiplier tube [66]. The sample is positioned at the focal point of the parabolic mirror and the light that is emitted from the sample is transferred via a light pipe into the photomultiplier tube as shown in Figure 2.10 [71]. The light could also be passed through a dispersion grating (monochromator) to separate it into its constituent wavelengths, thereby enabling CL spectroscopy to be performed [72].

The performance of solar cells is restricted by a variety of losses, which can be analysed using CL. Below is a brief description of the losses that can lower the efficiency of a solar cell. For solar cells with a single bandgap, photons with lower energies than the material bandgap energy cannot be absorbed and are therefore not absorbed by the material. In contrast, when the incident photon energy is larger than the band gap, there will be thermalisation loss, where the excess energy of the photoelectrons above the conduction band minimum will be converted to heat. The temperature of the solar cell will increase, which will further

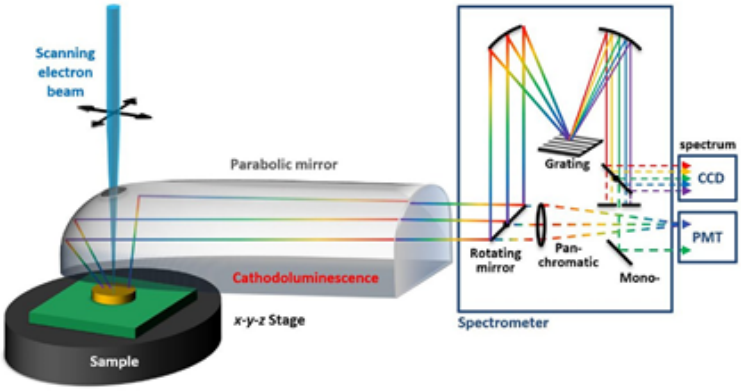

Figure 2.10: *schematic diagram of CL detection in SEM. [73]*

increase the reverse saturation current, so that the open circuit voltage is reduced [10].

In addition to these optical losses, there is another type of loss called collection losses. These losses are due to surface and bulk recombination in the semiconductor. The recombination is further classified into radiative and non-radiative recombination, the latter primarily being due to Shockley-Read-Hall recombination, which occurs at grain boundaries, interfaces and free surfaces. Radiative recombination, as shown in Figure 2.11, is when the electrons in the conduction band and holes in the valence band recombine, resulting in the emission of photons at or near the bandgap energy. This process is most common in direct bandgap semiconductors [40].

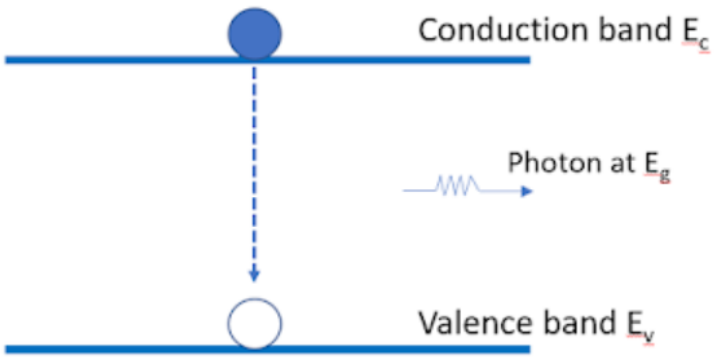

Figure 2.11: *Radiative Recombination. A conduction band electron recombines with a valence band hole, emitting a photon in the process. [40]*

The semiconductor may have some impurities or vacancies in the crystal structure, during the material's growth process. These impurities can cause localised defects in the bandgap of bulk semiconductors, which can traps or capture the free carriers. Dangling bonds at a grain boundary or interface are also localised defects and show a similar behaviour. This kind of

trap leads to non-radiative or Shockley-Read-Hall recombination as shown in Figure 2.12. If the trap is located near the centre of the bandgap, the recombination centre can capture electrons from the conduction band followed by hole capture from the valence band. This recombination event is non-radiative recombination, with the energies emitted as phonons [74].

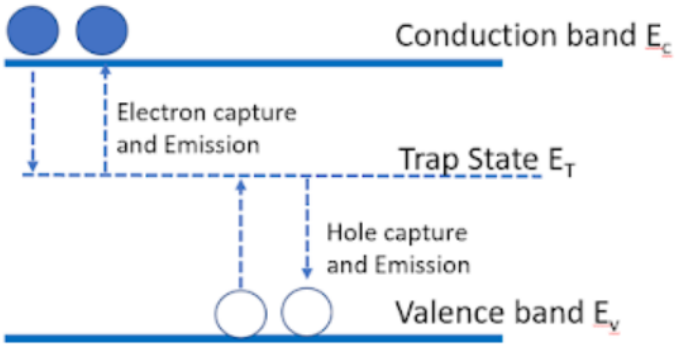

Figure 2.12: *Non-Radiative (Shockley-Read-Hall) Recombination. Conduction band electrons recombine with valence band holes via defect states within the band gap. [40]*

The radiative recombination mechanism shown in Figure 2.11 is known as 'band-to-band' recombination. There are other forms of radiative recombination as well, such as exciton and donor acceptor pair recombination, which are observed in CdTe solar cells. Below these radiative recombination mechanisms will be discussed in more detail.

Band-to-band recombination

In this mechanism when the electron beam hits the sample it can promote the electron from the valence band to the conduction band, leaving a hole in the valence band. Those free electrons and holes can exist for a period called carrier 'lifetime' and after this time they can recombine and emit a photon. In this kind of recombination, the energy of the recombination photon is equal to or above the band energy. (the above bandgap luminescence is however typically observed at room temperature) [72]. The recombination rate can be described as the number of recombination events per unit volume and unit time. The recombination rate is given by:

$$R = B(np - n_i^2) \tag{2.3.1}$$

Where B is the radiative recombination efficiency, np is the product of electron and hole

concentrations that are generated under the electron beam and n_i is the intrinsic carrier concentration. From the formula, we can see the proportional relationship between the recombination rate and the number of excess electrons and holes. This means when the number of excess electrons and holes increases, the rate of recombination will increase as well [74].

Exciton recombination

Another type of radiative recombination is exciton recombination. In an inorganic pure semiconductor, a free exciton consists of a free electron-hole pair moving inside the crystal, and they are attracted to each other by a Coulomb force (Wannier-Mott exciton) [72]. As a result of this Coulomb force, the photon for this type of recombination has energy less than the bandgap. The exciton should have a strong attractive energy to prevent the binding from being broken by the thermal energy $k_B T$, where k_B is Boltzmann's constant and T is temperature. For this reason, luminescence from Wannier-Mott excitons is typically observed at cryogenic (e.g. liquid nitrogen or helium) temperatures, rather than room temperature, as room temperature can break up the exciton. Therefore, low temperature and a pure crystal are necessary conditions for free excitons to exist in a material such as CdTe. When a valence band electron is excited by the highly accelerated electron beam in a SEM, the electron is not promoted to the conduction band because of the Coulomb force. This force makes the energy less than the band gap energy and the electron will occupy a state within the band gap. This state is called the ($E_{exciton}$) exciton energy level and is slightly lower in energy than the conduction band minimum (E_c). The exciton binding energy is given by:

$$Exciton\ binding\ energy = E_C - E_{exciton} \tag{2.3.2}$$

This energy is small (few meV for most inorganic semiconductors), and the exciton can be broken up by just gaining a small amount of thermal energy. At room temperature, the thermal energy can break this small Coulomb attraction energy, but at low temperature, the exciton does not break and the electron in the exciton state can recombine radiatively with the hole in the valence band. The recombination photon energy is smaller than the band gap and equal to the separation between exciton energy and valence band maximum. Therefore, the exciton peak appears sharp in a luminescence spectrum as it is related to a very specific photon energy. There can also be bound excitons which appear in an extrinsic crystal, because impurity atoms act as traps for the free excitons. In particular, the free exciton can bind

with impurity atoms to give DX donor bound or AX acceptor bound excitons. The electron energy is below the conduction band and it has less energy compared with free excitons [72].

Donor acceptor pair (DAP) recombination

Donor acceptor pair (DAP) recombination also produces radiative emission; an electron in a neutral donor energy level can recombine with a hole in a neutral acceptor energy level to emit a photon. During the recombination, the donor and acceptor become ionised (D^+ and A^-), resulting in Coulomb electrostatic attraction between them (Figure 2.13,a). Due to the Coulomb attraction, the DAP peak has a broad range of energy values which depend on the distance R between donor and acceptor. The recombination rate of donor-acceptor pairs increases as the distance of separation R decreases, due to the donor and acceptor wavefunctions overlapping more closely. Typically, the observation of DAP recombination requires a low temperature to avoid donor and acceptor ionisation by thermal excitation [72]. When the electron beam in a SEM strikes the material to generate electrons and holes, they will move within the crystal till electrons fill the donor ion state and holes fill the acceptor ion state. Then these two levels are no longer ionised (Figure 2.13,b), and the energy difference between these new two neutral donor and acceptor level is smaller as there is no attraction between them. At this time there is an opportunity for the electron in the donor state to recombine with the hole in the acceptor state. During the recombination process the donor and acceptor levels will return back to the ionised levels again (Figure 2.13,c) [75].

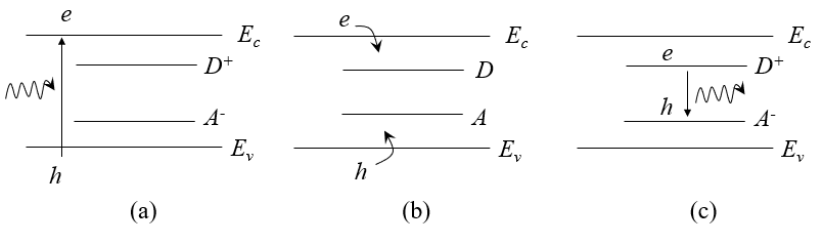

Figure 2.13: *a) Coulomb electrostatic attraction between the ionised donor and acceptor levels, b) Electron fill the donor ion state and hole fill the acceptor ion state, c) shows the emitted photon due to the recombination.*

The equation below shows how the donor acceptor pair photon energy (E_{DAP}) depends on r where r is the distance between the donor and acceptor levels. [72].

$$E_{DAP} = (E_D - E_A) + e^2/(4\pi\varepsilon_o\varepsilon_r r) \tag{2.3.3}$$

where E_D is the neutral donor energy and E_A is the neutral acceptor energy, e is the electronic charge, ϵ_0 is the permittivity of free space, ϵ_r is the material dielectric constant and the last term is the Coulomb interaction of the ions in the final state. There are many r separation values which will lead to a broad emission peak [72].

Cathodoluminescence of CdTe solar cells

Cadmium telluride (CdTe) is a direct band gap semiconductor that exhibits luminescence behaviour. The luminescence peaks of CdTe can vary depending on the defects, and sample preparation conditions. At room temperature (300 K), CdTe emits light as a single broad peak in the wavelength range of approximately 700 to 900 nanometres near the band gap energy of around 1.5 eV, as shown in Figure 2.14. Emission peaks at energies smaller than the band gap are not seen at room temperature. This is because defect states within the band gap are relatively shallow for CdTe and are therefore ionised at room temperature. However, at cryogenic temperatures (liquid nitrogen or helium) sub-band gap emission peaks are visible in the luminescence spectrum, and therefore provide more detail about the optoelectronic properties of the material [76].

Consonni *et al.* [77] investigated Cl doping of thick polycrystalline CdTe layers grown by close space sublimation using photoluminescence (PL) and cathodoluminescence CL. Figure 2.15 (a) shows CdTe PL spectra at 4 K (liquid He temperature). An exciton emission region was observed in the wavelength range between 772-792 nm. This range includes a free exciton emission peak at 1.596 eV, donor-bound exciton DX emission peak at 1.593 eV, and acceptor-bound exciton AX at 1.590 and 1.587 eV. A donor acceptor pair (DAP) region was also observed in the range between 792-820 nm, which includes two emission peaks at 1.557 and 1.552 eV. The region between 820-860 nm is called the deeper emission region, which represents a second DAP region and is less important. Moreover, an excitonic emission peak was observed at 77 K (liquid nitrogen temperature) at 790 nm and a broad DAP peak at 855 nm, as shown in Figure 2.15 (b) [77].

Mendis *et al.* [78] used cathodoluminescence to probe individual grain boundaries (GB) in CdTe. They conclude that exctions are quenched at GBs, but there was a higher fraction of DAP recombination at GBs. Figure 2.16 a shows the panchromatic image with high cathodoluminescence (CL) intensity in the grain interiors (GI) and low CL intensity at grain boundaries (GBs) for a CdTe solar cell device. The drop in CL intensity at GBs means a higher level of non-radiative recombination. The CL spectra for GI and GB at 12 K temper-

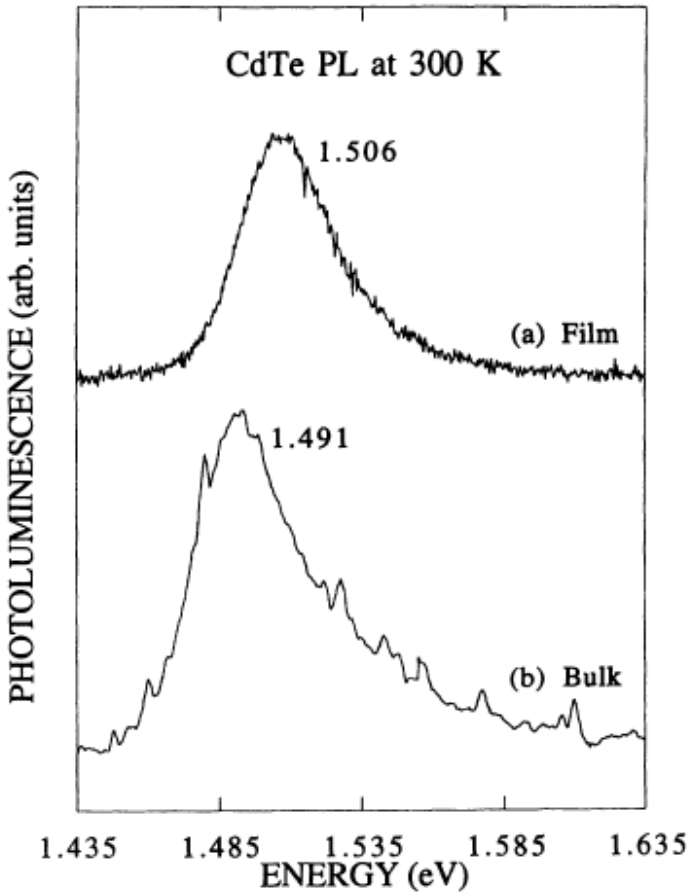

Figure 2.14: *a) Photoluminescence (PL) emission spectrum at room temperature 300 K.* [76]

ature are shown in Figure 2.16.b. A neutral acceptor bound exciton (A^0X) was observed at 779 nm. Other peaks corresponding to an electron to acceptor eA^0 and donor-acceptor pair DAP (DAP_1) radiative transition appeared at 795 nm and 799 nm respectively. A second, much broader DAP peak (DAP_2) was observed at the wavelength range 850-950 nm. It was observed that the relative intensity of (DAP_2) was enhanced at grain boundaries; see Figure 2.16 [78].

In CdS/CdTe photovoltaic devices, the interface between the CdS and CdTe layers plays a crucial role in device performance. The microstructural stability of this interface and the diffusion of sulfur within the device are important factors to consider. Cathodoluminescence microscopy was used by Taylor *et al.* [79] to demonstrate how sulphur diffuses into a CdS/CdTe device [79]. Figure 2.17 shows the CL spectrum measured close to the CdS/CdTe interface (labelled CdTeS- black spectrum) and further away from the interface where S diffusion is negligible (labelled CdTe- red spectrum). The two CL spectra show evidence for

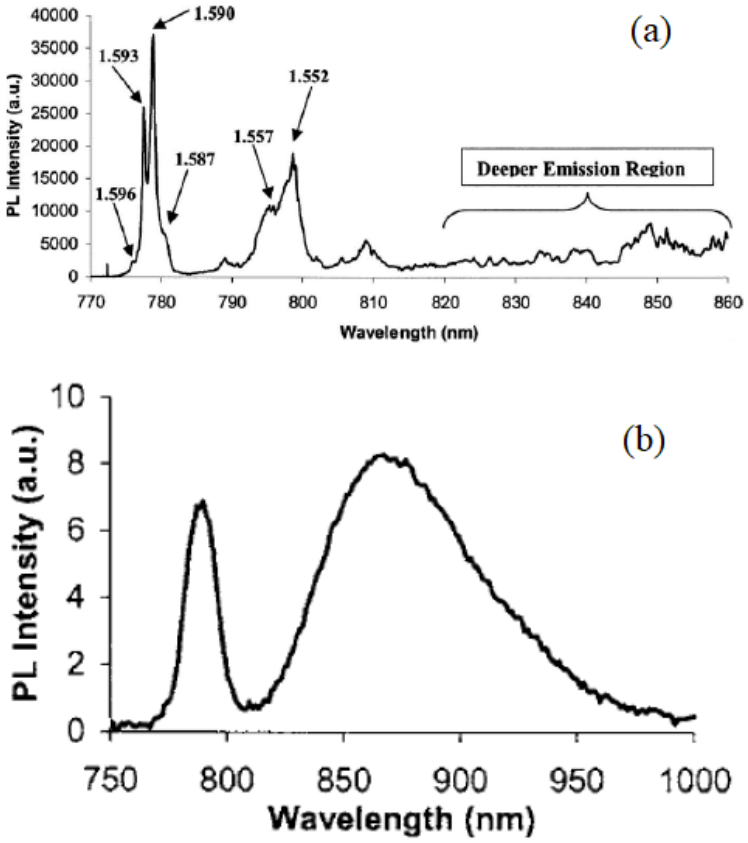

Figure 2.15: *PL spectrum for Cl doped CdTe at 4 K, and at 77 K.* [77]

a broad peak emission (800-900 nm in CdTe) (850–950 nm in CdTeS), which correspond to donor acceptor pair recombination. The other sharp peaks in the range (750-850 nm) are bound excitons peaks. A red-shift of the CdTeS spectrum was observed due to sulphur alloying with CdTe. This red shift of the CL spectrum was used to map the sulphur inter-diffusion region around the CdS/CdTe interface, as well as provide evidence for faster sulphur diffusion along grain boundaries in the Cd(Te,S) absorber layer.

Other luminescence studies have shown non-radiative recombination at grain boundaries, even after chlorine treatment [80]. Low-temperature cathodoluminescence (CL) spectrum imaging with nanoscale spatial resolution was used to examine defects at grain boundaries (GBs) and grain interiors (GIs) in both as-deposited and $CdCl_2$ treated CdTe thin films. The impurity concentration is higher at grain boundaries compared to the grain interior. The results showed that GBs in as-deposited films are active recombination centers and are thus harmful to solar cell performance. CL contrast measurement at GBs reduced for the $CdCl_2$ treated film, which indicates Cl passivation of defects at GB. However, the $CdCl_2$ treatment is not perfect and does not remove all GB recombination, so that GB recombination may still

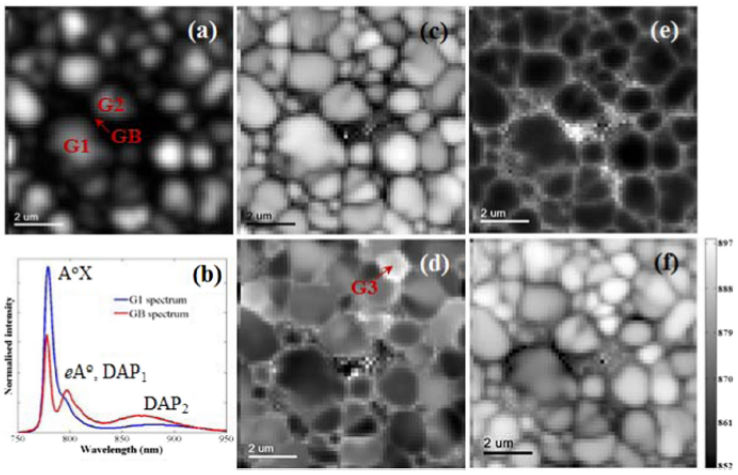

Figure 2.16: *(a) CdTe hyperspectral panachromatic image, (b) CL spectrum from the grain interior GI and grain boundary GB in (a), (c,d,e) normalised intensity distribution for A^0X, eA^0/DAP_1 and DAP_2 radiative transitions respectively. (f) is the central wavelength of the DAP_2 peak as a function of spatial position. All data were acquired at 12 K temperature. [78]*

be the limiting performance in $CdCl_2$ treated devices [80].

Moseley *et al.* [81] used high-resolution cathodoluminescence (CL) spectrum imaging on beveled surfaces of CdTe. They found that due to the chlorine treatment, there is a reduction in the grain boundary recombination through the absorber layer. Figure 2.18 shows CL spectra from grain boundary and grain interior in CdTe; the exciton peak is the higher energy band and the lower-energy band is due to donor acceptor pair (DAP) and electron to acceptor (eA^0) transitions. The exciton band intensity is reduced at the GB relative to the GI. Simulated low temperature spectra also confirm higher GB concentrations of (radiative) donor and acceptor defects.

$CdCl_2$ treatment is a common method employed to improve the performance of CdTe solar cells by passivating any existing defects and enhancing the optoelectronic properties of the material. Cathodoluminescence imaging allows us to investigate the changes in the luminescent properties of the CdTe film before and after $CdCl_2$ treatment. By comparing cathodoluminescence images, we can observe variations in the intensity of the luminescence signal associated with defects. Biduad *et al.* [82] studied the effects of $CdCl_2$ annealing by using high-resolution hyperspectral cathodoluminescence mapping. An increase in grain size as well as passivation of both grain boundaries and grain interior defects has been observed, which led to an increase in luminescence intensity and diffusion length overall.

Recent improvements in CdTe efficiency been achieved through the incorporation of chlorine

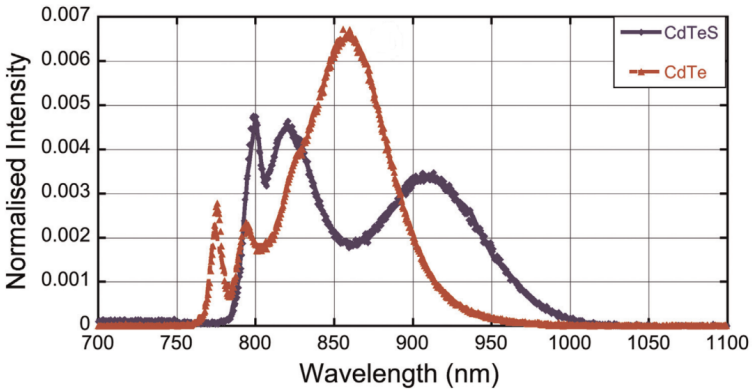

Figure 2.17: *10 K temperature CL spectra acquired near the CdS/CdTe interface (CdTeS) and near the back contact surface (CdTe) in a CdS/CdTe thin-film solar cell device. [79].*

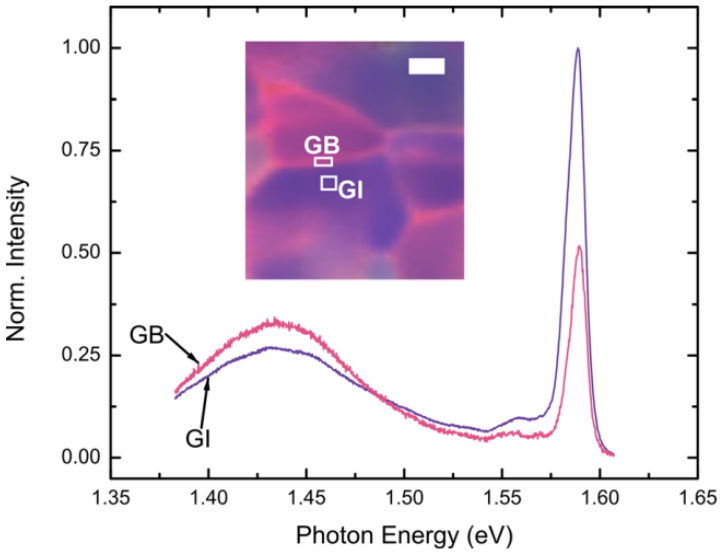

Figure 2.18: *Plots of the GB and GI CL spectra normalized to the maximum GI intensity of the back of CdTe layer [81].*

and selenium, since both Cl and Se have a defect passivating effect in CdTe solar cells [48,51]. The addition of selenium to the front of the CdTe absorber layer improved the efficiency from 19.5 to 22.1% [48]. Selenium diffused into the CdTe layer creating a CdSeTe alloy that has a lower bandgap and therefore increased long wavelength absorption. Fiducia *et al.* [48] used high-resolution cathodoluminescence (CL) microscopy and secondary ion mass spectrometry (SIMS) to show that selenium alloying helps reduce the density of deep level defect states, thus reducing recombination and improving the overall efficiency of the solar cell. They observed increases in the luminescence intensity and diffusion length in the alloyed material, indicating that selenium passivates the defects in the bulk of the absorber layer. They noticed from SIMS that selenium can diffuse from the CdSeTe layer into the CdTe through the grain boundaries,

followed by slow diffusion into the grain interiors. The SIMS results were correlated with CL imaging of the bevel in the same area. The panchromatic CL map shows that luminescence intensity is relatively low at the top of the bevel in the CdTe region, compared to the bottom of the bevel (i.e. CdSeTe region) as shown previously in Figure 1.22. The plot of selenium concentration versus luminescence intensity shows that the CL intensity generally increases when the Se concentration increases. This indicates that selenium passivates the defects and decreases the non-radiative recombination lifetime in the alloyed material. Further evidence that shows that selenium passivates bulk defects in CdSeTe alloys, is found from an anlaysis of the diffusion lengths, which is longer in grains with higher Se concentrations compared to pure CdTe grains [48].

Fiducia *et al.* [48] also combined the same area of the SIMS map with the room temperature CL photon emission energy (i.e. effective bandgap), and found there is a steady decrease in the effective bandgap from 1.46 eV in the CdTe region (yellow) to 1.36 eV in the CdSeTe region (purple) as shown in Figure 2.19 a,b. The effective bandgap has been plotted as a function of the selenium concentration to show the bowing shape of the band gap variation (Figure 2.19 c). This decrease in the bandgap correlates with a rise in the material luminescence efficiency, as shown in the effective bandgap versus the total CL signal plot (Figure 2.19 d) [48].

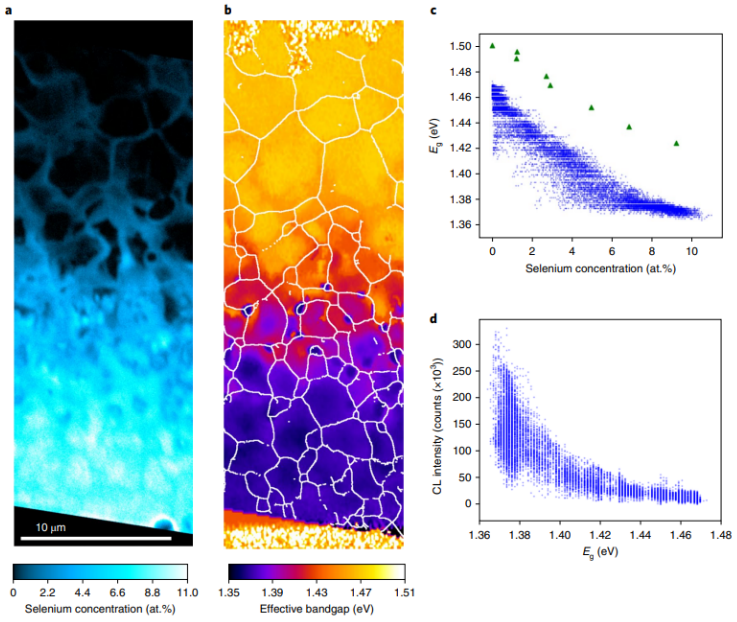

Figure 2.19: *(a) SIMS map of the selenium concentration on the bevel surface of a CdSeTe-CdTe solar cell device. (b) A map of the peak CL emission energy on the same area as (a). (c) A plot of the effective bandgap versus selenium concentration at each point on the bevel. (d) A scatter plot of the effective bandgap versus panchromatic CL signal at each point on the bevel [48].*

2.3.2 Electron backscattered diffraction (EBSD)

Electron backscattered diffraction is a technique that is used to study the local crystallographic data of the material. It is a useful tool to investigate the crystal structure, grain sizes, and crystallographic orientation of the grains in the sample. The signal in electron backscatter diffraction (EBSD) is based on Kikuchi diffraction patterns, which appear in the angular distribution of backscattered electrons (BSEs) in a scanning electron microscope [83, 84]. In an EBSD measurement, the sample must be very flat and well-polished, and the sample stage be tilted by 70 degrees so the electrons can be backscattered more easily (Figure 2.20). The electron beam typically has a voltage of 10 to 30 kV and a beam current of 1 to 50 nA. The primary electron beam interacts with the material surface to produce backscattered electrons. The backscattered electrons lose little energy and will pass through different paths causing constructive or destructive interference (e.g. backscattered electrons at the Bragg angle to the crystal planes will undergo constructive interference). A phosphor screen is placed at a short distance from the inclined sample so that the diffraction pattern is imaged on the screen. The phosphor screen converts the backscattered electron pattern into light which is detected by a charge couple device. The image depends on the wavelength of the incident electrons and the distance between the sample and the phosphor screen. Therefore, EBSD allows us to study the structural characteristics of the sample by seeing how the patterns of a sample are shaped [68, 85]

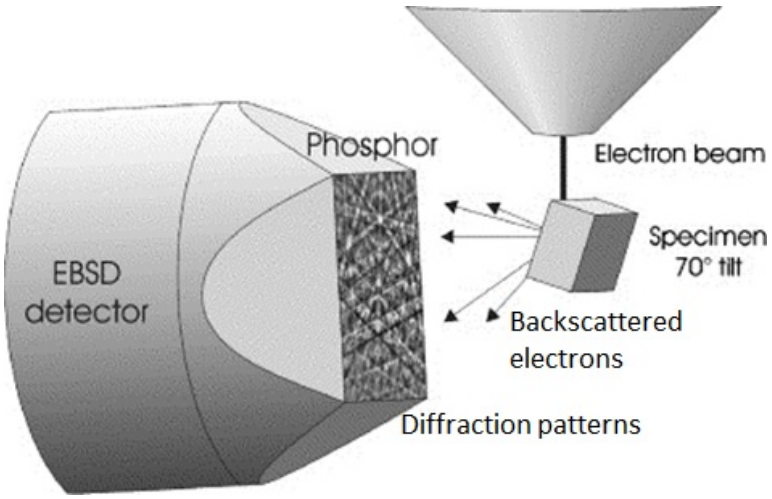

Figure 2.20: *Schematic representation of an EBSD setup. [86]*

Kikuchi bands

The pattern formed on the phosphor screen due to the backscattered electrons in the sample is known as a Kikuchi pattern. The incident electron beam is focused on the sample surface and elastic scattering of the electron beam induces the electrons to diverge from a point just below the surface of the sample. These electrons impinge on crystal planes in all directions. A backscattered electron that fulfils Brag's law for a given plane generates two cones that are from opposite sides of the plane. These cones are produced for every family of lattice planes. When these cones intercept the phosphor screen they appear as a band of intensity, called 'Kikuchi' bands. Because of the small diffraction angle and small electron wavelength, these cones appear as straight bright lines on the screen [87]. The Hough transform is used to identify Kikuchi bands which are observed in the diffraction patterns. Essentially the Hough transform is an image processing algorithm which detects Kikuchi lines within an image as shown in Figure 2.21. The location of a Kikuchi band is identified as the bright peak in Hough space. A peak detection algorithm is used to identify the most intense peak and to neglect other possible false peaks. The diffraction pattern of crystals can thus be analysed to see where the actual peaks are. This process is completed by overlaying a pair of lines corresponding to each peak in the Hough transform. The lines and peaks are indexed to reveal the crystallographic information about the sample [68].

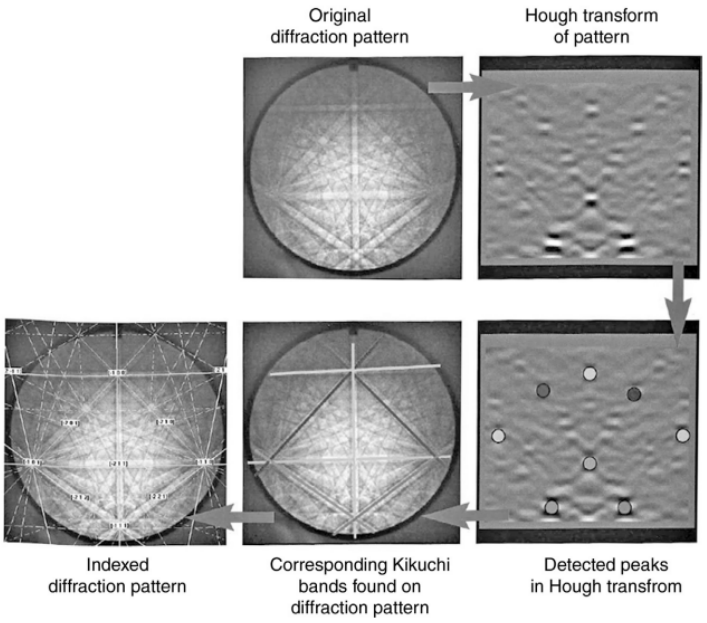

Figure 2.21: *EBSD process to determine crystallographic properties using Hough transforms. [68]*

Stereographic projection

Stereographic projection is a mapping technique used to project a three-dimensional crystal onto a two-dimensional plane while preserving the angle between planes [88]. In stereographic projection, a crystal is placed at the center of a sphere. Considering this sphere rests on a flat surface, it is assigned north (N) and south (S) poles. The surface normal for a given crystallographic plane intersects the northern hemisphere at point p (Figure 2.22). The North pole will be in the middle of the flat surface, while the edges of the circle are defined by the lines that pass from the South pole through the equator of the sphere. Therefore, the result is a two-dimensional projection of the spherical object onto the plane. The projected image will typically distort the size, shape, and distances between objects on the sphere. However, the angles between lines on the sphere are preserved in the projection [89].

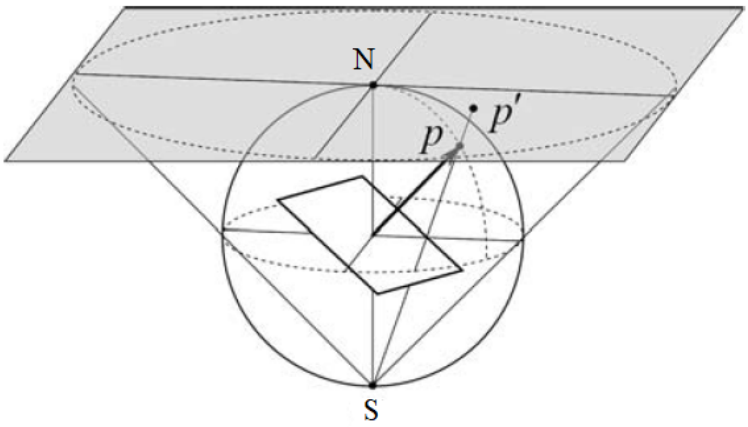

Figure 2.22: *A map showing projecting a point p on the surface of a sphere to point p' in a plane by stereographic projection. [87]*

When the poles of a particular crystallographic plane are considered, and the hemisphere is projected into two dimensions, a pole figure is obtained. Pole figures are used in crystallography to visualize the distribution of crystallographic orientations in a material. They provide valuable information about the preferred orientation, which reveals the orientations of particular crystallographic planes rather than of individual crystals. One point per crystal provides a complete description of the discrete poles in a polycrystalline sample. A cluster of points in this plane can be used to represent a distribution of poles. [87]. The pole figure displays sample directions that are aligned to a specific crystallographic pole. An inverse pole figure shows the crystallographic poles that are aligned with a given sample direction. Figure 2.23 shows the pole figure, inverse pole figure and the standard stereographic triangle for {111} cube texture. The inverse pole figure for the cubic system is divided into twenty-four

stereographic triangles, which contain the crystallographic directions {hkl}.

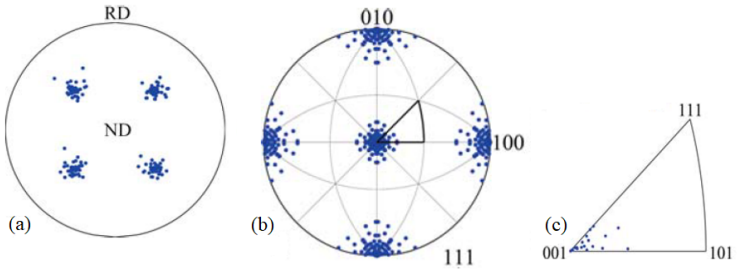

Figure 2.23: *{111} pole figure for a cube texture (a), a normal-direction inverse pole figure for the cube texture (b), and (c) the standard stereographic triangle of the cube texture. 'ND' and 'RD' refer to normal direction and rolling direction respectively. [87]*

2.4 Focused Ion Beam Scanning Electron Microscopy

Focused ion beam (FIB) microscopy is one of the most advanced and precise techniques for analyzing materials. The main parts of a typical FIB instrument are the vacuum system and chamber, liquid metal ion source, ion column, and detectors [90]. FIB instrument is routinely combined with a scanning electron microscope to form a FIB/SEM dual platform instrument. A schematic diagram of a typical FIB instrument is shown in Figure 2.24. In FIB/SEM dual platform instrument, FIB is mounted at 52° angle with respect to vertical. As the ion beam is used for analysis of the sample a vacuum system is required. At higher pressure interaction of the ion beam with gas molecules occur because the mean free path of the ions decreases. The pressure is decreased to the point where the mean free path of the ions increases to the extent that the ions will transverse the distance to the sample with barely any collisions occurring with gas molecules [91].

By using a liquid metal ion source, FIB can be made capable of small probe sputtering. The liquid ion source can provide a source of ions approximately 5 nm in diameter. There are various metals and alloys that are used in liquid metal iron sources. The commonly used LMIS (liquid metal ion source) is gallium (Ga). It is used because it has a low melting point that is 29.8 °C, which minimises the possibility of a reaction between the tungsten needle of the LMIS and Ga liquid. Also, gallium has low vapour pressure at its melting point, so that the source life is long.

The ion column typically has two lenses, i.e. condenser lens and an objective lens. The condenser lens is used to demagnify the ion source and the objective lens is used to focus the ion beam at the sample surface. Figure 2.24 shows the ion column with a set of apertures that

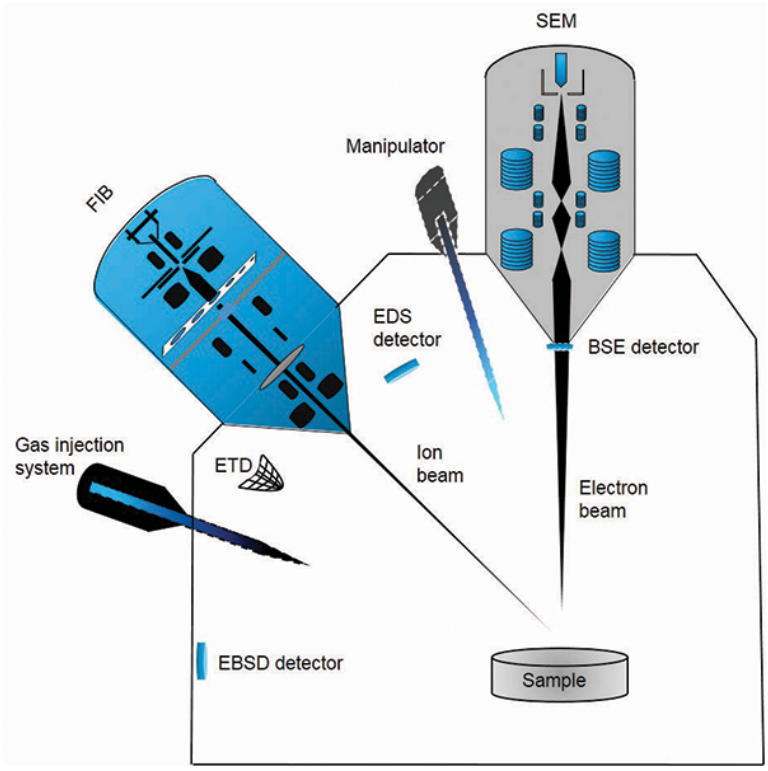

Figure 2.24: *schematic diagram of FIB/SEM. [92]*

have various diameters. The varying diameter help in defining probe angle, and therefore a range of currents from a few pico-amperes to as high as 20 or 30 nA can be obtained [91]. In FIB the ion column is equipped with electrostatic lenses rather than magnetic lenses, because ions are heavier and therefore hard to deflect compared to the electrons. When ions strike the surface it will cause a collision cascade in the sample resulting in the ejection of atoms from the surface. This process involving sputtering of the material is known as ion milling. Material deposition processes can also be carried out using the ion beam. For this purpose, a small needle is inserted into the sample chamber and a gaseous precursor is leaked into the vacuum chamber through this needle. When an ion beam is positioned in the vicinity these precursor gas molecules decompose and local material deposition occurs [90].

Combining the capabilities of the FIB/SEM, to remove material with the ion beam and to obtain images with the electron beam, three-dimensional (3D) models of the sample can be constructed. For this purpose the focused ion beam removes some material from a cross-section, moving it slightly further into the sample and the electron beam acquires the corresponding image of the new cross-section surface. Repeating this process iteratively gives a series of two-dimensional (2D) images, taken along the third axis of the sample. A drawback of this technique is the long acquisition time, depending on the material and volume to be sampled.

Typically, overnight runs are necessary. Furthermore, the method is destructive, meaning that the sample is lost during data acquisition.In addition to imaging with the ion beam, the FIB is frequently used to prepare samples for SEM and transmission electron Microscopy (TEM) [93].

2.5 Transmission Electron Microscopy (TEM)

Transmission electron microscopy (TEM) is one of the most effective tools for microstructural analysis, including crystal structure and chemical information of the sample, because of its high spatial resolution. This high spatial resolution is the result of the small interaction volume, as the sample thickness should ideally be less than 100 nm. Thinner samples show little scattering which is useful for providing a good-quality image, but in thick samples multiple scattering dominates causing image blurring. Moreover, the TEM uses a high energy beam of electrons (e.g. 200 keV), so that the majority of the incident electrons are able to transmit through the thin sample with a low possibility of scattering. This creates a small interaction volume. In detail, a beam of high energy electrons is transmitted through an ultra-thin specimen under a very high vacuum that is 10^{-4} Pa at the specimen region. The electron beam interacts with the sample and an image is formed using the electrons transmitted through the specimen. The image is magnified and focused on to an imaging device such as a phosphor screen or CCD camera [94].

The main principle of transmission electron microscopy is shown in a schematic diagram in Figure 2.25. The TEM consists of an emission source that is made from a material which has a high melting point and low work function, such as tungsten. When a high voltage in the range 100 to 200 kV is applied to the gun, it emits the high energy electron beam. Due to the relatively broad emission area of the electron gun, two condenser lenses control the incident beam. The first condenser lens demagnifies the beam size while the second condenser lens can create either a parallel or focused beam. Electromagnetic lenses are used in the TEM, where a magnetic field is used to deflect the negatively charged electron beam. As a result, the entire specimen can be illuminated using a parallel electron beam, or only a small region analysed by focussing the beam to a 'spot' [95].

The transmitted electron beam after passing through the sample will be focused by the objective lens into an image or diffraction pattern. The image or diffraction pattern is magnified further using a series of projector lenses, and finally recorded on a phosphor screen or charge-coupled device (CCD) camera. The objective lens forms a diffraction pattern at the back

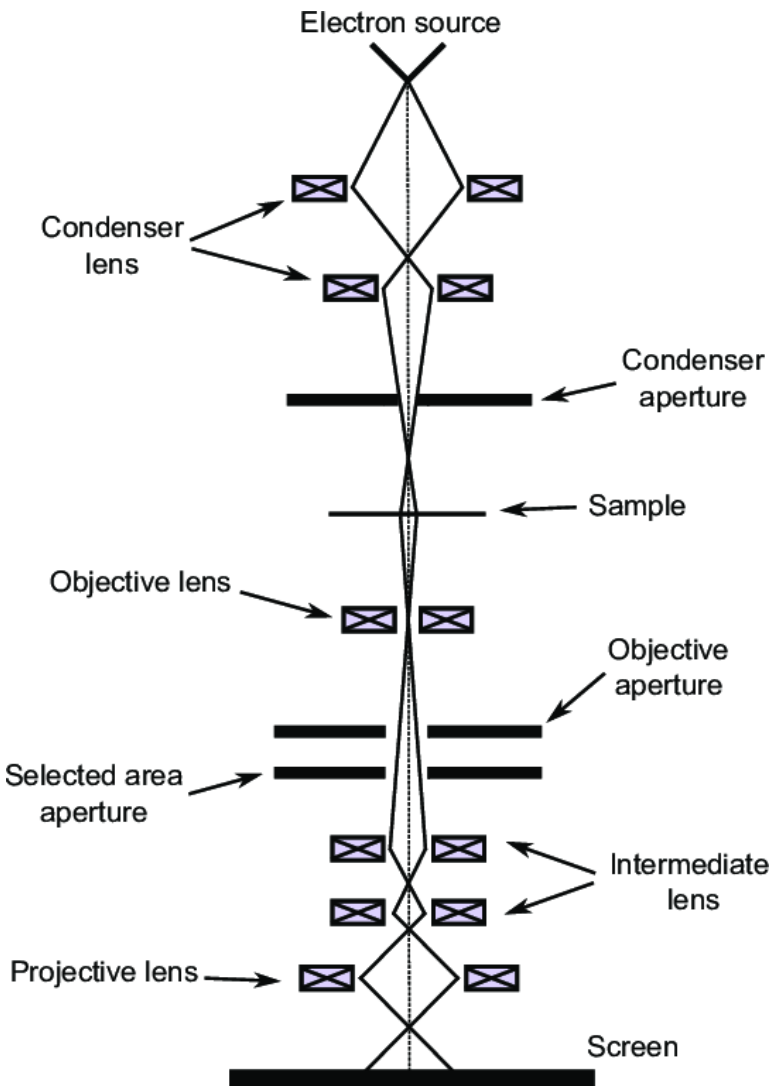

Figure 2.25: *Schematic diagram of a transmission electron microscope. [96]*

focal plane, also known as the diffraction plane. For imaging, the objective lens will focus all transmitted and scattered electrons from one point of the sample into a conjugate point in the image plane, as shown in Figure 2.26. For diffraction, those rays scattered in a given direction from all points in the sample area are collected into a single point. This is at the back focal plane of the objective lens and is where the diffraction pattern is formed (Figure 2.26). The diffraction pattern provides us with crystallographic information. The intermediate lens can select either the image or the diffraction pattern (Figure 2.25).

The objective lens contains an aperture which can be used to select either the unscattered (transmitted) or scattered beams for imaging. Depending on which beam is selected, either a bright field or dark field image can be formed. In bright field imaging mode, the aperture selects the unscattered (transmitted) electron beam and blocks the scattered electrons. Areas with higher atomic number will appear dark due to increased electron scattering; however,

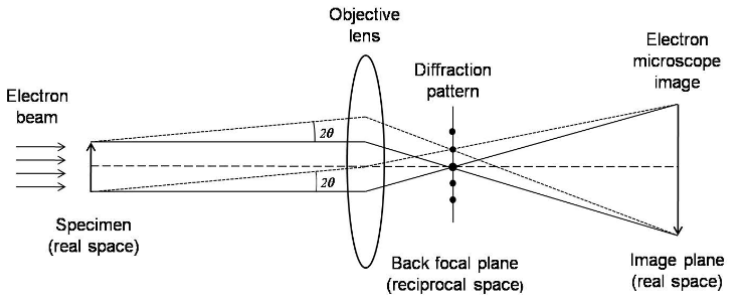

Figure 2.26: *Objective lens ray diagram and its relation to imaging and diffraction in the TEM. [97]*

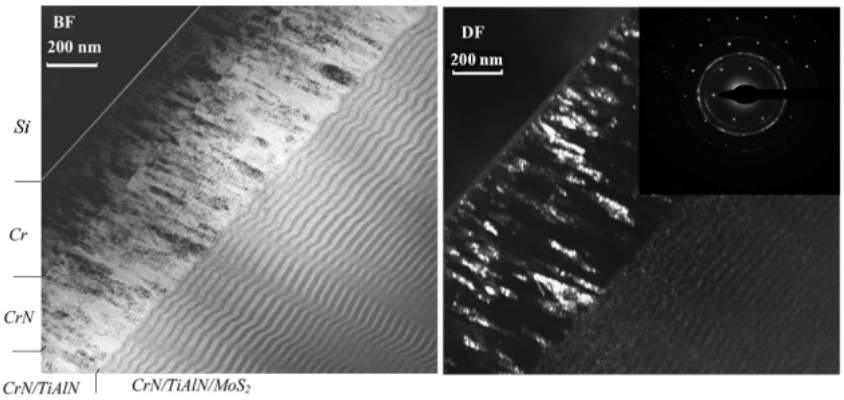

Figure 2.27: *Cross-sectional TEM bright field and dark field images of CrN/TiAlN multilayered structure. [98]*

the light areas having low atomic number will appear bright, such as the vacuum around the sample. In contrast for dark field imaging mode, the aperture selects the scattered electron beam, and areas with higher atomic numbers will appear bright due to electron scattering. Therefore, areas without electron scattering (the vacuum surrounding the sample) will appear dark [97]. As an example, Figure 2.27 shows the bright field and dark field cross-sectional TEM images of a CrN/TiAlN multilayer structure [98].

2.5.1 High Resolution Transmission Electron Microscopy (HRTEM)

Transmission electron microscopes have an imaging mode called high-resolution electron microscopy (HREM), which enables direct imaging of the atomic structure of the sample. It is a powerful tool to explore the atomic structure of materials. In both bright and dark field imaging modes, there was a single beam passed through the objective lens, ether transmitted beam (bright field) or scattered beam (dark field), which gives us the amplitude of the respective beam in the formed image. If we use a large-diameter objective aperture it is possible for more than one beam (transmitted and scattered beams) to pass through the

objective aperture. The interference of the multiple beams reaching the image leads to lattice fringes, which are regions of constructive and destructive interference. As each beam has its own phase, the method is called phase contrast imaging, where both phase and amplitude contribute to form the image.

Atoms in the crystal lattice work as a diffraction grating (which has more than one slit), where the constructive and destructive interference produces intensity maxima and minima that create an image of the lattice with different contrast (phase contrast). The image can provide useful information regarding the periodicity and orientation of the crystal lattice, and reveal information about the atomic structure of the sample [99]. It is especially useful for imaging defect structures such as interfaces and grain boundaries, where traditional crystallographic methods, such as diffraction, are more complicated to interpret.

2.5.2 Scanning Transmission Electron Microscopy (STEM)

Scanning transmission electron microscopy (STEM) is another highly versatile technique that is used extensively in materials characterisation. It has been mentioned previously that scanning electron microscopy works by rastering the beam across the sample. STEM has the same principle, where the electron beam is focused to a small spot and moved across the sample in a similar way to SEM, and signals are collected point by point to create images or maps [100], [101]. Bright field (STEM) imaging is used as a general imaging technique for investigating samples. To form this image, a photomultiplier tube (PMT) detector is placed along the electron optic axis (Figure 2.28), so that the intensity of the unscattered beam is detected. Dark field STEM images are formed from electrons that have been scattered by the sample, using an annular detector (Figure 2.28). The resulting images are also known as annular dark field (ADF) images.

Bright-field and dark field imaging modes can be sub-divided into other modes that give specific information. For example, in high-angle annular dark-field (HAADF) mode, where elemental contrast can be obtained, the focused electron beam is scattered by the atomic nuclei of the sample. Therefore, for a sample of uniform thickness, bright regions in a HAADF image correspond to regions of higher atomic numbers. For atomic number contrast the inner angle of the annular detector must be at least three times the STEM probe convergence semi-angle θ (Figure 2.28). In addition to imaging, STEM can also detect the X-ray signal emitted by the sample at each scan position. This enables extracting chemical composition maps from regions of interest at high spatial resolution [103], [104].

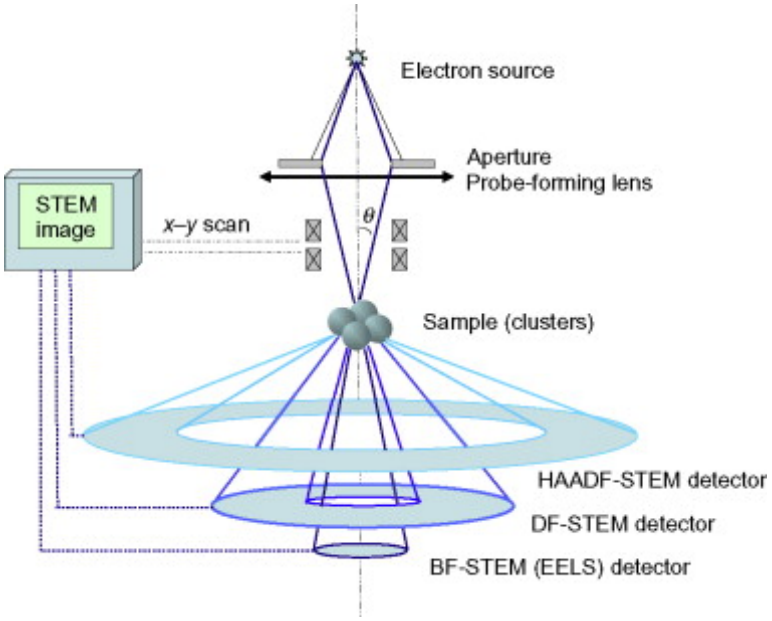

Figure 2.28: *schematic diagram of STEM equipped with bright field STEM detector and annular dark field STEM detector. [102]*

2.5.3 Bragg's Law and Diffraction

Materials are built from atoms. Understanding the structure and properties of materials is based on an understanding of how atoms are arranged. Crystals are solid materials with a very regular structure. This means the atoms are arranged in a way that is a periodically repeating three-dimensional object. A crystal lattice is a pattern of atoms that has the same unit cell repeated throughout space. The unit cell is defined by three fundamental lattice basis vectors **a,b** and **c**, with angles α, β and γ between two given lattice basis vectors [105].

Diffraction is a wave interference phenomenon. When an electron interacts with the sample and is scattered by atoms in the crystal, the interference of two scattered electrons forms the diffraction pattern. In order to form these diffraction patterns, we must have more than one scattering center. The diffraction pattern is a series of 'spots' (intensity maxima), where each spot represents the intensity scattered from a unique crystal plane. The principle of electron diffraction in a crystal is described by Bragg Law. In detail when planes (hkl) in the lattice are exposed to the electron beam, electrons are scattered by the regular arrangement of atoms; the scattered waves can interfere leading to diffraction.

Figure 2.29 shows two parallel electron waves incident on crystal atomic lattice planes at the angle θ, producing scattered electron waves at the same angle (the incident electron has a wavelength smaller than the crystal planar spacing). At the Bragg angle the electron waves interfere constructively, which means the scattered waves have the same phase and therefore

maximum intensity, while if the two waves are out of the phase, the intensity is destroyed (destructive interference). The difference of path length between two scattered waves is 2d sinθ. For constructive interference therefore:

$$2dsin\theta = \lambda \tag{2.5.1}$$

where, λ is the electron wavelength, θ is the angle of the incident electrons on the crystal plane, and d is the distance between the crystal planes (hkl). Equation (2.5.1) is known as Bragg's law.

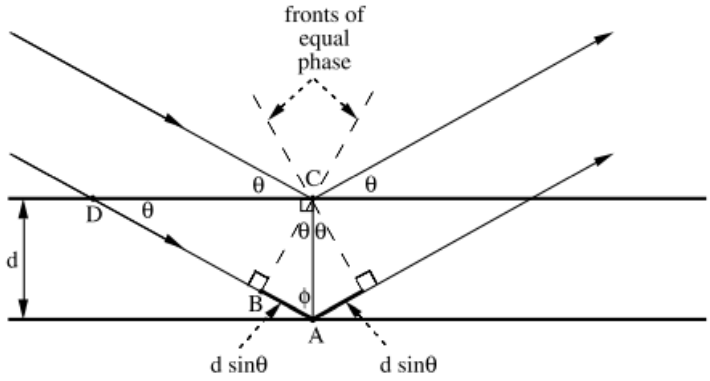

Figure 2.29: *Bragg's Law geometry showing the interference of a wave scattered from two planes separated by a spacing (d). [106]*

Therefore, we can explain diffraction patterns in terms of a diffraction vector **g**, which is associated with the crystal plane (hkl), where **g** is parallel to the (hkl) surface normal and has magnitude $1/\mathrm{d}_{hkl}$. The diffraction pattern is a cross-section of reciprocal space. The reciprocal lattice is a three-dimensional array of points. It is simply a mathematical construction to allow us to explain the diffraction patterns. Reciprocal lattices of crystals are defined by three reciprocal-lattice basis vectors. The reciprocal-lattice concept allows us to define a lattice, where all the lattice points correspond to the possible **g** vectors. A set of parallel atomic planes (hkl) can be represented by a point at $1/\mathrm{d}_{hkl}$ from the reciprocal lattice origin in a direction that is parallel to the (hkl) surface normal.

A reciprocal lattice vector is given by the equation

$$r^* = m_1a^* + m_2b^* + m_3c^* \tag{2.5.2}$$

where **a***,**b*** and **c*** are the basis vectors in reciprocal space. These reciprocal space vectors have a length

$$a^* = \frac{1}{a}, b^* = \frac{1}{b}, c^* = \frac{1}{c} \tag{2.5.3}$$

The reciprocal lattice vector $\mathbf{g}_{hkl}$ for a plane is given by:

$$g_{hkl} = ha^* + kb^* + lc^* \tag{2.5.4}$$

where *h,k* and *l* are Miller indices that define the plane (hkl). This plane (*hkl*) cuts the *a*, *b* and *c* axis at *1/h*, *1/k* and *1/l* respectively.

Ewald Sphere of diffraction

This sphere in reciprocal space has a radius $1/\lambda$, and passes through the origin of the reciprocal lattice (point O) as shown in Figure 2.30. When the sphere passes through the reciprocal lattice points the set of planes related to that point will satisfy Bragg's law, leading to intensity in the diffraction patterns. However, if the sphere does not pass through the lattice points, Bragg's law is not satisfied, and there is very little intensity. Therefore Ewald sphere of diffraction shows us how the intensity of the diffracted beam changes when the sample or electron beam is tilted [107]. For a high-energy electron beam in the TEM the electron wavelength *lambda* is much smaller than the crystal spacing d. This means that the Bragg angle θ is very small (Equation 2.5.1). Therefore, in electron diffraction patterns, the reciprocal vectors are all perpendicular to the incident beam direction.

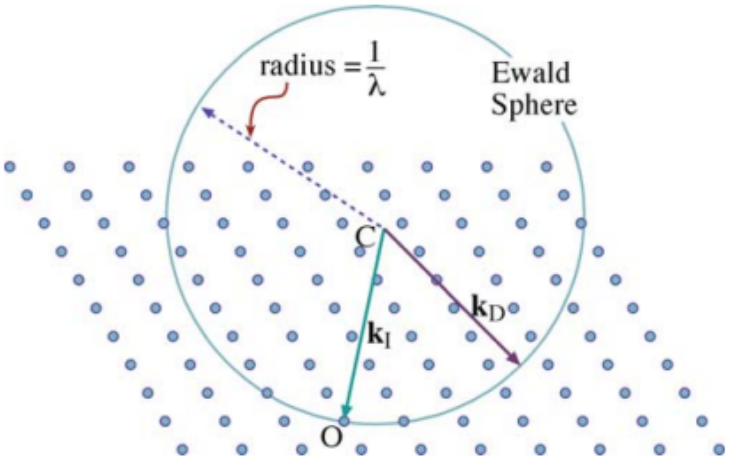

Figure 2.30: *The Ewald sphere of diffraction, which has radius 1/λ, where λ is the electron wavelength. K_I is the incident wave vector. [107]*

Apart from Bragg's law, for a crystal to diffract strongly it must also have a non-zero structure factor. The structure factor F_{hkl} is defined using the following formula:

$$F_{hkl} = \Sigma f_i(\theta) exp[-2\pi i(hu_i + kv_i + lw_i)] \tag{2.5.5}$$

where f(θ) is the atom scattering factor and u_i, v_i, and w_i are the fractional coordinates of atoms in the unit cell. The structure factor effectively represents how scattering from individual atoms in the unit cell interferes with one another. If the structure factor is zero the diffracted intensity is zero despite Bragg's law being satisfied. As an example, for face-centred cubic crystals the structure factor is zero if the Miller indices for the (hkl) plane are mixed, i.e. combination of odd and even numbers. The structure factor, along with Bragg's law, can be used to identify the crystal structure using diffraction.

Chapter 3

Correlated cathodoluminescence and electron backscatter diffraction investigation of CdTe grain boundaries

3.1 Motivation

To maximise the future positive impact of photovoltaic (PV) technology, especially CdTe solar cells as the second most common photovoltaic technology in the marketplace after crystalline silicon, there is a need to develop and improve the device technology to gain more efficiency. Moreover, characterisation techniques, such as cathodoluminescence and electron backscatter diffraction, are critical for investigating and studying the electrical and optical properties of solar cells. A crucial challenge is the limited lifetime of the electron-hole pairs generated by photons absorbed in the solar cell absorber layer, as they recombine either radiatively or non-radiatively leading to lower efficiency [108]. Therefore, minimising non-radiative recombination at grain boundaries is a critical factor to investigate, in order to increase the efficiency of CdTe solar cells.

This chapter aims to combine cathodoluminescence contrast (optoelectrical properties) and electron backscatter diffraction (crystallographic properties), to investigate the effect of grain boundary misorientation on non-radiative recombination [109, 110]. Grain boundaries have lower intensity than grain interiors in a panchromatic cathodoluminescence (CL) image due to higher non-radiative recombination. Therefore, the CL contrast of a grain boundary is a measure of its recombination activity. By performing correlative CL and electron backscattered diffraction (EBSD) analysis on the same grain boundary, we can link grain boundary recombination to its misorientation. This enables an investigation into the role of different grain boundaries (e.g. coincident site lattices vs. regular grain boundaries) on device performance.

The outline of this chapter is as follows. Section 3.2 describes the experimental methodology used to prepare samples suitable for electron microscopy from an actual thin-film PV device. Section 3.3 presents an overall characterisation, i.e. chemical composition, grain size and texture etc., of the sample. Results from correlative CL and EBSD investigation of grain boundaries are then presented in Section 3.4. Following a description of the analysis procedure (Section 3.4.1), results are divided into regular grain boundaries (section 3.4.2) and coincident site lattices (section 3.4.3). In Section 3.5 a more detailed quantitative analysis of the CL intensity profile across grain boundaries is presented. This analysis provides numerical values for the reduced recombination velocity of the grain boundaries, as well as the minority carrier diffusion length in the sample.

3.2 Experimental methodology

The sample used in this chapter was prepared by Dr Jacob Leaver at the University of Liverpool and has a structure of glass/fluorine-doped tin oxide (FTO)/ SnO_2/CdSe/CdTe/Au. The window layer CdSe has a thickness of 100 nm. CdTe was deposited using close-space sublimation under vacuum (i.e. 0 torr nitrogen gas pressure). The sample for scanning electron microscopy (SEM)-CL was prepared by first extracting a 2x1 mm^2 rectangular piece using a Gatan ultrasonic cutting tool. The as-deposited surface is rough due to the underlying CdTe grain structure and must therefore be flattened for CL analysis such that it is free of topographic artefacts. Figure 3.1 shows the precision ion polishing system from GATAN that is used to prepare the sample for scanning electron microscopy.

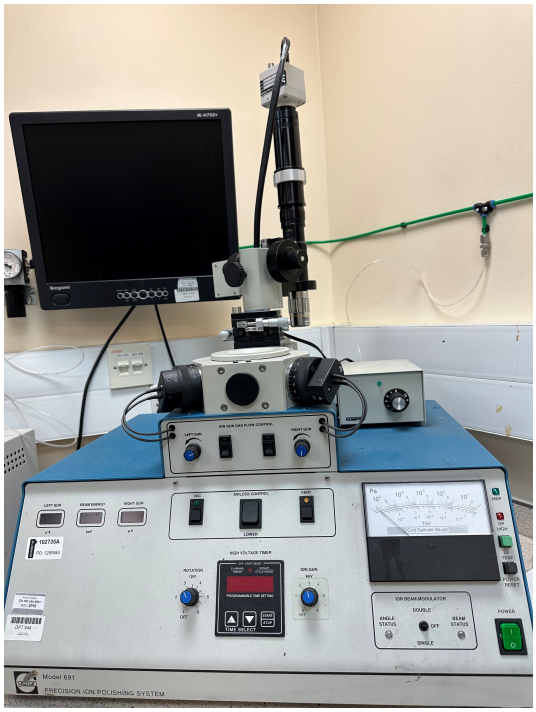

Figure 3.1: *Gatan precision ion-polishing system used for preparing CdTe samples for SEM analysis.*

This system utilises an argon ion beam to selectively remove material from a sample, allowing for precise thinning and polishing. The Gatan precision ion polishing system typically consists of a vacuum chamber, ion source, sample holder, and various controls and monitoring systems. The argon ion polishing is performed by two variable angle ion guns, where each can be adjusted independently with a milling angle between +10° to -10°. The ion source emits a focused beam of argon ions that interact with the sample surface, sputtering away material and creating a polished region. The ion beam energy can be varied between 1 keV to 6 keV,

which allows thinning and polishing procedures to be carefully controlled and monitored to achieve the desired sample thickness and quality. A 2 keV argon ion beam at a low incidence angle (2°) was used for our sample. The sample was then imaged in a Hitachi - SU70 SEM operating at either 15 or 20 kV electron beam voltage and equipped with a GATAN MonoCL system. EBSD instrumentation was located in a different microscope, an FEI Helios 600 focused ion-beam SEM (FIB-SEM), which was operated at 30 kV electron beam voltage.

3.3 CdTe solar cell specimen characterisation

Secondary electron SEM images for the back contact surface of the sample before and after ion polishing are presented in Figure 3.2. The as-deposited surface is extremely rough, due to the underlying grain structure of the absorber layer. After ion-polishing the surface roughness is considerably lower, although there is still some roughness in the form of shallow pits. As we shall see in subsequent sections, the residual surface roughness does not cause any artefacts in the acquired CL and EBSD images. This is likely to be due to the large interaction volume for CL, and because the sample is tilted at a steep angle of 70° for EBSD. Some porosity in the absorber layer was also evident on the surface after polishing. Porosity in close space sublimated CdTe has been reported previously [111].

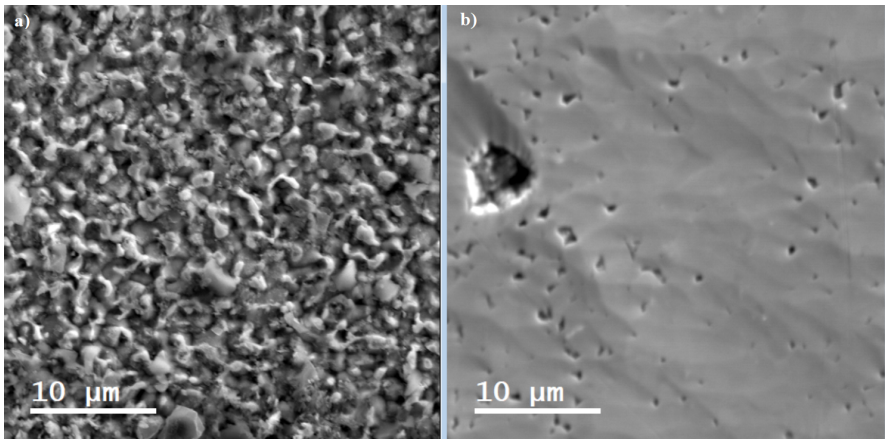

Figure 3.2: *Secondary electron-SEM images for CdTe specimen a) before ion polishing and b) after ion polishing.*

Energy dispersive X-ray (EDX) spectroscopy results (Figure 3.3) for the back surface showed that Cd and Te are the main components in the sample with overall weight 47.13% for Cd, 50.43% for Te and 0.64% for Se. The remaining concentration is due to aluminium (1.80 weight%), which is likely to be an impurity. Although there may be some diffusion of Se from CdSe into the CdTe, the extent of diffusion is not sufficient that it can be detected by a 20

kV SEM electron beam under plan view imaging of the back contact surface. Therefore, for all practical purposes, the grain boundary results presented in this chapter can be identified as being CdTe grain boundaries, with little Se alloying.

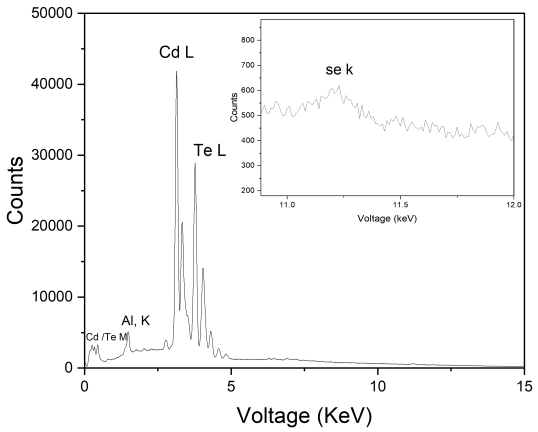

Figure 3.3: *Energy dispersive X-ray (EDX) spectrum of the back surface of a CdTe-CdSe solar cell. The electron beam energy is 20 keV. The inset shows the Se K X-ray peak at 11.2 keV energy.*

Figure 3.4 shows the CL spectrum acquired at room temperature from the back surface of the CdTe thin-film. It appeared as a single broad peak with a maximum at 814.5 nm wavelength. This is equivalent to a photon energy of 1.52 eV, which is similar to the 1.5 eV room temperature band gap of CdTe [112]. The broad tail of the CL emission at wavelengths longer than the peak wavelength indicates that the nature of CL emission is related to band-to-band recombination.

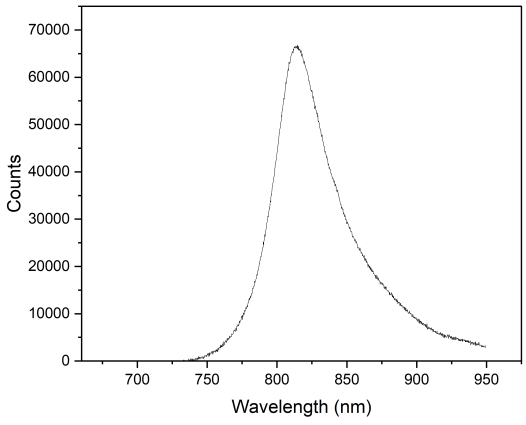

Figure 3.4: *CL spectrum from back surface of CdTe-CdSe. The electron beam energy is 15 keV.*

AztecCrystal software is used to acquire EBSD maps from the CdTe back surface, which provided information on grain size, misorientation angle between grains and its distribution histogram. In particular, the Aztec software uses the Kikuchi pattern at each electron beam scan position to determine the local crystal orientation. This is done using the Hough transform described in Section (2.3.2). Grain boundary misorientation parameters (i.e. angle/axis pair) can be calculated using the crystal orientation of the two grains on either side of the grain boundary [41]. The EBSD map in Figure 3.5a contains 1811 grains with an average grain area of 2.2 μm^2, which varied from a minimum of 1.11 μm^2 to a maximum of 13.08 μm^2. The histogram of grain boundary misorientation angles is shown in Figure 3.5b. Grain boundaries with a low misorientation angle (2-10°) are few in the sample with just 1.63%, but large misorientation angle (>10°) grain boundaries are more common in the sample with approximately 98.4%. The EBSD map allows investigation of the nature of the grain boundaries and the detection of those boundaries belonging to coincident site lattices (CSL). CSL grain boundaries, are expected to have different influences on the overall efficiency compared to regular grain boundaries, as they have high symmetry, and therefore are less harmful to the device performance. In this respect, Figure 3.5a shows how each grain is coloured differently according to its orientation, and contains a mixture of CSL boundaries and regular grain boundaries. 45.1% of the CSL boundaries are of the Σ3 type (60° misorientation angle), as shown in the frequency histogram of Figure 3.5b. Σ3 grain boundary is the most common type of CSL in the sample. However, other CSLs such as Σ5, Σ7, and Σ9 appeared less frequently in the sample, with a number fraction of approximately 2.6% for Σ9, and less than 1% for Σ5 and Σ7 (0.9% and 0.6% respectively). These results are similar to Abou-Ras, et al. [58], as they found two maxima are apparent at 60° and 70° misorientation angles for CIGS thin-film solar cells, which correspond to near Σ3 boundaries for a tetragonal crystal structure. The most frequent grain boundary type in CdTe thin films is also 60° Σ3 (Figure 3.5b).

3.4 Grain boundary type and recombination activity

3.4.1 Grain boundary contrast analysis

Ideally, grain boundary contrast analysis must be performed on large grains with straight grain boundaries, as shown in Figure 3.6. This results in a 'clean' intensity profile, with a clear dip in intensity at the grain boundary plane and intensity plateaus within the neighbouring

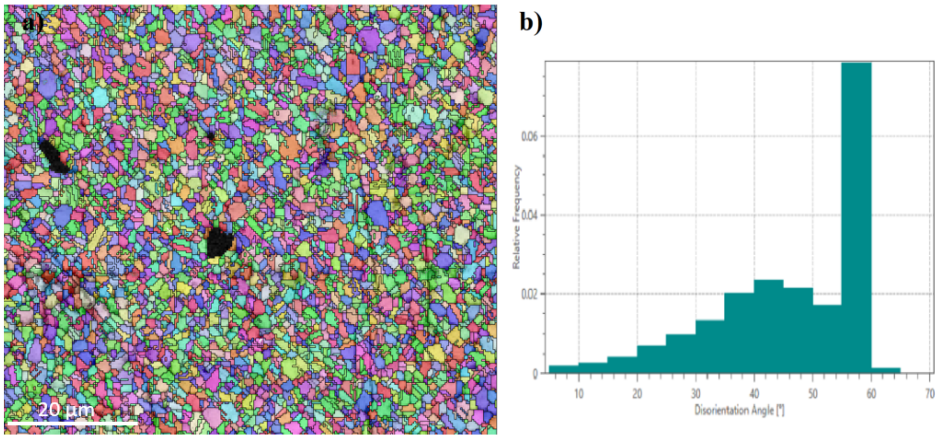

Figure 3.5: *(a) EBSD map of back contact surface in a CdTe-CdSe solar cell, (b) histogram showing the frequency (i.e. number fraction) of grain boundaries as a function of misorientation angle.*

grain interiors. Straight segments of grain boundary suggest that the grain boundary plane has little 'projected width' in the electron beam direction, so that the CL contrast is at its highest. On the other hand, curved grain boundary segments will have significant projected width, and therefore the contrast is lower than what it should be. Large grains are required to ensure that the intensity plateaus within the grain interiors. In contrast, small grains (Figure 3.7) have no flattened profiles because of the effect of the neighbouring grain boundary, which acts as a second source of non-radiative recombination and therefore decreases the CL intensity. Therefore, large grains with a straight grain boundary segment must be selected to ensure a clean profile. The cathodoluminescence contrast at each individual grain boundary (Figure 3.6) has been calculated from the intensity profile by using the formula:

$$\text{CL Contrast} = \frac{\text{Grain Interior Intensity} - \text{Grain Boundary Intensity}}{\text{Grain Interior Intensity}} \times 100\% \qquad (3.4.1)$$

The standard error for both grain interior (GI) and grain boundary (GB) intensity can be calculated by defining a window of some few pixels in width at the grain interior and grain boundary regions, as shown in Figure 3.8. The standard deviation related to the specific pixel values within each window can then be calculated, and the standard error determined using the following formula:

$$\text{Standard error of (GI,GB)} = \frac{\text{standard deviation of (GI, GB)}}{\sqrt{n}} \qquad (3.4.2)$$

where n is the number of pixels within a given window.

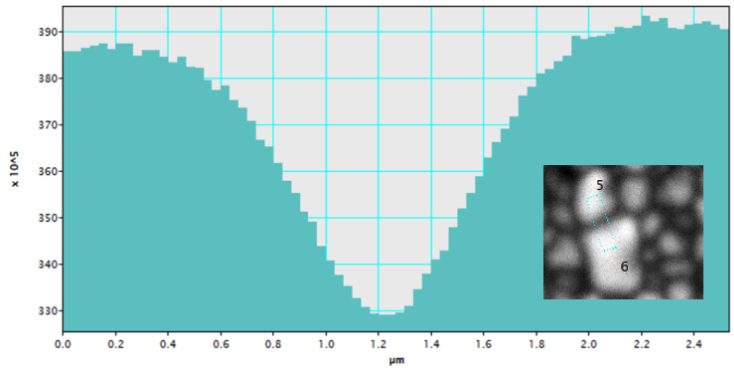

Figure 3.6: *The CL intensity profile between two large grains. The CL intensity is minimum at the grain boundary plane and plateaus to a maximum value at the grain interiors.*

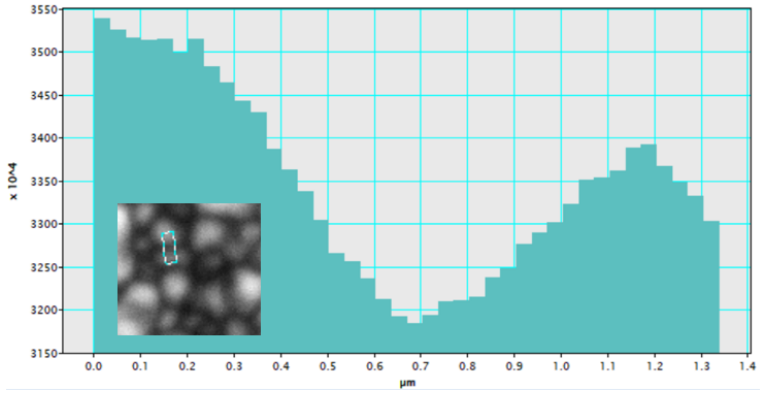

Figure 3.7: *The CL intensity profile between two small grains. The CL intensity is minimum at the grain boundary plane. The plateau regions are not well defined, due to the presence of neighbouring grain boundaries.*

The error for the numerator in the CL contrast (Equation 3.4.1) has been propagated by using the following formula:

$$\alpha_Z = \sqrt{(\alpha_A)^2 + (\alpha_B)^2} \tag{3.4.3}$$

where α_Z is the error of the numerator and α_A, α_B are standard errors of grain interior and grain boundary intensity respectively.

The error in CL contrast (Equation 3.4.1) is then given by:

$$\frac{\alpha_c}{C} = \sqrt{(\frac{\alpha_z}{Z})^2 + (\frac{\alpha_B}{B})^2} \tag{3.4.4}$$

where C is the CL contrast which has error α_C, α_Z is the error in the numerator (Equation 3.4.3) which has value Z, and α_B is the error in the denominator (Equation 3.4.2) which has value B. For a given grain boundary two values for the CL contrast can be defined

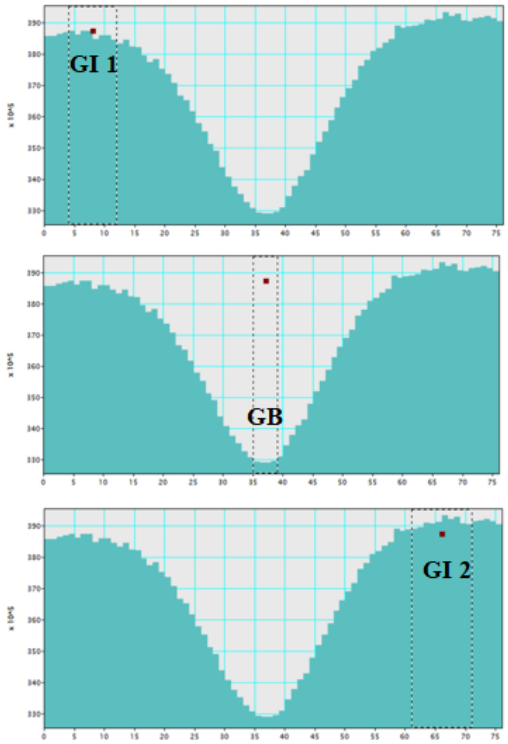

Figure 3.8: *The CL intensity window of GI 1, GB and GI 2 is used to calculate the error.*

according to Equation 3.4.1, since there are two values for the grain interior intensity from the neighbouring two grains. Therefore, the CL contrast values and errors reported here are the average of the two corresponding values.

3.4.2 Regular grain boundaries

Figure 3.9 shows CL and EBSD images acquired from the same area of the sample so that we are able to perform a correlative study on each individual grain and grain boundaries. The drawn circles showed the same porosity in the two images, which provides evidence that the sample area is the same. Note that there will be some slight differences in the appearance of the porosity, due to differences in the spatial resolution of CL and EBSD techniques, as well as the fact that the sample is steeply inclined at 70° for the latter (although a software correction is used to compensate for the resulting image distortion).

Approximately sixty four large grains have been picked to calculate the CL contrast and misorientation across their grain boundaries. For example, Figure 3.10 shows some selected grains. Moreover, Figure 3.11 shows EBSD pattern quality and orientation map. While the EBSD map provided the misorientation information, the pattern quality map is used to distinguish each grain and grain boundaries, especially for those CSL GBs. The CL contrast

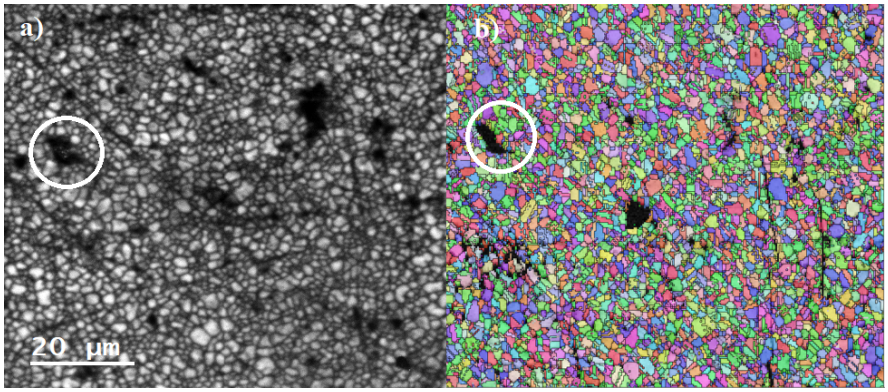

Figure 3.9: *(a) Panchromatic CL and (b) EBSD images of the back surface of a CdTe-CdSe solar cell. The circled region show sample porosity common to both images. The dark lines in the two images are due to surface scratches.*

information is then combined with the EBSD misorientation angle for each individual GB that is provided by Aztec crystal software, as displayed in Table 3.1.

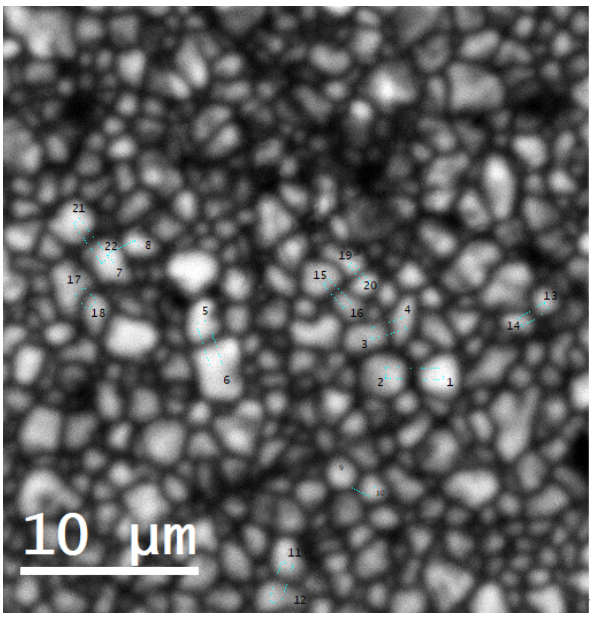

Figure 3.10: *CL panchromatic image that shows the grains chosen to calculate the grain boundary contrast between them. The small rectangular boxes indicate the regions from which CL intensity profiles were extracted.*

Figure 3.12 shows the plot of CL contrast versus the grain boundary misorientation angle from our results. It reveals high contrast values with large variations from approximately 11% to 26%, depending on the misorientation angle. Overall, the range 35°-55° includes high values of CL contrast, and around the angle 35° a high peak with maximum value in CL contrast is observed. The high CL contrast means high non-radiative recombination, which is harmful to the device.

Moseley *et al.* [60] has also reported a combined CL-EBSD analysis of grain boundaries and

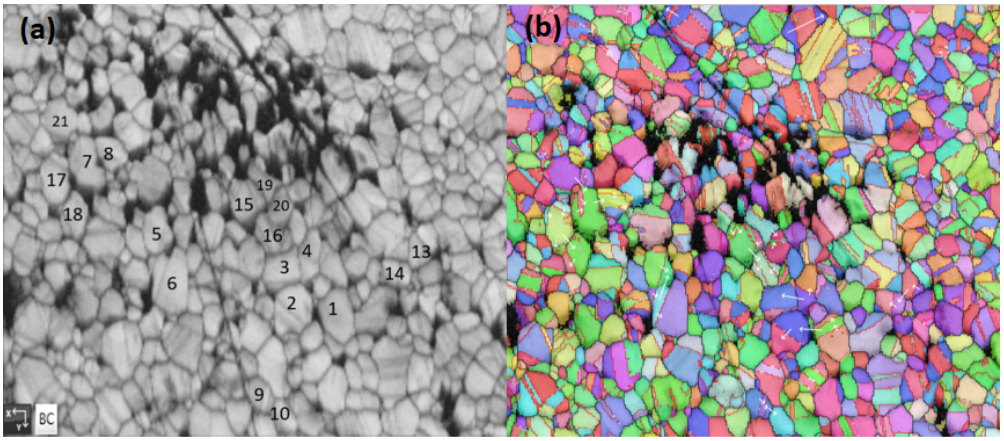

Figure 3.11: *(a) EBSD pattern quality map with the grains in Figure 3.10 chosen for grain boundary analysis. (b) corresponding EBSD orientation map of the same region. The red limes in (b) denote twin boundaries.*

how they impact the recombination rate in CdTe solar cell devices. The grain boundary recombination was examined before and after chlorine activation, by measuring the CL intensity at all GB types for both as-deposited and chlorine treated thin-films. A higher CL intensity means a low recombination rate. On the other hand, our results calculated and plotted the CL contrast, where high CL contrast denotes a high recombination rate. Moseley et al. found that the CL intensity for all GBs increased after $CdCl_2$ treatment including Σ 3, other CSL ($\Sigma = 5 - 49$) GBs and regular GBs, due to passivation of band gap defect states. (Figure 3.13). Generally, an increase in the average CL intensity with GB misorientation angle was observed for a given device condition (i.e. as-deposited or chlorine activated), as they found that small angles are more harmful for the device. This trend is unexpected, since from the dislocation model of grain boundaries (section 1.5.1) there should be less recombination for low angle ($<15°$ misorientation angle) than regular, high angle grain boundaries, due to a smaller dislocation density in the former. Moseley et al. assumed this might be because the deep levels were effectively passivated at the high angle GB. However, we note that the same trend is also observed for the as-deposited sample, where there is no chlorine passivation of the grain boundaries. Furthermore, we believe that a proper analysis requires a CL contrast calculation rather than the absolute CL intensity, since it is the decrease in the CL intensity at the grain boundary with respect to the grain interior (i.e. contrast) that is the true measure of GB recombination. Absolute CL intensity on the other hand will be susceptible to sample inhomogeneities, such as local variations in doping concentration, presence of porosity etc (discussed further below). A slight decrease in the average CL intensity for the chlorine activated sample was observed at the misorientation range 35-45° compared

Table 3.1: CL contrast values combined with EBSD misorientation for different grain boundaries.

GB Misorentation	CL Contrast(%)	GB Misorentation	CL Contrast(%)
18.6°	14.4	**43.4°**	14.8
22.3°	18.5	**44.4°**	19.0
23.6°	15.9	**45.1°**	12.1
25.4°	13.8	**46.9°**	21.0
25.8°	14.1	**49.3°**	18.7
29.5°	14.3	**49.6°**	19.6
30.9°	13.2	**50.9°**	13.2
32.3°	17.1	**51.4°**	19.1
34.3°	12.9	**52.3°**	14.5
35.3°	26.9	**52.7°**	15.5
35.6°	24.2	**53.9°**	17.1
39.5°	17.5	**54.2°**	18.9
39.6°	11.7	**56.3°**	13.8
41.1°	20.6	**57.1°**	10.8
41.3°	15.4	**57.1°**	13.9
43.1°	15.7	**58.9°**	14.9

to 25-35° and 45-55° ranges (Figure 3.13). Our results however showed an increase in the CL contrast around this range, especially at 41° and the highest CL contrast at 35°, which is inconsistent with the results of Moseley et al.

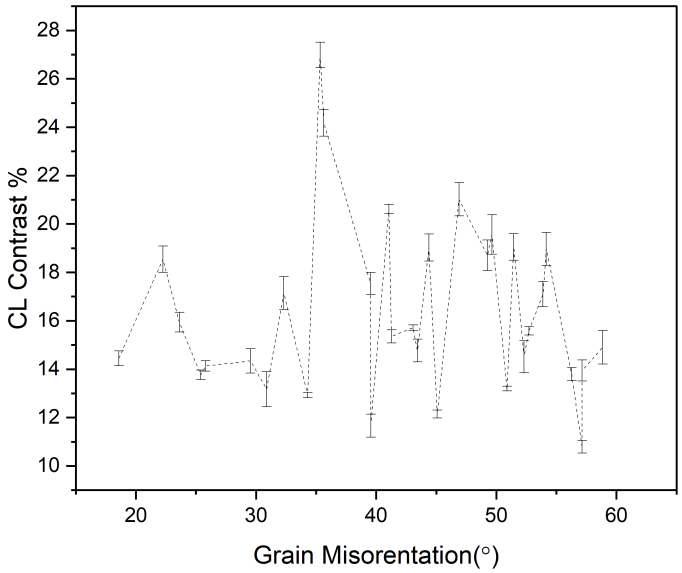

Figure 3.12: *The CL contrast as a function of grain boundary misorientation. The line connecting the data points is a guide to the eye only.*

A close investigation of the grain boundary between grains 1 and 2 in Figure 3.14a, which has a misorientation angle 41.1°, showed that the CL contrast at this misorientation has a high value of 20.6 %. It would appear as though this particular misorientation is harmful to the device, but at a similar misorientation of 41.3° for another GB, the CL contrast drops to 15.3% (Figure 3.12). This difference in CL contrast might not be related to the misorientation angle, but rather to artefacts in the specimen microstructure. For example, in the EBSD image of Figure 3.14b a smaller grain and a pore between grains 1 and 2 are observed. These features are however not seen in the panchromatic CL image. The extra grain boundary area due to the smaller grain, as well as the free surface of the pore, will give rise to additional non-radiative recombination, which could explain the higher CL contrast. This example highlights some of the artefacts in our analysis, and why Figure 3.12 may not be truly representative of the true effect of grain boundary misorientation on carrier recombination. Nevertheless, some general trends can still be extracted, as also observed in Figure 3.14. The dark GB in Figure 3.14a indicates strong non-radiative recombination. However, the special twin grains (CSL $\Sigma 3$), which appeared as red lines within grain 1 (Figure 3.14b), did not show any significant non-radiative recombination in the CL image compared with other regular grain boundaries.

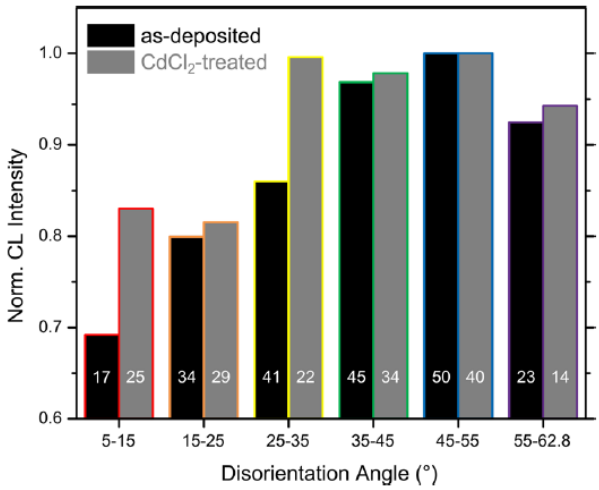

Figure 3.13: *The average CL intensity of GBs as a function of the GB disorientation angle for the as-deposited and $CdCl_2$-treated films. The highest intensity is normalised to one. [60]*

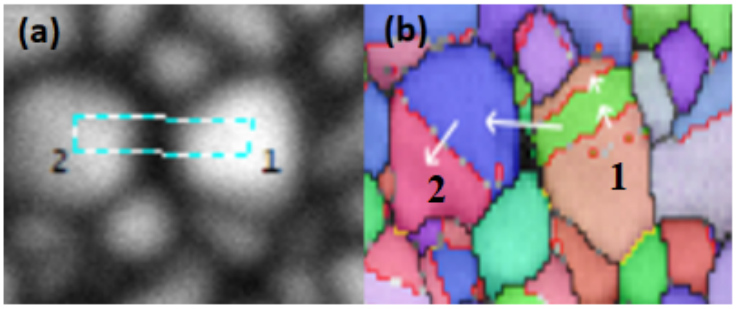

Figure 3.14: *(a) CL panchromatic image showing strong CL contrast at the boundary between grain 1 and 2. (b) EBSD orientation map of the same region. The white arrows indicate different grain interior regions separated by a twin boundary (red lines).*

3.4.3 Coincident site lattice grain boundaries

Using the CL and EBSD data for the same region, CSL grain boundaries have also been investigated. This includes the Σ3 twin boundary, which has a misorientation angle equal to 60° and appears more frequently in the sample. It has been observed that Σ3 CSL have small CL contrast values compared to the regular GBs. The CL contrast varied from 0.2% to 10%, as shown in Figure 3.15, where it appeared that the CL contrast for these types of GBs is smaller than the average contrast of the regular GBs. This is clear from the twin boundaries within grains 1 or 2, i.e. the red twin boundary in the EBSD map. The CL map did not show visible non-radiative recombination, indicating only a small amount of non-radiative recombination. This is not the case for the general GB between grains 1 and 2, which has strong non-radiative recombination (wider darker grain boundary). Similar observations can be made for grains 5 and 6. Therefore, Σ3 GBs are not working as centres for harmful

non-radiative recombination in the device, despite the fact that for CdTe the para-variant of the twin boundary can potentially act as a strong recombination centre due to wrong bonds (section 1.5.3). The EBSD analysis in this work cannot distinguish between ortho and para-twin variants, and therefore no comment can be made about which type is present in our samples. Nevertheless, our results are in good agreement with Moseley *et al.* [60], as they mentioned that only a small percentage (16-18%) of Σ3 twin boundaries are active as non-radiative recombination centres, i.e. they have high recombination velocity.

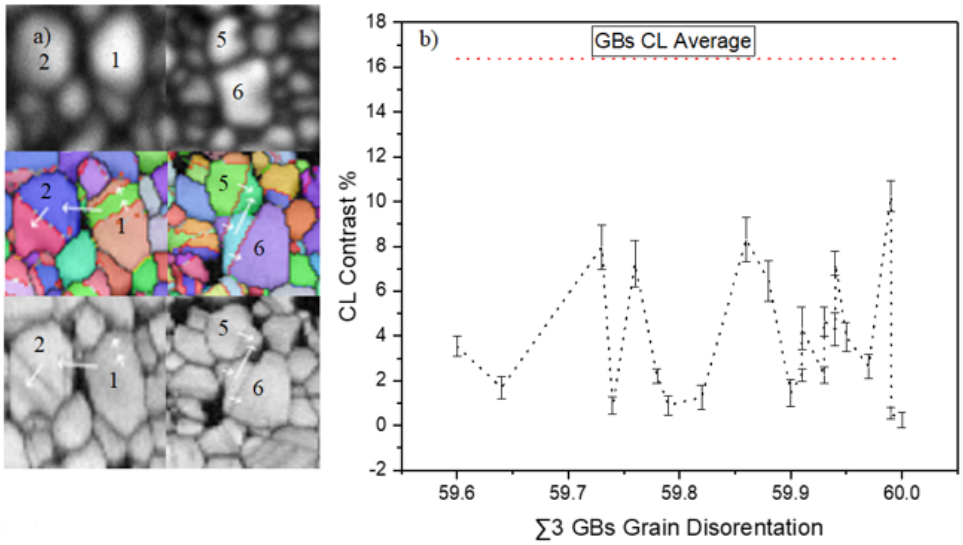

Figure 3.15: *a) CL panchromatic (top), EBSD orientation (middle) and pattern quality (bottom) maps showing some* Σ3 *GBs within the grains labelled '1' and '2' as well as '5' and '6'. b) CL contrast as a function of GB misorientations close to* Σ3 *CSL. The line connecting the data points is a guide to the eye only. The horizontal dashed line represents the average CL contrast for the regular grain boundaries in Figure 3.12.*

Moreover, other CSL such as Σ5, Σ7, and Σ9 GBs have also been investigated. Figure 3.16 shows that they also have low CL contrast compared to general GBs, although they were relatively rare in the sample. The low recombination activity of CSL grain boundaries compared to regular grain boundaries is consistent with the fact that the former has higher symmetry, and therefore fewer dangling bonds that would lead to fast non-radiative recombination.

Moseley *et al.* [60] also found Σ3 CSL GBs showed a high CL intensity consistent with our low CL contrast values (Figure 3.17) indicating they are not harmful to the device. However, other-CSL (Σ=5-49) GBs show no significant difference from the regular GBs, while our results show small values of contrast for other CSL ($\Sigma 5, \Sigma 7, \Sigma 9$) (Figure 3.16). The small Σ values of our investigation might be the reason why the GB recombination is lower compared to the larger Σ values in Moseley's study.

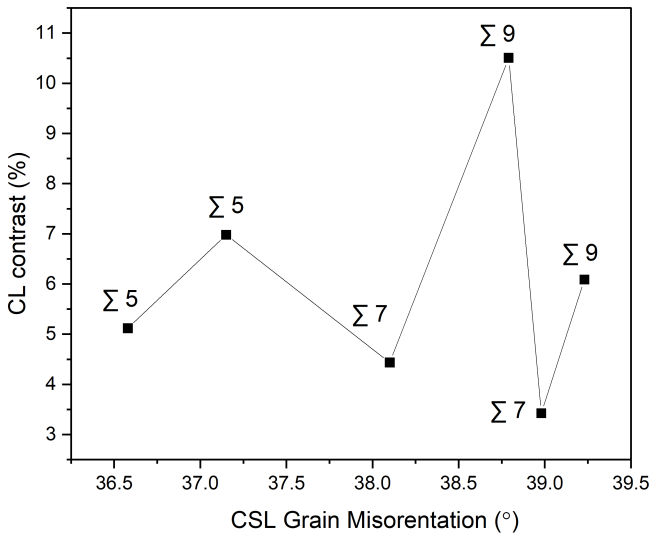

Figure 3.16: *The CL contrast as a function of misorientation angle for* $\Sigma 5$*,* $\Sigma 7$ *and* $\Sigma 9$ *CSL GBs. The line connecting the data points is a guide to the eye only.*

3.5 Reduced recombination velocity of grain boundaries

This section will further quantify how an individual grain boundary affects photovoltaic performance by studying the relationship between recombination velocity and grain boundary type. Recombination velocity is the rate at which carriers diffuse to the grain boundary to replenish the carriers lost to recombination, thereby maintaining a steady-state carrier concentration. A grain boundary with a high recombination velocity is electrically more active and has a more negative impact on the device efficiency. Mendis *et al.* [113] measured the reduced recombination velocity of a single grain boundary by combining the CL technique with the high spatial resolution of a SEM. They showed that the CL intensity contrast $\Delta I(X)$ at a distance (X) from the grain boundary is given by the equation:

$$\ln[\Delta I(X)] = \ln(\frac{S}{S+1}) - \frac{X}{L} \tag{3.5.1}$$

where S is the reduced recombination velocity and L is the minority carrier diffusion length. The reduced recombination velocity is the recombination velocity divided by the bulk carrier diffusion velocity. By least squares fitting a straight line to the $\ln[\Delta I(X)]$ vs. X data points, L and S can be extracted from the gradient and intercept respectively.

The reduced recombination velocity at the GB and diffusion length have been calculated from the CL intensity profile according to Equation 3.5.1. Figure 3.18 shows the GB between two

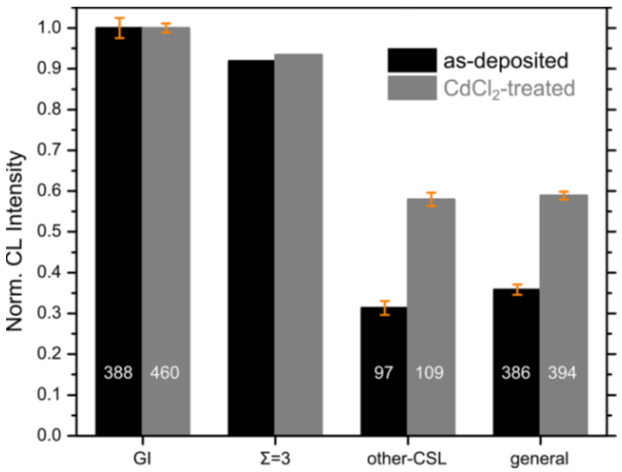

Figure 3.17: *Bar chart showing the average CL intensity calculated for each GB type (Σ3, other-CSL (Σ = 5 − 49) and regular GBs) relative to the average grain interior (GI) CL intensity for the as-deposited and $CdCl_2$ treated films. The numbers at the bottom of the bars indicate the number of GBs sampled of each type. The highest intensity in the scale is normalised to one. [60]*

Table 3.2: The calculated diffusion length (L), reduced recombination velocity (S), CL contrast and grain misorientation values that are related to grain boundaries 1,2 and 3,4 (Figure 3.18).

GB	Diffusion length(L)	Reduced velocity(S)	Misorentation	CL Contrast
1,2	0.42±0.07	0.52±0.16	41.1°	20.62
3,4	0.36±0.02	0.19±0.01	34.3°	12.93

grains labelled 1 and 2, with a relatively large value (0.52) of reduced recombination velocity (Table 3.2). The CL contrast for this GB was 20%, which confirms the strong non-radiative recombination. The related misorientation at this GB was 41° as measured using EBSD (Table 3.2). For the second GB between two different grains labelled 3 and 4, the reduced recombination velocity (0.19) was smaller than the previous GB, and the CL contrast (12.9%) and misorientation (34°) at the GB is lower than the previous one. It is clear that the non-radiative recombination is not as strong as the previous GB between grains 1 and 2. This indicates that the CL contrast analysis presented in Section 3.4 is a good indicator of the role of grain boundary misorientation on recombination activity. The benefit of CL contrast however is that a large number of grains can be rapidly analysed compared to calculating the reduced recombination velocity. The larger number of grains gives a statistically more valid picture of grain boundaries in the absorber layer. Finally, for both sets of grains in Figure 3.18 the minority carrier diffusion length was estimated to be 0.4 μm. This is a similar value to that reported in [113].

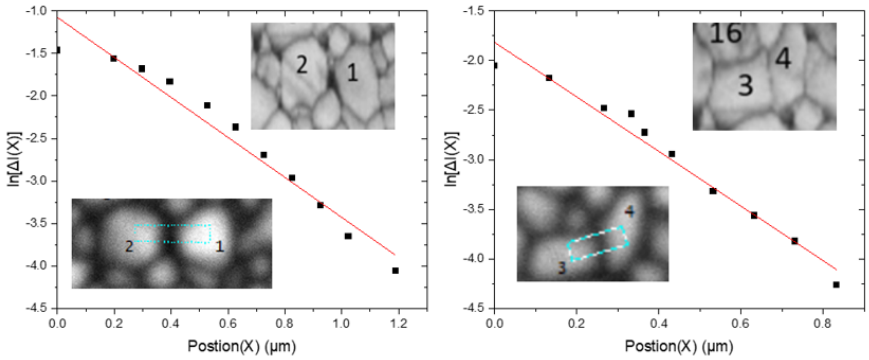

Figure 3.18: *Reduced recombination velocity analysis across two grain boundaries. The upper inset is an EBSD pattern quality map indicating the grains that have been analysed. The lower inset is the corresponding panchromatic CL image from which data analysis is performed.*

3.6 Conclusion

In conclusion, CL and EBSD correlative investigations of regular and CSL grain boundaries in CdTe-CdSe thin-film have been presented in this chapter. The grain boundaries were assumed to be pure CdTe, since EDX results showed there is no selenium appearing at the back contact surface. CL contrast has been calculated, and for the regular GBs, the contrast was significantly high in the range between 35°-55° misorientation angle. This means that those regular grain boundaries are strong non-radiative recombination centres. The highest CL contrast was observed at 35°, which might indicate this particular misorientation angle has the highest harmful effect on the device. On the other hand low index CSL such as $\Sigma 3$, $\Sigma 5$, $\Sigma 7$ and $\Sigma 9$ showed much lower contrast values which is consistent with the fact that they have high symmetry. The robustness of our results was examined by performing more detailed quantitative analysis of the reduced recombination velocity. The reduced recombination velocity results were consistent with the previous trends, i.e. the high contrast grain boundary has a larger reduced recombination velocity than the lower contrast grain boundary. Our results for the regular grain boundaries had the opposite behaviour to that reported in Moseley *et al* [60] and this might be due to the contrast calculation being the more proper analysis rather than the absolute CL intensity used in Moseley *et al.* In particular, the normalised average CL intensity was slightly lower around the range 35°-45°, while our results showed a high CL contrast in the same misorientation range. Furthermore, Moseley *et al* [60] observed $\Sigma 3$ CSL had a high intensity which is in agreement with our low contrast values, indicating that the non-radiative recombination is small at $\Sigma 3$ CSL. However, there was no agreement for other CSLs, with our study reporting low recombination for $\Sigma = 5$, 7 and 9 GBs and Moseley *et al* [60] reporting recombination rates that were similar to regular GBs.

The discrepancy could however be due to the much larger Σ range in Moseley's study (i.e. $\Sigma = 5 - 49$).

Chapter 4

Investigating Se diffusion in CdSe-CdTe solar cells using CL and TEM

4.1 Motivation

In the previous chapter, the analysis was done on the back contact surface of the CdSe-CdTe thin film, where the EDX results showed it to be a pure CdTe thin-film. This chapter is concerned with investigating Se diffusion from CdSe to CdTe by using a bevel cross-section to understand how Se diffusion affects the microstructure. Two samples with different thicknesses of CdSe layer motivated us to investigate the reason why the sample with 400 nm thickness showed a large decrease in efficiency compared to a 100 nm sample. It has been known that using CdSe as a n-type buffer layer improves the device efficiency by narrowing the band gap and collecting more current. The advantage of alloying CdTe solar cell absorbers with selenium is to decrease the material bandgap and therefore increase absorption of the long-wavelength range of the solar spectrum. The increase in efficiency of CdSeTe solar cells is a result of higher short circuit current density J_{sc}, where the quantum collection efficiency for short and long wavelengths will increase leading to larger J_{sc} values as mentioned previously in section (1.7). The CdSeTe layer (which is formed during the growth of CdTe) has the ability to convert incident photons to electric current and this depends on the Se concentration and crystal structure. It has been observed that at higher Se concentrations (>60 %), the crystal structure transforms from cubic zinc blende to hexagonal wurtzite, which is found to be photo-inactive [54].

The initial aim of the investigation was to examine if a change in crystal structure could explain the dramatic drop in efficiency for the 400 nm CdSe device. Our investigations using cathodoluminescence (CL) and transmission electron microscopy (TEM) however uncovered an alternative mechanism, where the rapid diffusion of Se along the CdTe grain boundaries led to solute pinning and small absorber layer grains close to the pn-junction. Kirkendall voiding at the grain boundaries was also observed. Together these two effects explain the efficiency drop in these devices. The chapter is organised as follows. Device properties of the samples are described in section (4.2). The explanation of the experimental methodology used to prepare the bevel cross-section for CL and TEM samples is presented in section (4.3). Then the standard and bevel cross-section CL results are presented in section (4.4). Finally the results of transmission electron microscopy and the solute drag effect by moving grain boundary discussed in sections (4.5) and (4.6).

4.2 Device properties of samples

The CdSe-CdTe samples used in this research were fabricated and deposited by Drs Jacob Leaver and Jon Major at the University of Liverpool. Two sample sets were provided, labelled set A and set B respectively. The external quantum efficiency (EQE) of Set A samples is shown in Figure 4.1, with constant 100 nm CdSe thickness but with variation in CdTe deposition pressure and the application of a chlorine activation step. Chlorine activation was performed in air at 430°C for 30 minutes, using $MgCl_2$ as the source of chlorine (1 mol/dm^3 aqueous solution of $MgCl_2$ was spray-coated onto the back surface of the devices). A "pre-heat" stage before CdTe deposition (via close space sublimation; CSS), with a source temperature of 600°C for 20 minutes at 400 Torr was applied for all the samples. The source temperature used was 600°C, and the substrate temperature was around 550°C.

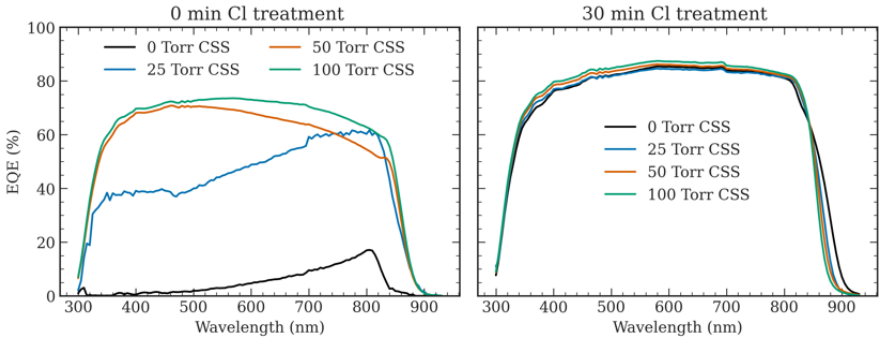

Figure 4.1: *External quantum efficiency (EQE) of set A samples (100 nm CdSe thickness, variable CdTe deposition pressure) with and without Cl treatment.*

Cl treatment appeared to improve the overall efficiency, especially for those samples deposited at low pressure (0-25) Torr, as the EQE showed the range of strongly absorbed wavelength improved after 30 min of Cl treatment. This is because the grain boundaries were passivated after the chlorine treatment, as discussed previously in section 1.6 [52], [82]. For the non-chloride activation device, the EQE for 50-100 Torr CSS showed that the device absorbed the light from 900 nm to 300 nm. The wavelength larger than 900 nm is not able to be absorbed by the device because the photon energy is smaller than the band gap, resulting in zero EQE. A plateau external quantum efficiency appeared between 400-850 nm, indicating maximum photo-current generation by the absorber layer. The EQE then dropped suddenly around 300 nm due to parasitic absorption by the fluorine doped tin oxide (FTO) layer which has a 3.6-3.8 eV band gap [114]. The EQE for 0 and 25 Torr devices without Cl activation appeared much lower compared to 50-100 Torr CSS. This is likely due to the small grains formed at low pressure 0-25 Torr CSS, which contains a high density of grain boundaries and defects.

Major *et al.* [115] measured the performance parameters as a function of grain size by varying the CSS pressure, and they found that the grain size increased with higher pressure. The increase in grain size reduced the harmful impact of grain boundaries. The SEM images in Figure 4.2a show how the grain size increased with increasing the pressure from 2 to 200 Torr CSS. The average device performance parameters from J-V curves measured as a function of deposition pressure in Figure 4.2b showed that all the parameters improved with the large grain size.

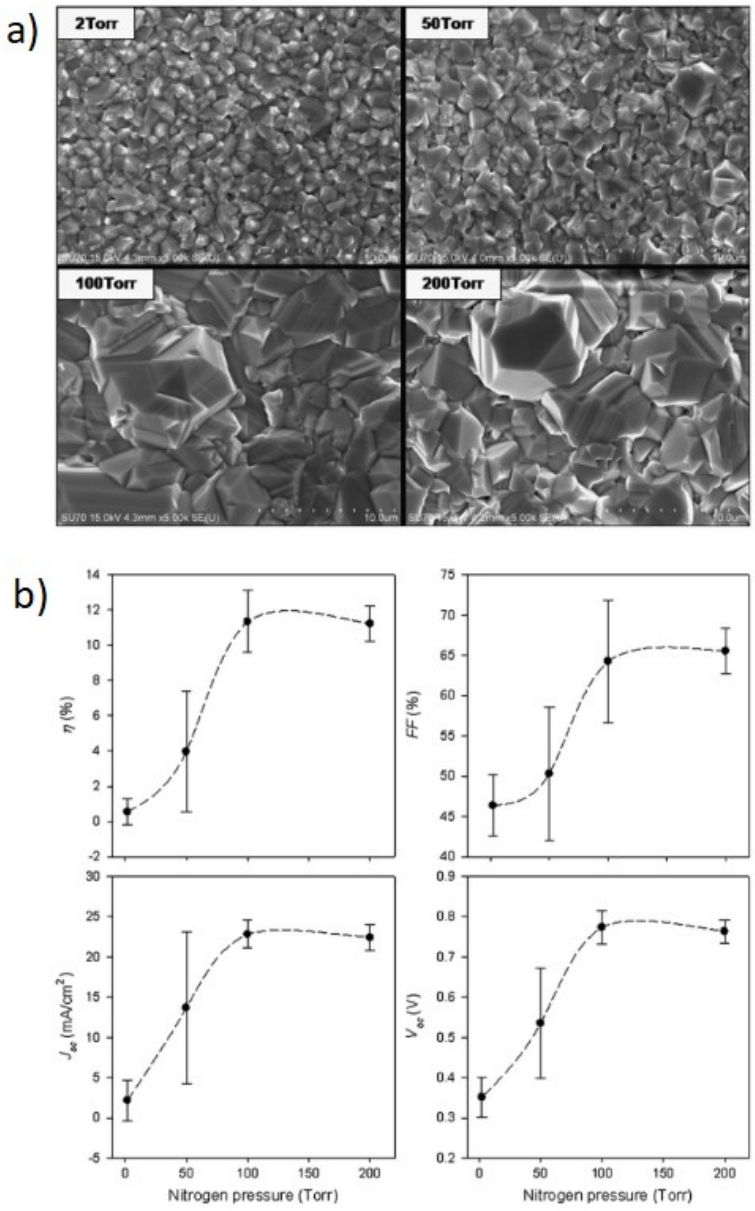

Figure 4.2: *(a) SEM images of CdTe deposited by CSS under different pressures 2-200 Torr. (b) Average device performance parameters extracted from J–V curves as a function of the pressure present during deposition. [115]*

The performance parameters including efficiency, open circuit voltage (V_{oc}), short circuit

current density (J_{sc}), and fill factor (FF) are shown in Figure 4.3. Each data point represents the measurement for one device, and in some cases a large scatter appeared between individual devices. The short circuit current density, which is related to the external quantum efficiency, increased after Cl activation for all samples, consistent with Figure 4.1. The increase in J_{sc} is the biggest contributor to the higher device efficiency following Cl activation. The spread in V_{oc} and fill factor was too large to detect any meaningful change between devices.

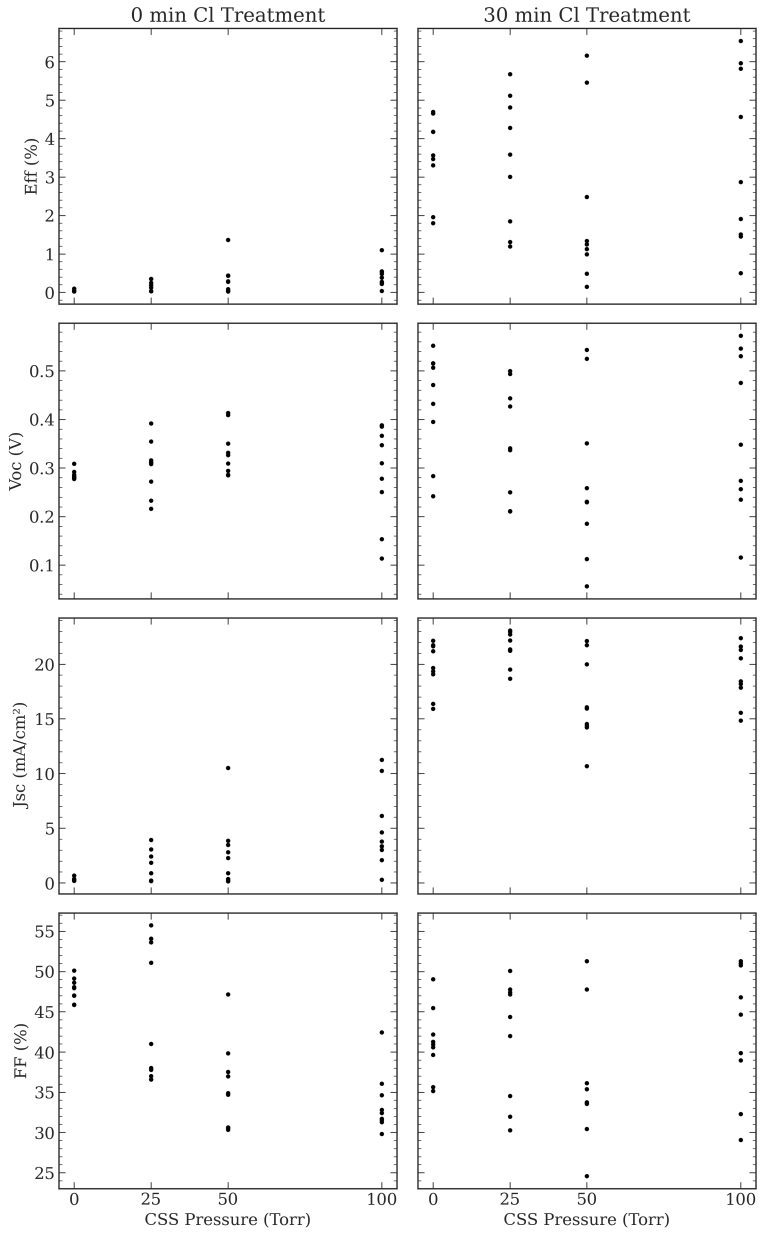

Figure 4.3: *Device performance parameters of set A samples with and without Cl treatment.*

Samples of set B have a constant CdTe deposition pressure (5 Torr) and 60 minute chloride treatment but with a variation of underlying CdSe thickness, i.e. 50-100-200-400 nm. The EQE for the thicker layers in Figure 4.4 showed a lower bandgap as evidenced by the onset of

absorption at a longer wavelength range, implying higher Se incorporation in the CdTe due to inter-diffusion. The EQE in the wavelength range 400-800 nm decreases gradually with CdSe layer thickness, until at 400 nm CdSe thickness, a dramatic drop in EQE is observed. This is also reflected in the device performance parameters (Figure 4.5), where the lower EQE for the 400 nm layer results in a lower J_{sc}, and average device efficiency as well. Previous literature reported that the reason behind this drop in EQE at 400 nm (Section 1.7- Figure 1.21) is due to the photo-inactive wurtzite phase, which decreased the short circuit current and consequently efficiency [54].

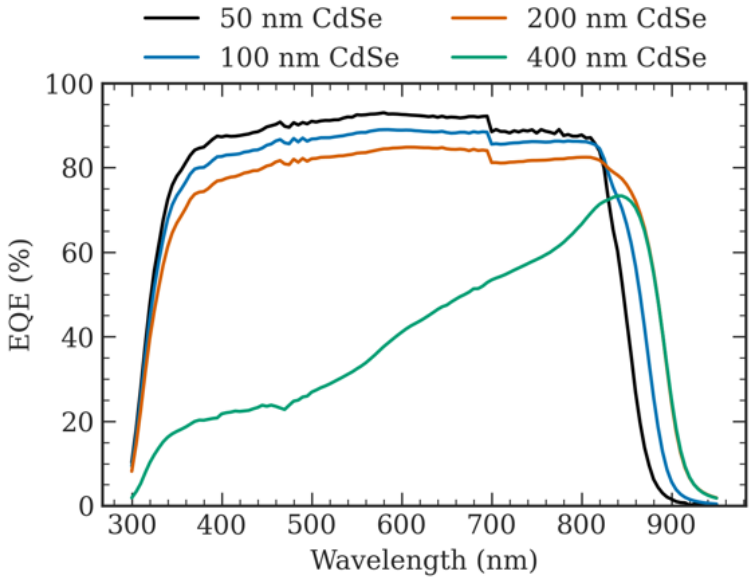

Figure 4.4: *EQE measurements of set B samples with Cl treatment.*

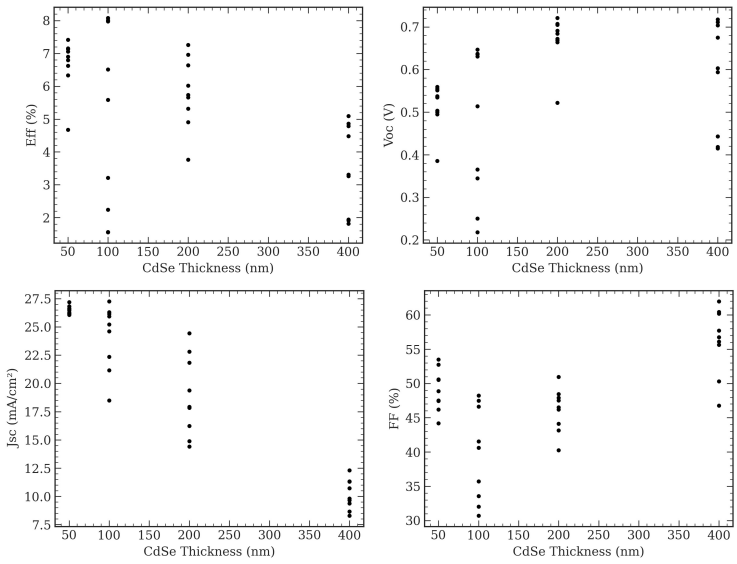

Figure 4.5: *Device performance parameters of set B samples.*

4.3 Experimental methodology

4.3.1 SEM-FIB Standard and Bevel Cross section

The geometry of FEI Helios Nanolab 600 dual-column FIB SEM microscope (Figure 4.6a) which is used to produce both standard and bevel cross-section, contains a Ga ion beam tilted by 38° to the sample surface. The standard cross-section is achieved when the ion beam is perpendicular to the sample surface (i.e. platinum deposition, milling and cleaning cross-section operations performed at 90° angle), which means the sample must be tilted to 52° as shown in Figure 4.7a. The bevel cross-section is formed by cutting the thin-film at an angle other than 90°, in order to get the sloped surface at a shallow angle. The bevel angle refers to the angle between the milling ion beam and the sample surface plane as shown in Figure 4.7b and 4.8. The advantage of using a bevel cross-section with a shallow bevel angle is to elongate the cross-section surface, which will make it easier to investigate the thin-film layers and Se diffusion profile without any limitations in spatial resolution.

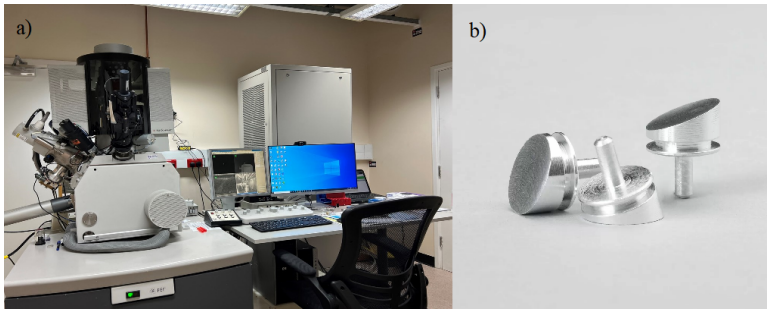

Figure 4.6: *a) FEI Helios Nanolab 600 dual-column FIB SEM microscope in Durham University. b) 20° SEM Specimen Stub .*

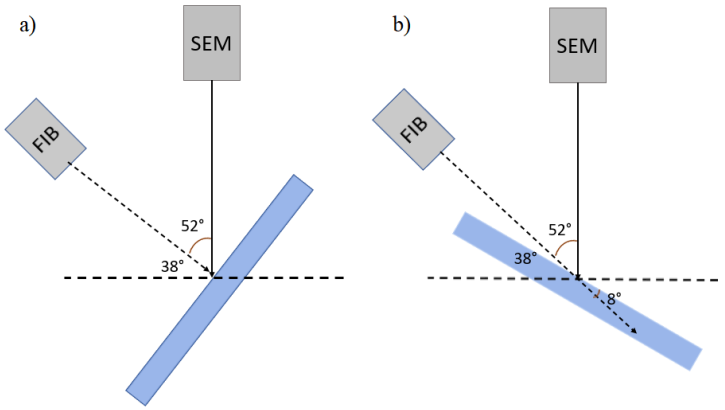

Figure 4.7: *a) geometry for preparing a standard cross-section b) the bevel cross-section at 8° angle.*

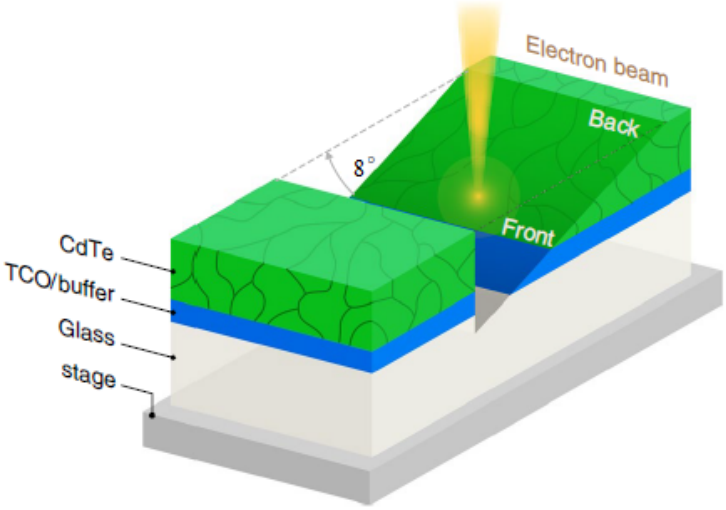

Figure 4.8: *Schematic diagram showing the bevelled cross-section at 8°, TCO and buffer layer represent FTO/SnO_2 and CdSe respectively. [116]*

The sample stage of the FEI microscope can tilt to a maximum -10° away from the ion beam. For a sample tilted to this angle, it is not possible to get a bevel cross-section with an angle lower than 28°(= 38°- 10°). Figure 4.9 shows a bevel cross-section at 28° for the sample with 400 nm of CdSe thickness.

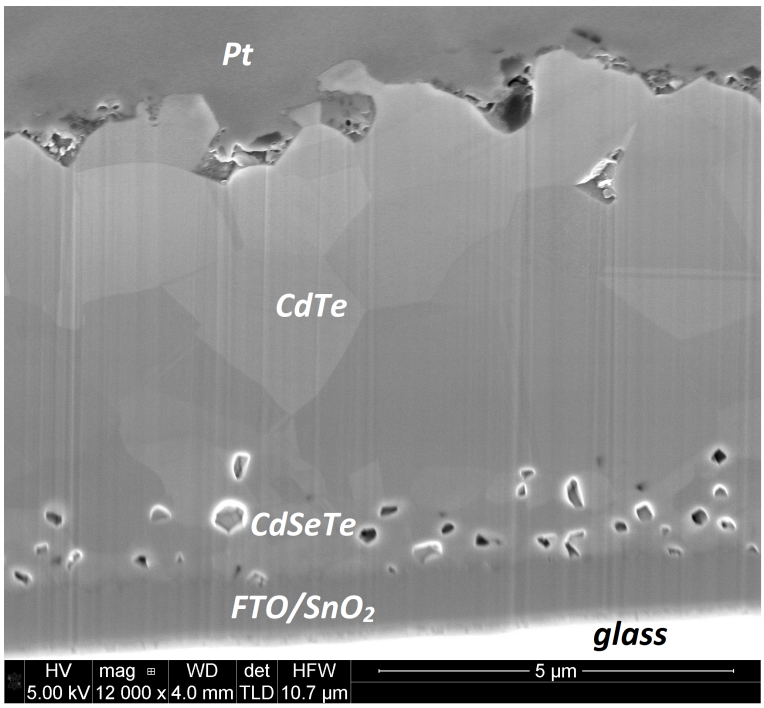

Figure 4.9: *Set B 400 nm bevelled cross-section with bevel angle 28°.*

A 12.5 mm SEM specimen stub inclined at 20° angle (Figure 4.6b) has been used for the purpose of producing a shallower bevel cross-section, where the ion beam makes 18° angle

with the specimen stub. When the sample is tilted to -10°, a bevel cross-section with 8° (= 18°- 10°) angle can be achieved, as shown in Figure 4.7b. Detailed steps to prepare the bevel at this angle is as follows: after mounting the sample on the stub, it was tilted to a 32° angle facing the ion beam to deposit a protective platinum strip at 30 kV and 0.9 nA of current with dimensions X= 60 µm, Y= 10 µm and Z= 5 µm. The purpose of depositing platinum is to avoid the so-called 'curtaining effect' that occurs during the milling process. Curtaining is caused by a non-uniform sputter rate and appears as 'scratches' along the length of the cross-section. After Pt deposition the sample is tilted to -10° away from the ion beam in order to do the regular cross-section milling at 30 kV with an increased current of 6.5 nA, followed by cleaning cross-section at the same voltage but lower current 2.7 nA. Finally, a gentle cleaning cross-section at a low voltage of 5 kV and a low current of 1.3 nA is used to clean the bevel.

4.3.2 FIB TEM sample preparation

It was mentioned previously that the focused ion beam can be used to prepare TEM samples (Section 2.5). A FEI Helios Nanolab 600 dual-column FIB SEM microscope was used in this work to prepare FIB TEM samples. Samples were prepared by Dr B.G. Mendis, Durham University. The same 2 x 1 mm sample geometry used for correlative CL and EBSD analysis (Chapter 3) was used for preparing a TEM cross-section. FIB electron column imaging is used to identify the area of interest. The sample was first tilted to 52°, where the ion beam was perpendicular to the sample surface. This is used for depositing a thin layer of platinum on the surface, which helps to reduce ion beam damage during the milling and thinning of the sample. The ion beam operational settings for depositing platinum are 8 kV and 0.66 nA. A platinum rectangle was deposited with dimensions: X = 15 µm, Y = 2 µm, and Z = 4 µm. Next the regular cross-section feature is used to mill trenches on either side of the deposited platinum at a higher ion-beam voltage of 30 kV, 6.5 nA current with dimensions: X = 20 µm, Y =10 µm, and Z = 5 µm (Figure 4.10). A cleaning cross section (polishing process) was also used to get a clean cut of the sample with lower (1.4 nA) current.

In order to undercut the sample for extraction, the sample was tilted back to 0°. Parallel milling of three separate rectangles was performed in a U-shaped design (Figure 4.11a), with one of the vertical rectangles (the right hand side in Figure 4.11a) intentionally shorter, in order to keep the sample attached to the surrounding material. This milling process is done on both sides by rotating the sample 180°. The new TEM sample is extracted out of the

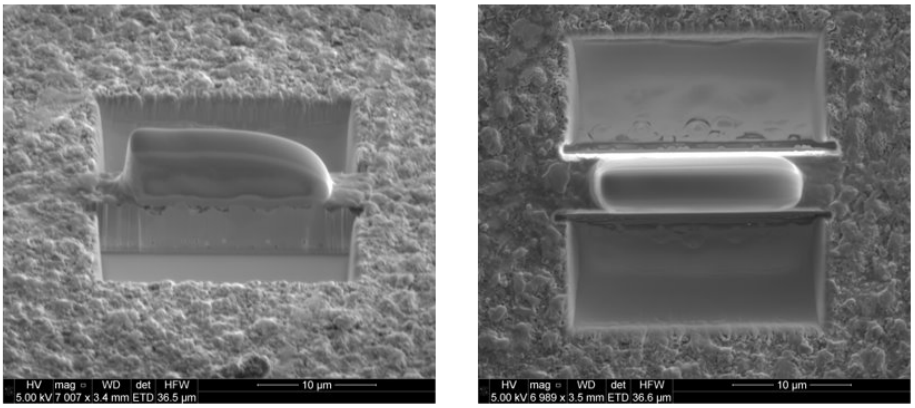

Figure 4.10: *SEM image showing (a) Regular cross section milling of the trenches. (b) the regular cross-section milling from a plane view showing the platinum strip and the two trenches.*

specimen using a tungsten needle. Here the sample is attached carefully to the tungsten needle by using platinum deposition (Figure 4.11b). The remaining attached part of the sample with the surrounding material is cut so that it can be released from the rest of the sample (Figure 4.11c). Then it is lifted together with the needle as shown in Figure 4.11d. The platinum deposition is used again to attach the sample to a TEM grid, and the previous platinum attaching it to the needle is cut so that the sample and the needle are separate (Figure 4.12).

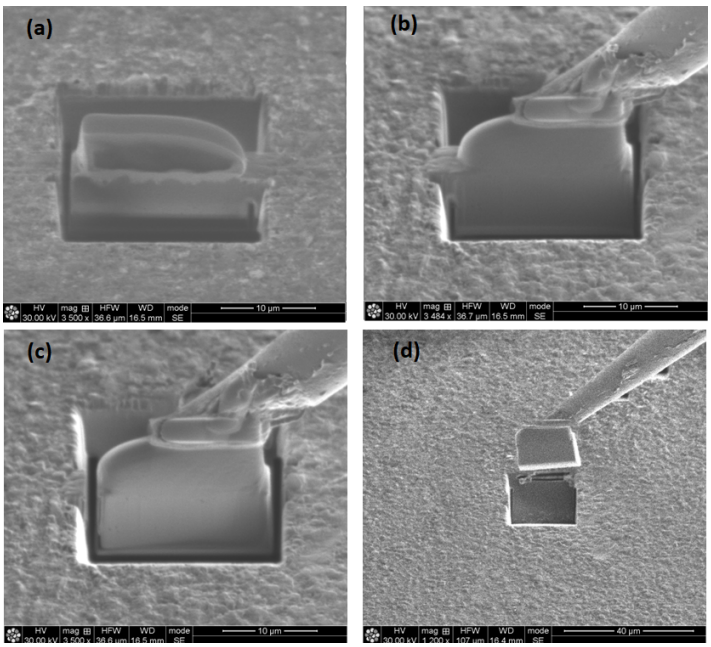

Figure 4.11: *(a) U-shape of the three rectangle milling pattern. (b) Attaching the sample to the tungsten needle by using platinum deposition. (c) releasing the sample by cutting the remaining attached part of the sample to the rest of the material. (d) The sample is raised outside the trench together with the needle.*

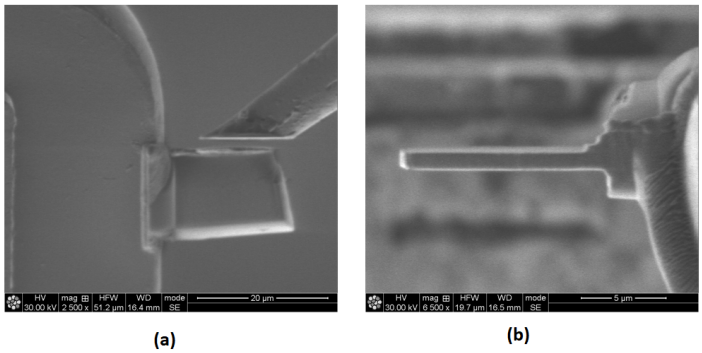

Figure 4.12: *SEM image showing (a) The sample after attaching to the TEM grid by using platinum depostion. (b) Sample thickness at an intermediate stage during the thining process.*

The sample was tilted to 54° and 30 and 16 kV ion-beam voltage was initially used to thin the sample on both sides by rotating the sample by 180°. Then the ion beam voltage was reduced to 8 and 5 kV to thin the sample further. At this step, care is required when thinning through the material and polishing the specimen so that the area of interest remains intact. Finally, we end up with a cross-section thin sample (100-150 nm thickness) where the electrons can penetrate through it easily as shown in Figure 4.13.

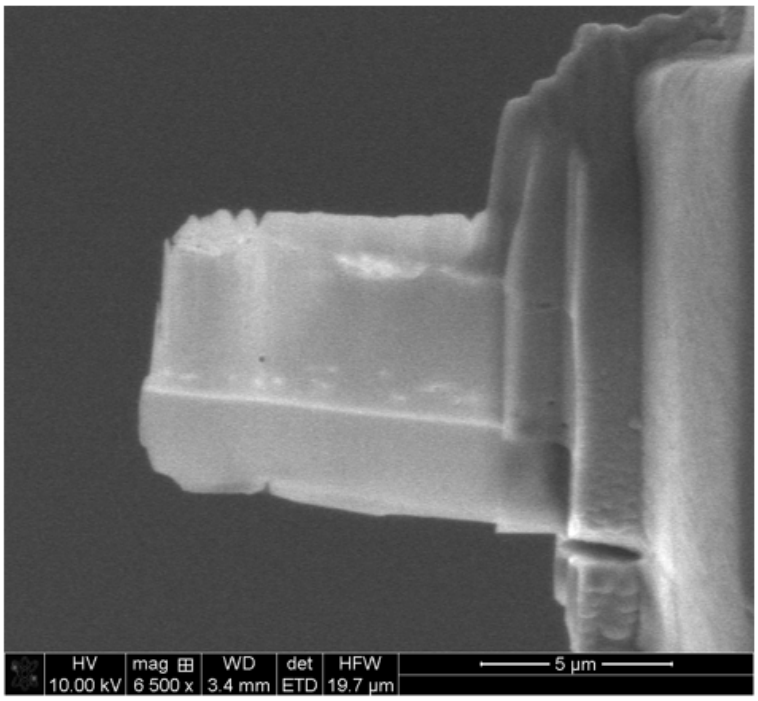

Figure 4.13: *SEM image showing the completed sample after the thining process.*

4.4 Standard and bevel cross-section CL results

In the previous chapter 3 set A sample was used with 0 Torr CSS. This chapter focuses on samples of set B, with 100 and 400 nm thickness of CdSe to understand more about the decrease in EQE for the latter, which leads to overall poor efficiency. The following sections will investigate CdSe-CdTe solar cells in regard to the microstructural and optoelectronic changes as well as Se diffusion from CdSe to CdTe. Electron microscopy was used to examine the solar cell microstructure at high spatial resolution. Cathodoluminescence (CL) technique is used to image the structure across the prepared bevel cross-section, and electron backscatter diffraction (EBSD) helped identify the phases formed during the inter-diffusion.

4.4.1 Sample with 100 nm CdSe

Figure 4.14 shows the standard cross-section for the sample with 100 nm of CdSe layer. It is difficult to visually identify a 100 nm CdSe layer, even at high magnification (Figure 4.14b). It might be because some of the CdSe layer dissolves into the CdTe. Some voids were observed close to the FTO layer, which might be experimental proof for the diffusion of Se from the CdSe layer to the CdTe layer. These voids are called Kirkendall voids or Kirkendall porosity. The Kirkendall porosity occurs due to the difference in the diffusion rate between the two materials, which results in a net diffusion of vacancies. When there are two different materials, such as CdSe and CdTe in our case, they will diffuse into each other at high temperatures at different rates, creating voids in the material with the larger diffusion flux [117].

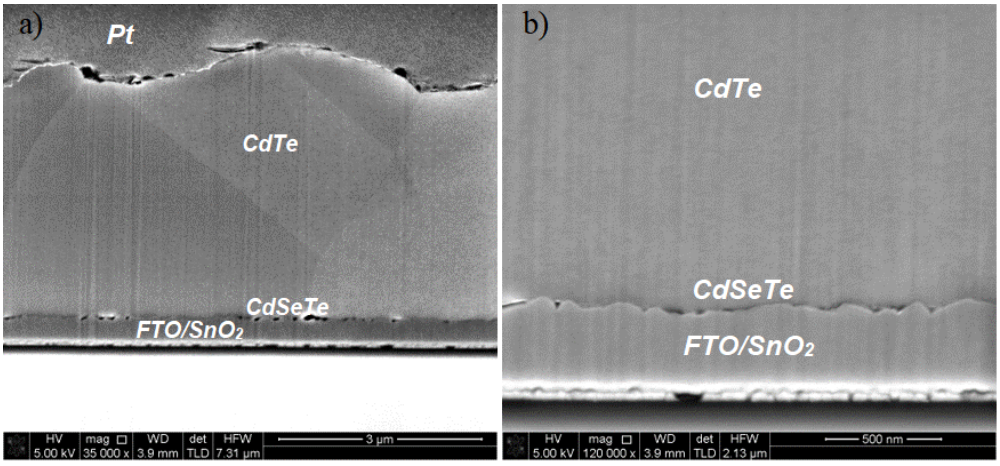

Figure 4.14: *SEM image showing the standard cross-section of 100 nm sample (a) at low mag 35000, (b) at high mag 120000 .*

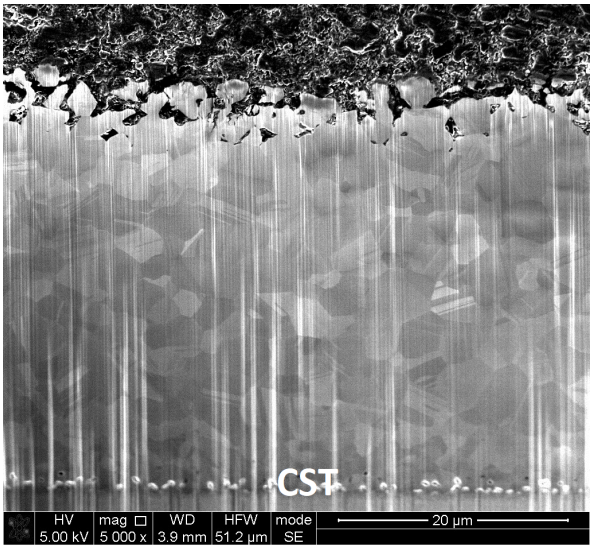

Figure 4.15: *SEM image showing the bevel cross-section at 8°.*

On the other hand, the elongated microstructure for the bevel cross-section at 8° for the same sample showed all grains and the voids more clearly in the inter-diffusion layer (labelled 'CST' for CdSeTe) as shown in Figure 4.15. The energy dispersive X-ray (EDX) results showed that Se is more likely to dissolve into the CdTe layer to form the CST region, as shown in Figure 4.16. The energy dispersive X-ray (EDX) results showed that Se is more likely to dissolve into the CdTe layer to form the CST region, as shown in Figure 4.16.

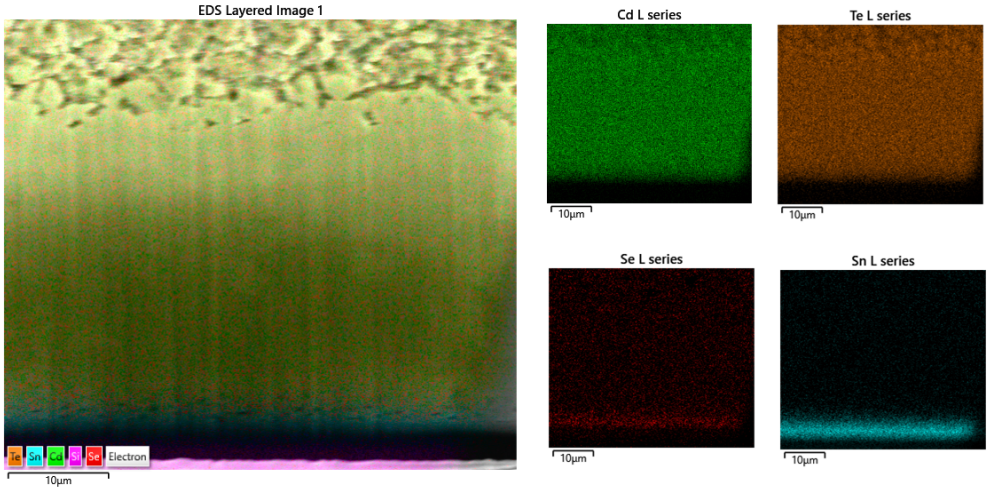

Figure 4.16: *Energy dispersive X-ray (EDX) image for the bevel cross-section at 8° showing the small amount of Se in the CST inter-diffusion layer.*

Electron backscatter diffraction (EBSD) map (Figure 4.17a) showed a slightly smaller grain size in the inter-diffusion CST layer, and that they are equiaxed. Likewise, the phase map (Figure 4.17b) confirmed a zinc blende phase throughout and did not show the hexagonal phase of CdSeTe as reported in two studies by Yanfa and Poplawsky *et al.* [54], [118].

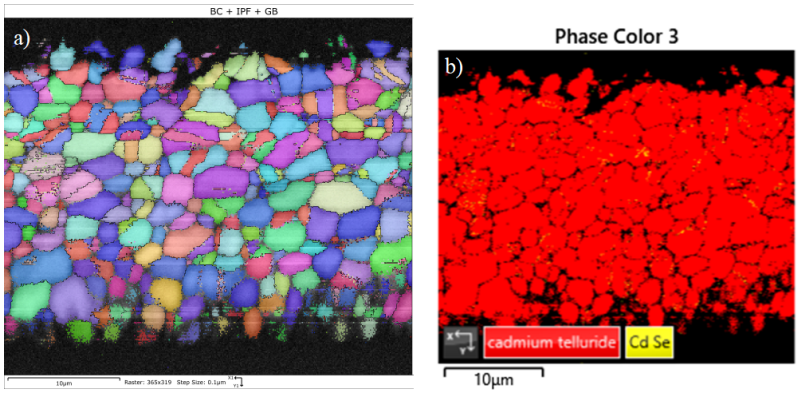

Figure 4.17: *(a) Electron backscattered diffraction (EBSD) image for the bevel cross-section at 8°, (b) phase map for the same area in (a). Red indicates the zinc blende crystal structure.*

CL panchromatic image showed a slightly lower intensity at the inter-diffusion layer as shown in Figure 4.18b. The secondary electron SEM image for the same area in Figure 4.18a also shows the small voids in the inter-diffusion layer.

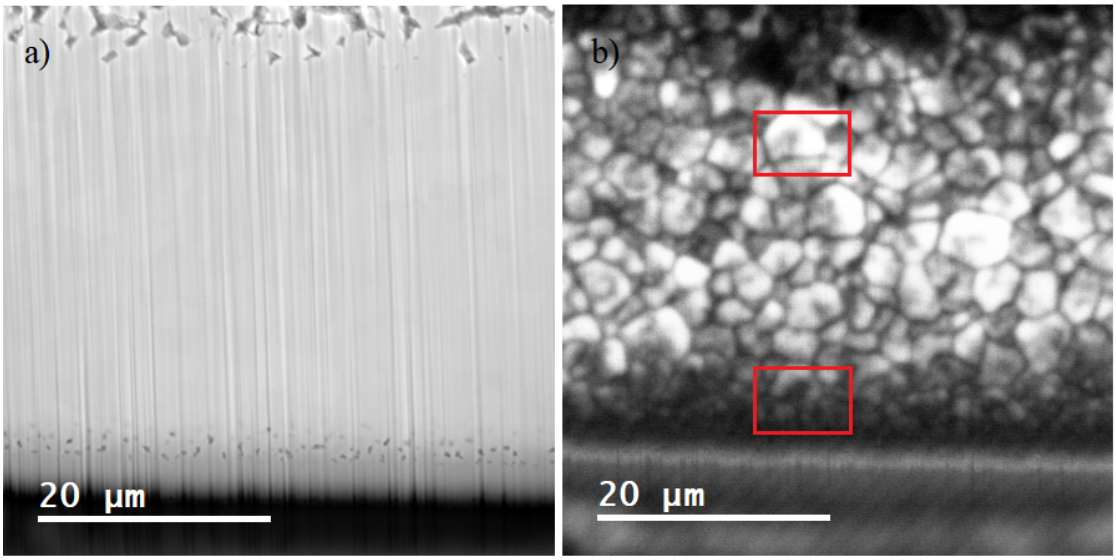

Figure 4.18: *(a) Secondary electron SEM image and (b) simultaneously acquired CL panchromatic image for the 100 nm CdSe sample bevel cross-section*

The CL hyperspectral map was acquired along the bevel cross-section. The CL spectrum was acquired from deep within the CdTe absorber layer and from close to the inter-diffusion layer (see Figure 4.18b). The CL spectra are shown in Figure 4.19. There is a red shift of the spectrum from the inter-diffusion region due to alloying with selenium. This is consistent with the EQE plot in Figure 4.4, where the onset of absorption is shifted to longer wavelengths in the 100 nm sample compared to 50 nm CdSe thickness.

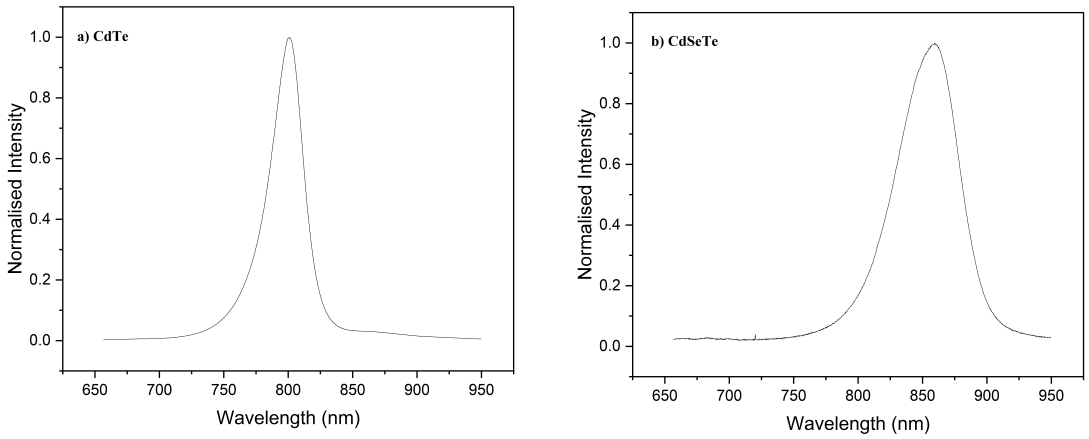

Figure 4.19: *(a) CL spectrum at CdTe layer (b) CL spectrum at inter-diffusion CdSeTe layer of 100 nm sample. The spectra were acquired from the two point labelled in Figure 4.19b.*

4.4.2 Sample with 400 nm CdSe

Figure 4.20 shows the grain structure and voids in the inter-diffusion layer of the standard cross-section in 400 nm sample. The voids observed are much larger compared to the sample with 100 nm of CdSe (Figure 4.14). As mentioned before (section 4.2) this device has a low efficiency. Paudel and Yan [55] also found that when the thickness of the CdSe layer was increased to 350 nm, the average J_{sc} decreased and then led to low overall efficiency.

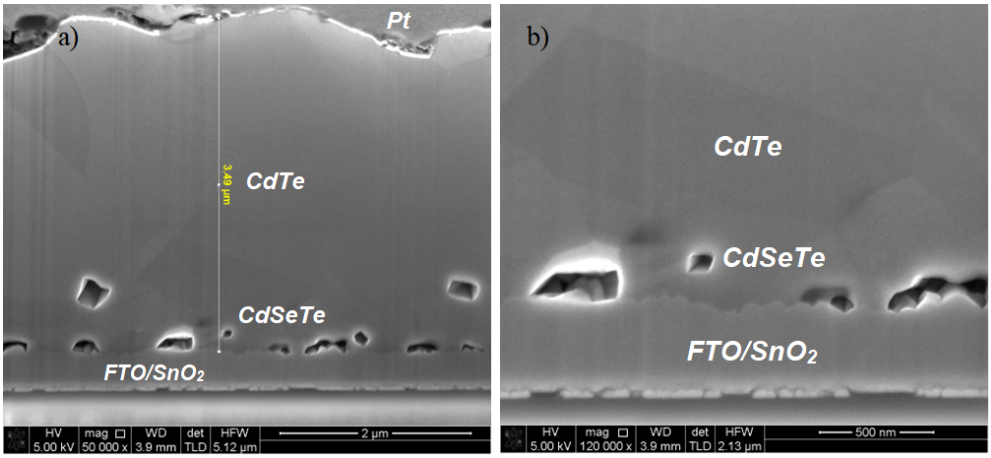

Figure 4.20: *SEM image showing the standard cross-section of 400 nm sample (a) at low mag 50000, (b) at high mag 120000.*

The bevel cross-section at 8° for the same sample is shown in Figures 4.21,4.22. The CL panchromatic image showed a low cathodoluminescence signal at the inter-diffusion CdSe-CdTe layer, where the dark black area emphasises the harmful defects that are causing high carrier recombination rates and overall drop in efficiency. The inter-diffusion CdSeTe layer has both small grain size and Kirkendal voids at the grain boundaries. We believe that the reason for the small grain size is because of the Se solute drag effect on the grain boundaries.

The fast speed of Se diffusion also created voids that further pinned the grain boundaries and prevented the grain from growing. This is discussed in more detail in Section (4.6).

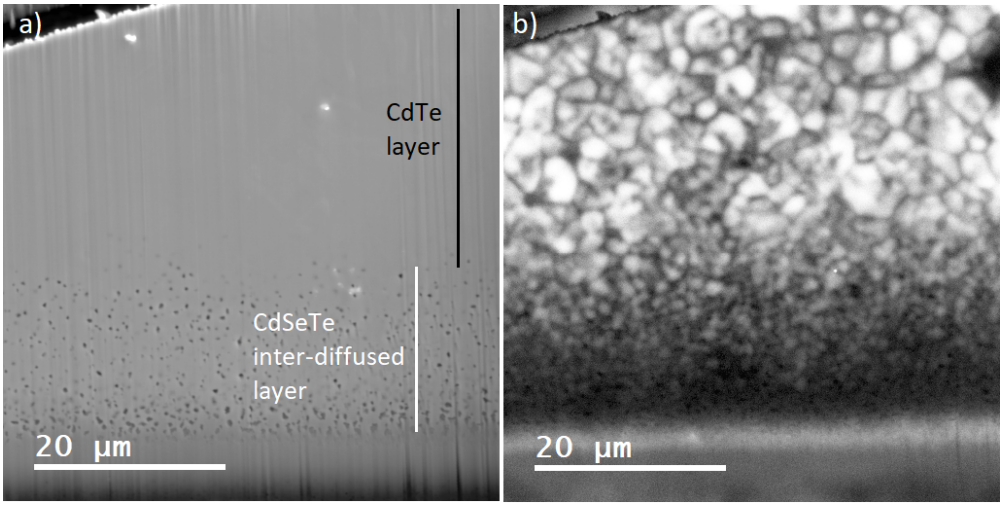

Figure 4.21: *(a) Secondary electron SEM image and (b) simultaneously acquired CL panchromatic image for the shallow 8° bevel cross-section for 400 nm CdSe sample.*

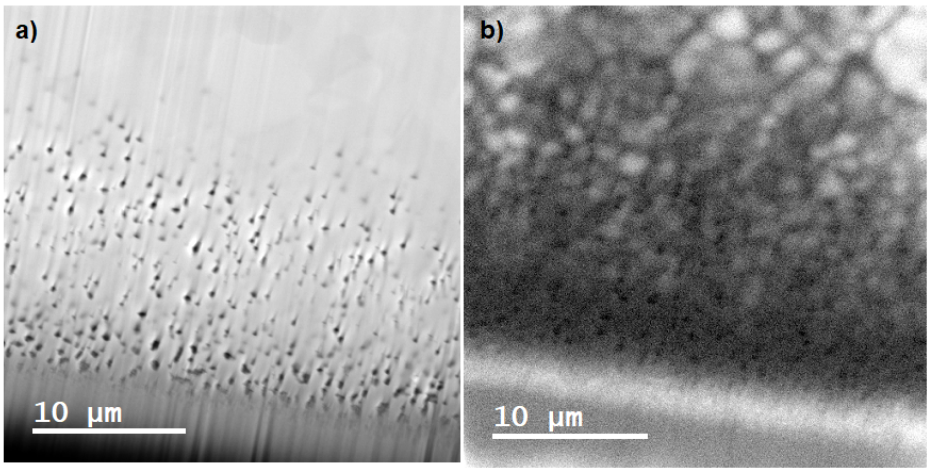

Figure 4.22: *(a) Secondary electron SEM image and (b) simultaneously acquired CL panchromatic image for the CdSeTe inter-diffused layer at the shallow 8° bevel cross-section.*

The EBSD results acquired for the 400 nm bevel cross-section were able to detect a clear Kikuchi pattern at the CdTe layer, but the quality of the pattern at the inter-diffusion CdSeTe layer was poor as shown in Figure 4.23b. The EBSD software was not able to identify the phase information in the inter-diffusion layer, as we can see a black unidentified area in the inter-diffusion CdSeTe layer of the EBSD map (Figure 4.23b) due to the small grains and voids in that area. Moreover, the EBSD map shows no change in the crystal structure for the regions that have been successfully indexed. Yanfa *et al.* [118] found the photoactivity

of the inter-diffusion layer is highly dependent on the crystalline structure of the alloy (i.e. zincblende or wurtzite) which is also dependent on the relative Se and Te concentration. Moreover, Poplawsky *et al.* [54] investigated CdTe/CdS interface, and found in both as-grown and $CdCl_2$ treated samples there is a significant Te-S interdiffusion in a few nanometres of CdTe solar cells, where the S was diffused to the CdTe grain interior. They noticed when more S diffused to substitute Te, the structure will transform from the zincblende phase to the wurtzite phase.

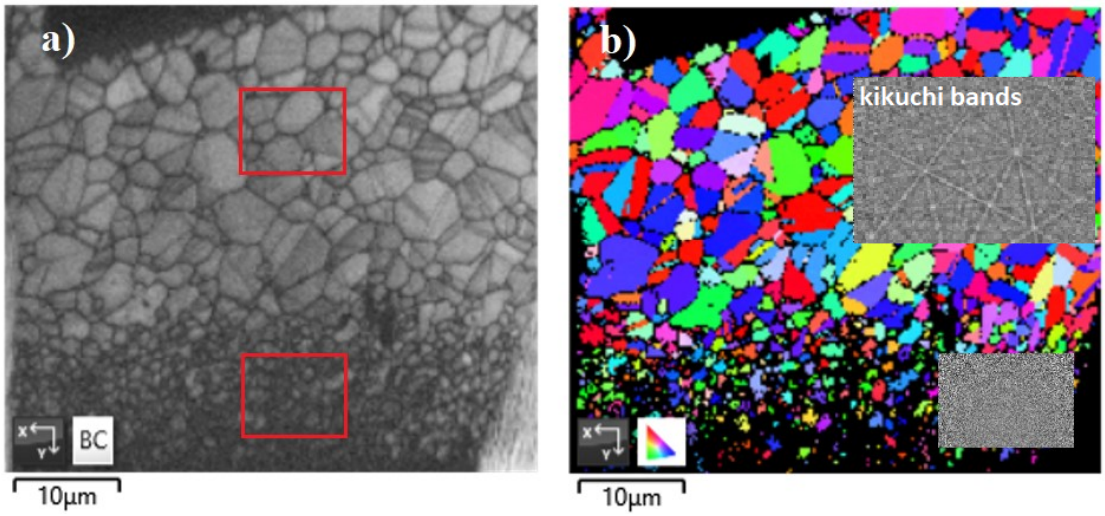

Figure 4.23: *(a) Band contrast and (b) EBSD map of 400 nm bevel cross-section. The insets in (b) show the quality of Kikuchi patterns from the CdTe and CdSe-CdTe inter-diffusion regions.*

The CL spectrum has been acquired from both CdTe and CdSeTe layers (see Figure 4.23 for the positions from which spectra were acquired). Figure 4.24a showed the CdTe layer CL spectrum peak was around 813 nm, corresponding to approximately 1.5 eV of energy, however Figure 4.24b showed the CL spectrum peak for CdSeTe layer at 879 nm or 1.4 eV of energy. Figure 4.25 shows the superimposed CL spectra close to the interface (CdSeTe-red) and distant from the interface (CdTe-black). For a more direct visual comparison the intensity was normalised to the highest value. The broad band-to-band recombination peaks indicated that there is a redshift at the CdSeTe inter-diffusion region where it has more Se concentration. The red shift of optical properties was due to Se alloying with CdTe. A similar redhsift of the CL peak with sulphur alloying has also been reported in CdS-CdTe solar cells [79].

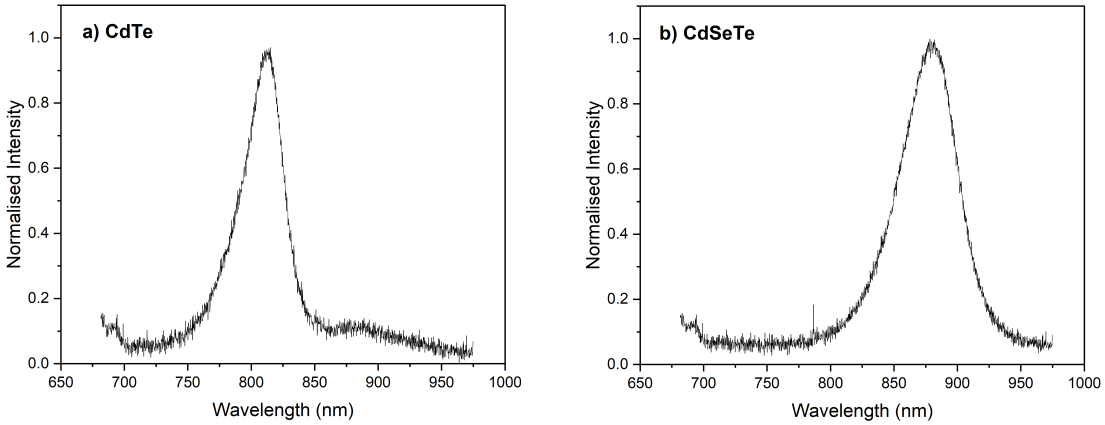

Figure 4.24: *(a) CL spectrum at CdTe layer (b) CL spectrum at inter-diffusion CdSeTe layer of 400 nm sample.*

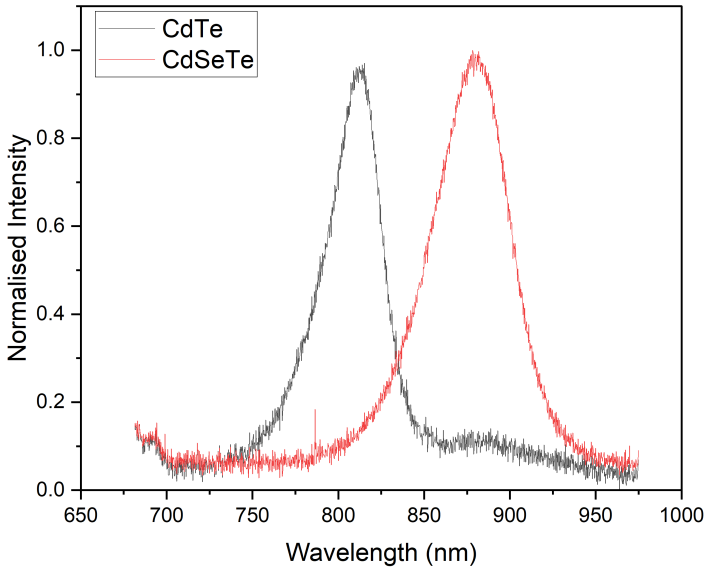

Figure 4.25: *The redshift of CL spectrum at the inter-diffusion CdSeTe layer for 400 nm sample.*

Fiducia *et al.* [119] used panchromatic cathodoluminescence (CL) measurements on the bevel of untreated CdSeTe/CdTe solar cells. The panchromatic CL images were acquired for normal CdTe without the CdSeTe layer and for CST/CdTe. They found that the panchromatic CL image of a 7° bevel on a CST/CdTe device showed more luminescence in the inter-diffusion layer, where the dark contrast is seen at the grain boundaries in the upper region of the bevel (the CdTe layer) as shown in Figure 4.26a. They referred to the higher luminescence signal in the CdSeTe material than in CdTe, indicating that selenium passivates defects in the grain

bulk. Also, a clear V-shaped drop in the CL signal at grain boundaries in CST layer and CdTe layer as well observed as shown in Figure 4.26b with an overall increase in the intensity at CST layer. This observation is not consistent with our CL measurements on the bevel of CdSe-CdTe where the drop in the CL signal was observed at the inter-diffusion CdSeTe layer. The reason for the discrepancy between our work and that of Fiducia *et al* [119] is due to a grain boundary solute pinning mechanism that is discussed in more detail in Section (4.6).

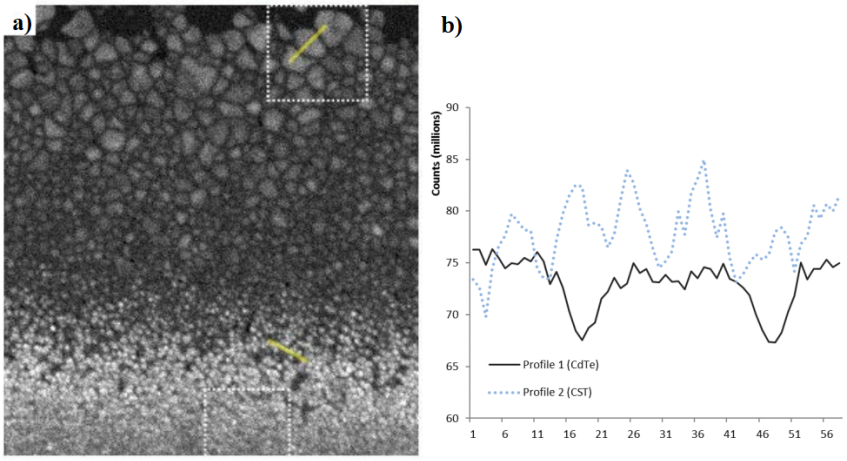

Figure 4.26: *(a) panchromatic CL image of a 7° bevel on a CST/CdTe device, The lines show regions used to create profiles in (b) CL intensity line profiles in the CdTe and CST regions of the bevel. [119]*

Figure 4.27 shows that Se diffused across grain boundaries, where the redshift observed from grain interior to grain boundary in the CL spectrum imaging data that is acquired at room temperature for our sample (Figure 4.28).

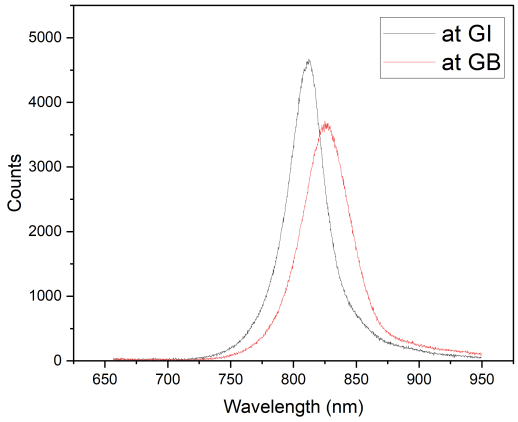

Figure 4.27: *The redshift of CL spectrum from grain interior GI to grain boundary GB at 400 nm CdSe sample.*

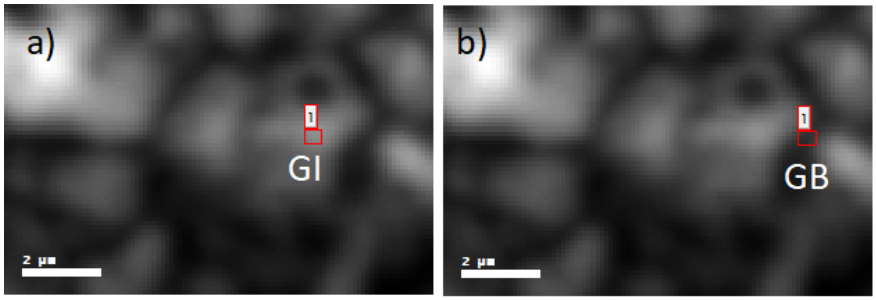

Figure 4.28: *The region used for extracting the CL spectrum at grain interior GI (a) and at grain boundary GB (b) for the 400 nm CdSe sample.*

Moreover, Colegrove *et al.* [120] investigate Se diffusion in CdTe thin films by examining Se diffusion in single-crystal and polycrystalline CdTe during deposition and $CdCl_2$ treatments by using dynamic secondary-ion-mass spectroscopy and Auger electron spectroscopy depth profiling and coupled with electron backscatter diffraction images of the crystalline structure. They noticed the Se was diffused in CdTe with higher rates during $CdCl_2$ treatments compared with thermal processing alone. Also, it diffused at a faster rate across the grain boundaries rather than bulk.

4.5 TEM results

Transmission electron microscopy (TEM) is an important technique for providing information regarding the structure. JEOL 2100F FEG TEM (field emission gun transmission electron microscope) was used in this work to acquire TEM, scanning TEM (STEM) and energy dispersive X-ray spectroscopy (EDX) data. The microscope was set up with 200 kV Schottky-type field emission gun, with a point resolution of 0.23 nm. A double tilting specimen holder was used to tilt crystals to zone axis allowing diffraction patterns to be obtained. The TEM data was acquired by Dr Budhika Mendis (Durham University).

Indexing of TEM diffraction patterns

CdTe is zincblende structured with cubic space group. Cd atom is bonded to four equivalent Te atoms to form corner-sharing CdTe tetrahedra. The interplanar distance between lattice planes is given by Eq 4.5.1, with a being the lattice parameter of the cubic unit cell. There are four cadmium atoms and four tellurium atoms per unit cell; the diffraction is determined by Bragg law and the structure factor F_{hkl}. In face-centered cubic crystals h, k and l should all be

even or all odd indices to get non-zero reflections, otherwise they will be forbidden reflections. In order to index the diffraction pattern, all reflections are listed in ascending order of $1/d_{hkl}$ and forbidden reflections are eliminated. Then experimentally from the obtained diffraction pattern, the two shortest reflections with their measured d_{hkl} (Eq 4.5.1) is determined. These d-spacing values are compared to the list of possible reflections, to find the closest match which corresponds to the family of planes. The Miller indices for the two shortest reflections are assigned in such a manner that the angle between the two planes equals the angle measured between two reflections in the diffraction pattern. The right-hand rule and cross-product will give the beam direction and crystal zone-axis. By using vector addition, all other reflections of the diffraction pattern can be constructed.

$$d_{hkl} = \frac{a}{\sqrt{h^2 + k^2 + l^2}} \tag{4.5.1}$$

4.5.1 Sample with 100 nm CdSe

Similar to the standard cross-section STEM bright field (BF) and dark field (DF) images (Figure 4.29) did not show any small grains at the CdSe-CdTe interface. Instead FTO/SnO_2 followed by a thin porosity layer was observed at the CdSeTe inter-diffusion layer. One large grain appeared in the image, which extended through the thickness of the absorber layer. In order to verify that this was a single grain diffraction patterns were obtained from the top and the bottom of the STEM BF images, as indicated by the annotated circles in Figure 4.30 showed the one grain annotated at the top and the bottom. Both TEM diffraction patterns obtained have the same indexed diffraction pattern, which means they originate from the same grain.

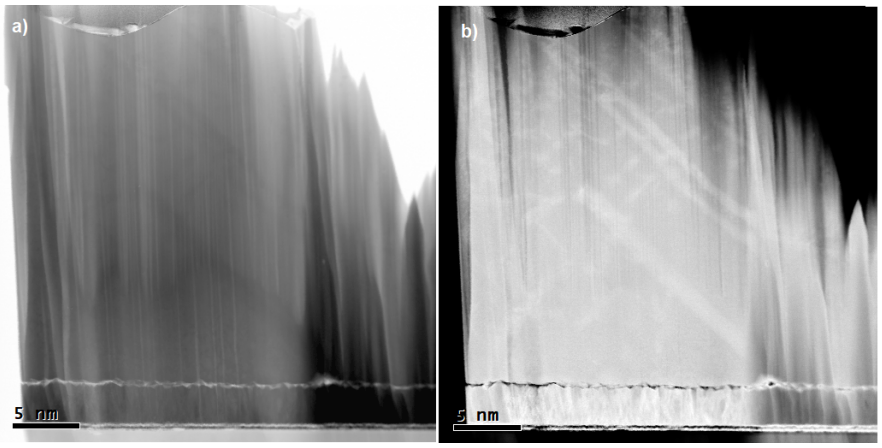

Figure 4.29: *(a) STEM Bright field image for 100 nm sample. (b) STEM Dark field image for 100 nm sample.*

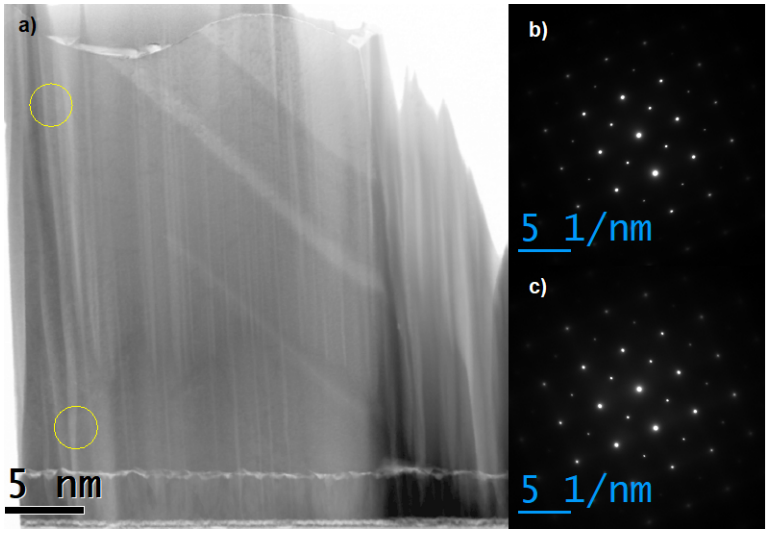

Figure 4.30: *(a) STEM Bright field image for one grain of 100 nm sample. Diffraction patterns in (b) and (c) were obtained from the top and bottom circular regions shown annotated in (a) respectively.*

Figure 4.31 shows the indexed diffraction pattern for the top and the bottom of this grain. Two basis vectors 200 and $0\bar{2}0$ were identified. The experimental measured d_{hkl} spacing for the 200 reflection was 0.3567 nm, which is near the theoretical value of 0.3787 nm. The small difference between the two values might be due to the effect of Se alloying on the lattice parameter. The angle between 200 and $0\bar{2}0$ was 90° and the beam direction was [001].

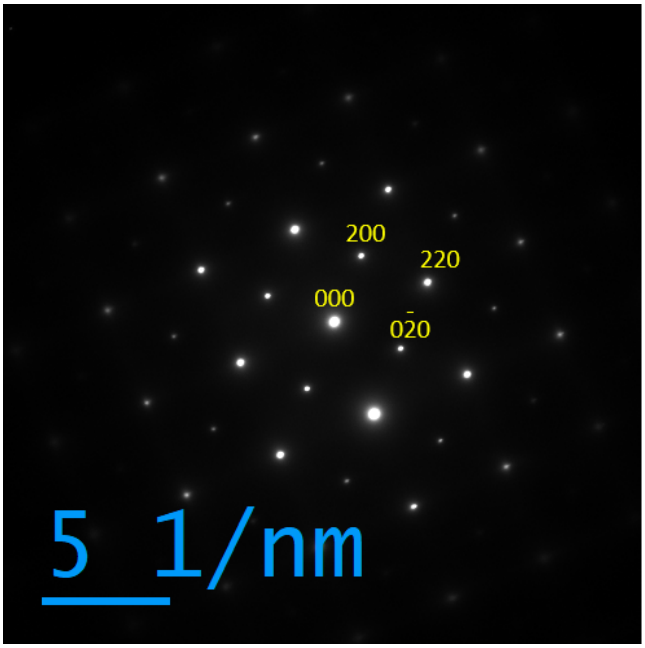

Figure 4.31: *Indexed diffraction pattern for the 100 nm Se sample grain shown in Figure 4.28. The zone axis is [001].*

TEM-EDX map shown in Figure 4.32 was acquired across the inter-diffusion CdSeTe layer, where no distinct CdSe layer was observed in the Se map. The Se looks to be diffused regularly through the grain interior, leaving behind a porosity layer.

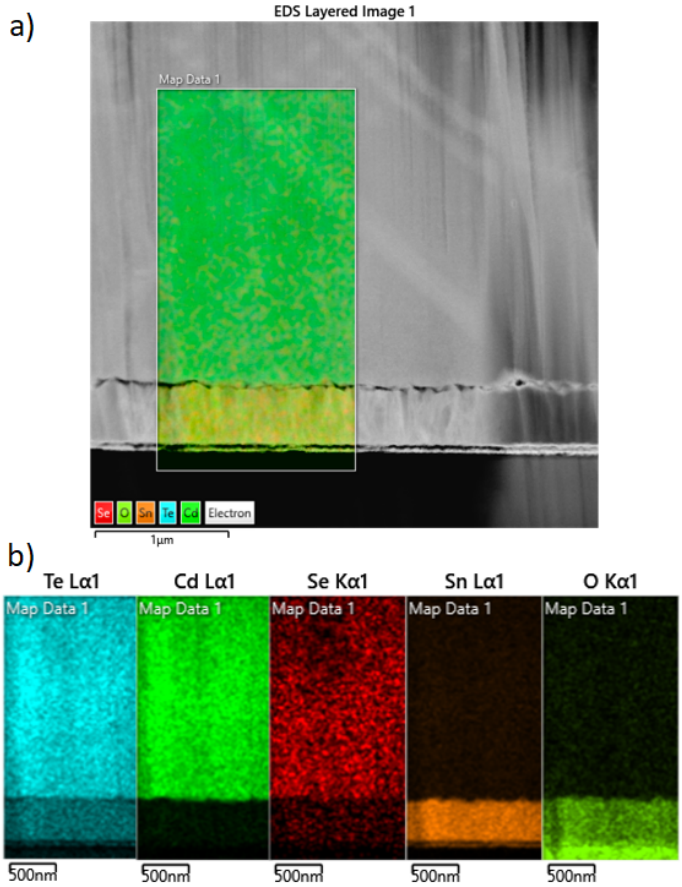

Figure 4.32: *a) STEM dark field image showing the region where EDX maps were acquired. b) STEM-EDX maps for Te, Cd, Se, Sn and O respectively in 100 nm CdSe-CdTe sample.*

4.5.2 Sample with 400 nm CdSe

Dark field and bright field STEM images (Figure 4.33) showed the FTO/SnO_2 layer followed by the CdSe-CdTe inter-diffusion layer which has a small grain size, as well as voids at the grain boundaries, especially at the triple points. In the dark field image (Figure 4.33a), the size of the grains was more visible, and the upper CdTe region showed larger grains. The grains are not clear in the bright field STEM image due to the sample being thick.

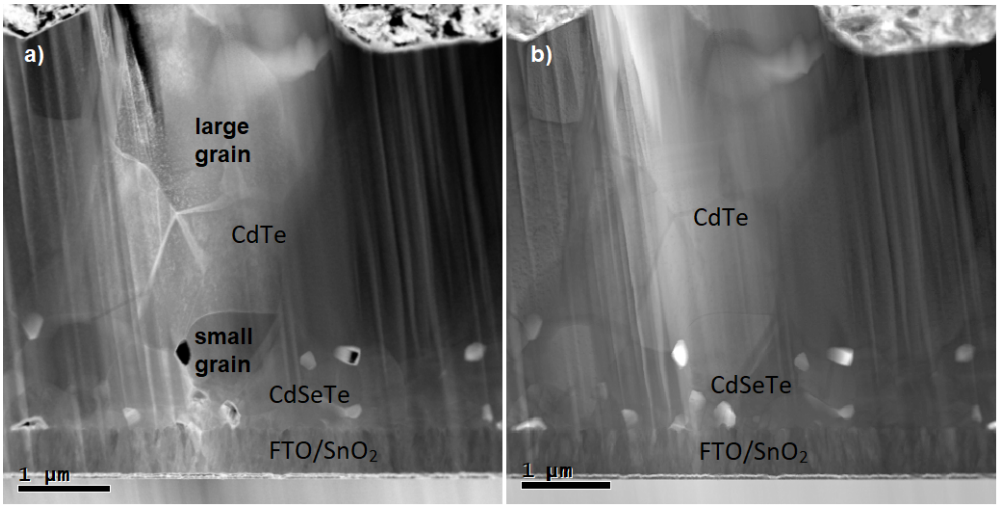

Figure 4.33: *(a) STEM dark field image for 400 nm sample. (b) bright field STEM image showing the small grain size at the inter-diffusion CdSe-CdTe layer, and the voids at grain boundaries.*

Figure 4.34 shows high magnification images for the previous figure. It shows clearly the layers and the porosity at the inter-diffusion CdSe-CdTe layer with a small field of view that contains some grains.

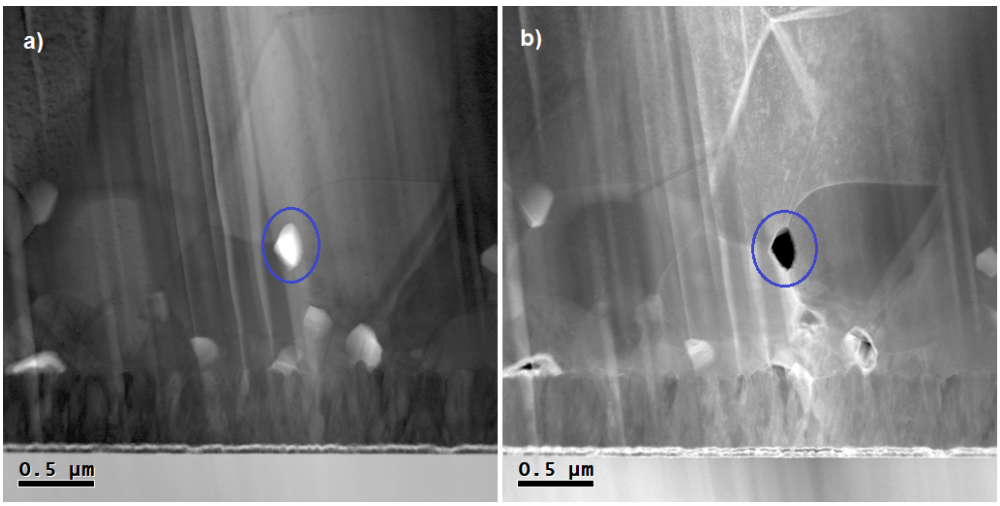

Figure 4.34: *(a) high magnification STEM bright field image (b) high magnification STEM dark field image shows clearly the voids (blue circle) at the inter-diffusion CdSe-CdTe region for 400 nm sample.*

TEM diffraction patterns were acquired for one grain at the CdSeTe inter-diffusion layer as shown in Figure 4.35a with specimen tilt X at 5.9° and Y tilt at 3.9° (Figure 4.35b). Figure 4.36 shows that the pattern is indexed as a face centred cubic structure with 220 and 202 vectors and [1$\bar{1}$ $\bar{1}$] beam direction. Moreover, when the sample was tilted along X axis to -14° and along Y axis to -2.4° a different diffraction pattern was observed (Figure 4.35c). The diffraction pattern shown in Figure 4.37 was indexed with cubic structure with two basic vectors 1$\bar{1}$1 and 220 and 90° between them. The beam direction was [1$\bar{1}$ $\bar{2}$]. Therefore, unlike the wurtzite phase reported in previous studies [54], the crystal structure in the inter-diffusion region for our samples consists of cubic zincblende phase. This is confirmed by both TEM and EBSD (Figure 4.23).

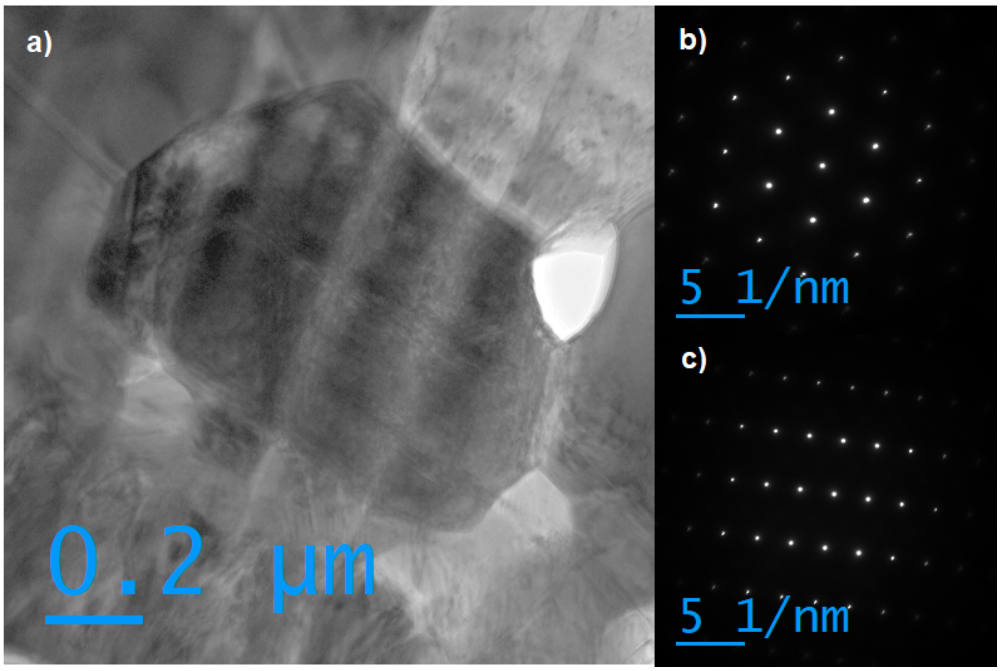

Figure 4.35: *(a) Bright-field STEM image showing one grain at the inter-diffusion CdSe-CdTe layer. (b) The diffraction pattern at TX 5.9°, TY 3.9° for the grain (a). (c) The diffraction pattern at TX -13°, TY -2.4° for the grain (a).*

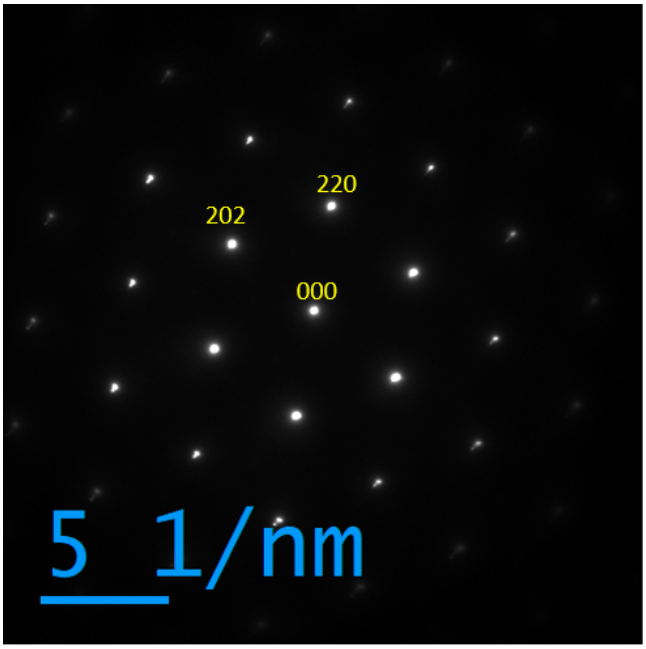

Figure 4.36: *The TEM diffraction pattern at TX 5.9°, TY 3.9° for the grain at the inter-diffusion CdSeTe layer.*

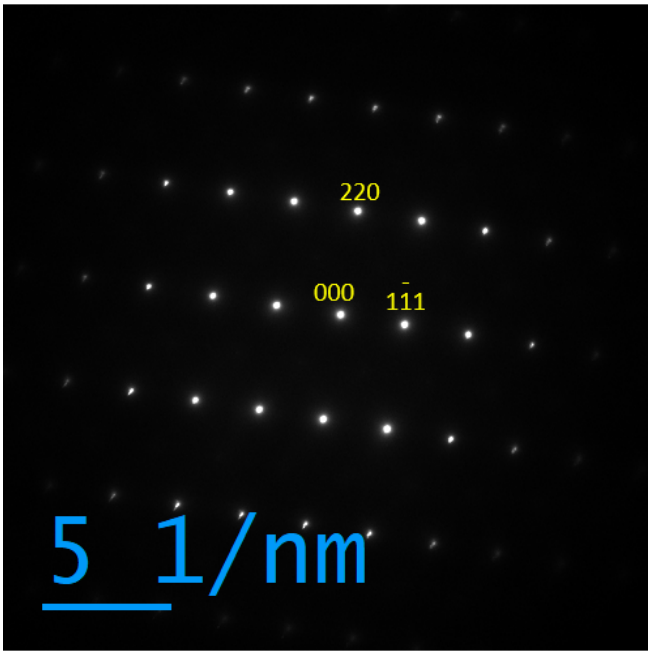

Figure 4.37: *The TEM diffraction pattern at TX -13°, TY -2.4° for the grain at the inter-diffusion CdSeTe layer.*

To study the behaviour of Se concentration across the voids and GBs at the CdSeTe inter-diffusion layer, EDX map results were collected by using TEM as shown in Figure 4.38. TEM results showed quite a high Se concentration at the CdSe-CdTe interface. It showed a

concentration gradient through the inter-diffusion layer. Even though the EDX result showed that Se concentration is high within the inter-diffusion layer, Se did not passivate the grain boundaries where the low CL intensity was observed at the inter-diffusion layer (Figure 4.21). This result is not in agreement with Fiducia *et al.* [48] as they found that grains have been strongly passivated at the inter-diffusion layer where they detect high CL intensity.

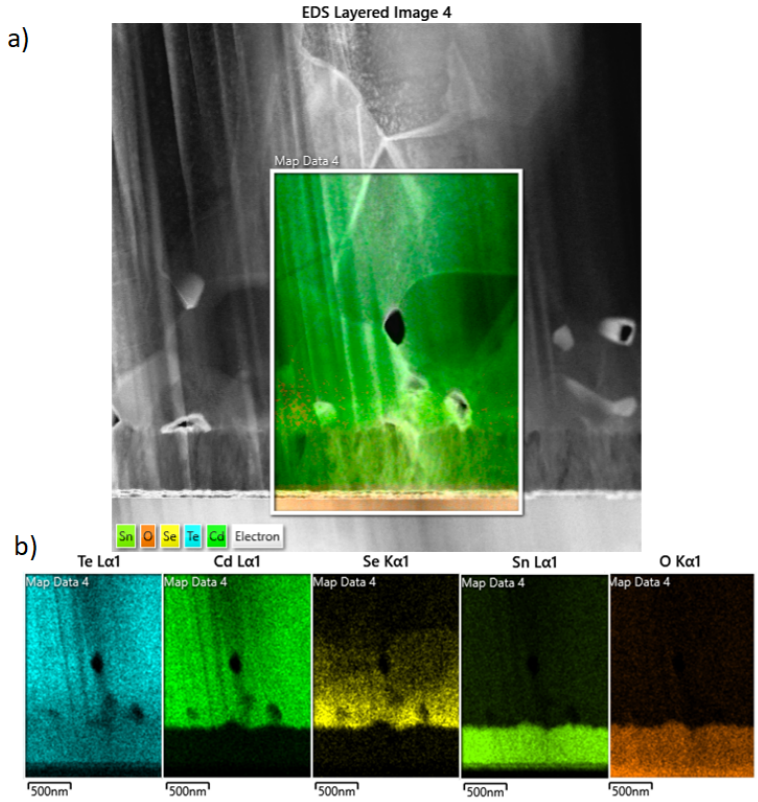

Figure 4.38: *a) STEM dark field image showing the region where EDX maps were acquired. b) STEM-EDX maps for Te, Cd, Se, Sn and O respectively in 400 nm CdSe-CdTe sample.*

4.6 Se solute drag effect by moving grain boundary

Our TEM and EBSD results revealed that the drop in efficiency in the sample with the CdSe thickness of 400 nm is not due to a wurtzite structure that formed at the CdSe-CdTe layer [54]. We propose the small grains and voids that formed at the inter-diffusion CdSeTe layer are due to the solute drag and Kirkendall effects, as described below. Therefore, there is a need to outline the solute drag and Kirkendall mechanisms to understand their crucial effect to control material properties. The solute-drag effect was first described by Cahn in 1962. It is a phenomenon that occurs when solute atoms are present at grain boundaries during grain boundary movement, which can cause changes in grain growth and microstructure

development [121]. Solute drag occurs when the motion of grain boundaries is impeded by the presence of Se atoms (solute atoms) at the grain boundary. These Se solute atoms create obstacles that prevent the movement of grain boundaries. His theory found that the solute atoms at grain boundaries result in the migration of the grain boundary while dragging the solute atoms along with it [122].

In detail, during Se alloying to form the CdSeTe inter-diffusion layer, Se diffused from CdSe to CdTe layer. Se diffusion is expected to be fastest along free surfaces and grain boundaries. As shown in Figure 4.39 during the initial stages of CdTe deposition, Se enriches the surfaces of CdTe islands. As the deposition time increases the islands merge to form grains, and the grain boundaries are decorated with Se. The solute pinning will take place at this stage because of Se at grain boundaries, which opposes grain growth. Therefore, the solute drag effect describes two opposing processes where the grains grow to reduce the grain boundary energy, but selenium atoms try to segregate to the grain boundary to lower the segregation energy, leading to a moving grain boundary with Se cloud.

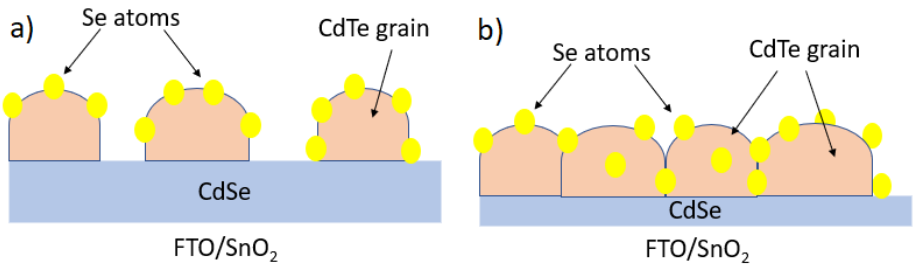

Figure 4.39: *A schematic diagram showing the origin of the Se solute drag effect.*

The solute drag effect depends on the velocity of the grain boundary and the solute diffusion. Figure 4.40 shows the classical model of grain boundary solute drag. First regime at low grain boundary velocities shows a higher force for grain growth due to the drag effect of the Se atom cloud (Drag area in Figure 4.40). The second regime breaks occur at high grain boundary velocities (Breakaway area in Figure 4.40), and at this stage, Se atoms are not able to keep up with the moving grain boundary. The grain boundary therefore breaks away from the Se cloud and shows grain growth characteristic of a pure material. [123].

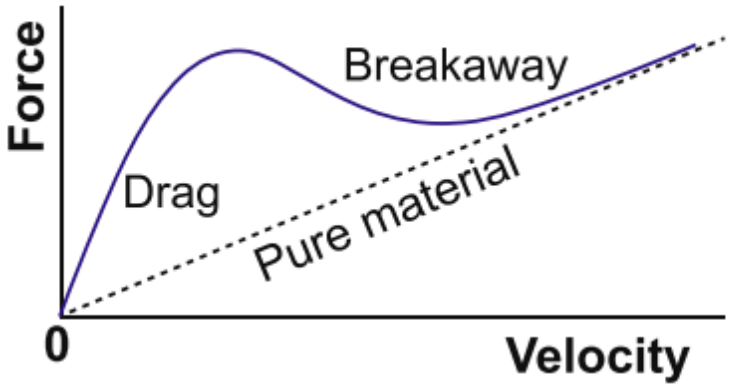

Figure 4.40: *Force-velocity diagram according to the classical model of grain boundary solute drag. [123]*

Our result shows the drag regime. The free energy is high at the inter-diffusion CdSeTe region, as it has many grain boundaries. We can describe the drag regime in our result where the Se solute drags with the grain boundary movement during growth. First, at the stationary grain boundaries, a high Se (solute) concentration diffused through grain boundaries to segregate and lower the free energy. Here, the change in the energy is negative because Se atoms settled at the grain boundaries, while if the grain boundary breaks away from Se and moves to a new position, the free energy will increase due to no Se at the grain boundary. The difference in free energy between the grain boundary with and without Se enrichment gives rise to a pinning force during grain growth, which is larger than a pure material. The pinning force gives rise to small grains within the CdSeTe inter-diffusion layer.

Voids due to Kirkendall effect was also observed in our result, as shown in Figure 4.41 [124]. For each atom jump to fill a vacancy, a vacancy will move the opposite way. For one type of atom, the rate of flow of atoms equals the rate of flow of vacancy. For our material, CdTe is the p-type layer and CdSe is n-type. Te diffuses to CdSe layer and Se diffuse to CdTe layer. When Te atom jumps to CdSe layer, the vacancy will jump to fill the original place of the Te atom. Similarly for Se to jump to CdTe the vacancy fill the place left behind by Se. In case of Se diffusing faster, this will lead to many vacancies flowing in the opposite direction. This accumulation of vacancies is called Kerkendal porosity, and is a result of unequal vacancy fluxes between the two layers at the interface CdSe-CdTe [117]. The formation of voids at the inter-diffusion layer for large CdSe thickness samples has been observed in the literature [125]. Also, voids were found at the triple grain boundary junction, which might also pin the grain boundaries and reduce their mobility.

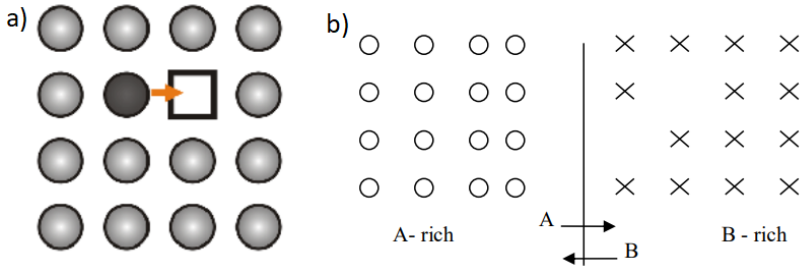

Figure 4.41: *a) Vacancy assisted diffusion in a pure materials and b) between two different materials, labelled 'A' and 'B'. For the latter differences in diffusion rates for 'A' and 'B' gives rise to Kirkendall voids. [124]*

Therefore, the free surface voids and large grain boundary area lead to high recombination rates as shown by the lower CL signal. This results in the dramatic drop in EQE observed for the 400 nm CdSe sample (Figure 4.4).

4.7 Conclusion

In conclusion, the Se diffusion from CdSe to CdTe layer has been investigated to explain the reason behind the low efficiency for the thicker CdSe layer sample. Two devices with different thicknesses (100 nm and 400 nm) of CdSe were compared. Both standard and bevel cross-sections were performed. Kirkendall voids were observed in both samples, although a much thicker layer of porosity was observed in the 400 nm sample. Small grain size was also observed at the inter-diffusion layer in the 400 nm sample. A high recombination rate was found for the CdSeTe inter-diffusion region in the CL panchromatic image results for the 400 nm CdSe sample. The redshift of the CL spectrum at the inter-diffusion layer was observed in both samples, due to Se alloying. TEM-EDX map across the inter-diffusion layer showed Se diffused more uniformly in 100 nm compared to 400 nm. Face-centred cubic structure observed in our TEM diffraction patterns indicate that the high recombination rate at the inter-diffusion layer is not because of the hexagonal wurtzite structure as proposed in the literature [54]. Se solute drag and Kirkendall voiding mechanisms are proposed as the origin for the loss in device efficiency.

Chapter 5

Further analysis of Se diffusion and lifetime measurements

5.1 Motivation

This chapter will introduce the STEM-EDX line scan results and CL spectrum imaging to study and focus more on Se diffusion across the inter-diffusion region (CdSeTe layer) of 400 nm CdSe sample, specifically, to measure Se diffusion coefficient using CL and STEM-EDX. The knowledge of diffusion coefficient will enable to design CdSeTe solar cells, which will help to optimise the temperature and annealing time for a specific thickness of the inter-diffusion layer. Moreover, the time-resolved cathodoluminescence was used to measure the carrier lifetime in CdTe and CdSeTe regions to compare it with the CL intensity observed in chapter 4.

5.2 Time-resolved cathodoluminescence instrumentation

Time-resolved cathodoluminescence Attolight microscope at Cambridge University was used to acquire our time-resolved cathodoluminescence (TRCL) results. In order to optimise the efficiency of a photovoltaic device, it is critical to measure carrier lifetime with high spatial resolution at grain boundaries. TRCL is a technique that provides information about the carrier lifetime in the material. As mentioned earlier standard cathodoluminescence technique (chapter 2) uses continuous waves of electron beam while in the time-resolved cathodoluminescence technique, electron pulses are used to hit the sample and produce luminescence. A pulsed electron beam is produced using the photoelectric effect. Even if we only excited one electron per pulse, that would create enough electron-hole pairs in the material to generate light where the intensity will be a function of time [126]. In detail, the time measurement will describe how fast the luminescence decays; many electron pulses are used to gradually build up the intensity as a function of the time for the whole measurement, as each photon is emitted at a different time. This will show more photons emitted at a short time (fast) compared to a long time (slow), providing an intensity plot versus the decay time. From the exponential decay, we can measure the carrier lifetime (τ) by using the following formula:

$$I = I_0 \, \mathbf{exp}\frac{-t}{\tau} \tag{5.2.1}$$

where I is the intensity, t is the time, τ is the lifetime, and I_0 is the luminescence intensity at t = 0.

The lifetime is calculated by measuring the CL-decay after the sample has been excited by an electron beam pulse. Early investigations of the carrier lifetime were by using the

beam blanker in the standard SEM to generate an electron pulse, where the electron beam was diverted away from the axis of the electron optical column using a set of electrostatic deflection plates [126]. This means that the electron beam is not continuously illuminating the sample but blanked to measure the decay time. The disadvantages of this experimental method are that the beam sweeps the sample, and the minimum pulse length is a few tens of nanoseconds. This causes the semiconductor to be excited in a steady state, and the temporal information about the luminescence is collected during the decay of the light and the time resolution is limited to a few hundred picoseconds. An alternative approach to time resolved measurements is to replace the classical tungsten electron gun in an SEM with a 20 nm thick gold photocathode as shown in Figure 5.1. When the photocathode is illuminated by a laser with 80 MHz repetition rate, a pulsed electron beam (100 femtosecond pulse length) is generated, and then a streak camera located behind a monochromator is used in photon counting mode to work as a time-resolved detector. This method can provide higher temporal resolution ($\approx$ 10 picoseconds) and secondary electron images of spatial resolution better than 50 nm as shown in Figure 5.2. [126].

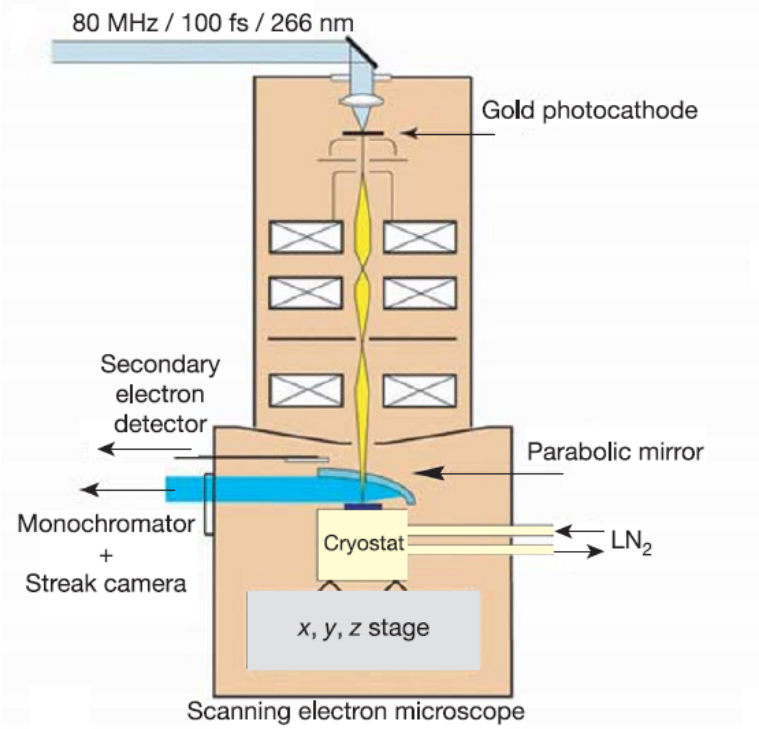

Figure 5.1: *Schematic diagram of time-resolved cathodoluminescence system. [126]*

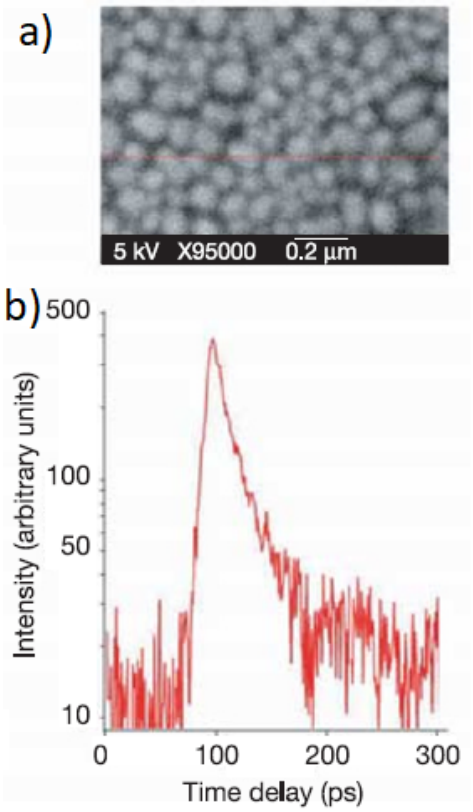

Figure 5.2: *a) The Secondary electron image and b) time-resolved CL spectrum from the microscope in Figure 5.1. [126]*

There are two methods for detection, first is time-correlated single photon counting (TCSPC), which is a technique for reconstructing the lifetime decay over multiple events by synchronising the arrival of single photons on a detector (PMT) with the timing of a pulsed excitation source. Photon detection events are sequentially recorded using timing electronics in the form of a time-to-digital converter until enough statistics are acquired to reconstruct the decay. The lifetime decay is then represented as an exponential function [127]. The electron beam current density needs to be low to emit a single photon (because the detector is not able to process two photons at the same time which leads to measurement artefacts).

The second detection method is by using a streak camera (Figure 5.3) which uses wavelength dispersion. An ellipsoidal mirror collects the CL-light, which is then dispersed in a monochromator. All the wavelengths pass through a slit, and strike a photocathode, which converts photons into electrons. There are two electrical plates before the CCD camera where the voltage increases linearly with time. The electric field between the plates deflects the electrons generated by the light. Electrons generated by light emitted at a later stage will be deflected more, due to the higher voltage between the plates. In this way electrons from the photocathode are dispersed according to the time of their generation. The CCD camera will

detect the photon wavelength as a function of the time, providing an intensity plot versus streak time [128], This method is able to show part of the whole spectrum, and might therefore not be suitable for some materials because the camera is not sensitive in the wavelength region of interest.

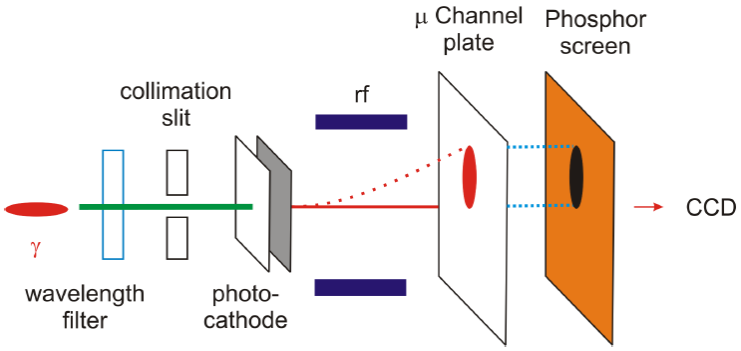

Figure 5.3: *The principle of a streak camera. [129]*

5.3 Time-resolved cathodoluminescence (TRCL) results

Time-resolved cathodoluminescence is a critical technique to gain a deep understanding of the optical and electronic properties of nanoscale materials. It combines two important techniques, namely cathodoluminescence and time-resolved spectroscopy to measure the emission of light from a material over a short time period, often in picoseconds (10^{-12} seconds) to nanoseconds (10^{-9} seconds). This will allow us to observe and analyse the dynamics of carrier recombination processes. It helps in understanding how quickly charge carriers recombine. In detail, the time-resolved cathodolumencense is a technique that allows the CL signal variation to be recorded over small-time scales. The lifetime decay is then represented as an exponential function, where the intensity is a function of the time [126], [127].

Time-resolved cathodoluminescence results using the streak camera technique were acquired by Dr Gunnar Kusch at Cambridge University. The microscope operating voltage was 3 kv and the specimen was cooled with liquid nitrogen to 80 K. Measurements were performed on the bevel cross-section 400 nm CdSe sample at both the inter-diffusion CdSeTe layer and the CdTe layer to understand more about the recombination rate and to measure the average lifetime at both regions. Figure 5.4 shows the TRCL data collected at one grain interior of the CdTe layer, which has large grains. Figure 5.4a shows a (false colour) secondary electron image of the CdTe region. The cross-hair indicator shows the electron beam position, which is placed within the CdTe grain interior. Figure 5.4b shows the acquired streak camera image

which represents the time decay of the luminescence signal as a function of wavelength. The luminescence peak appeared at 787 nm, with a range 770 - 800 nm. Since the data was acquired at 80 K temperature the CL peak could represents the A^0X bound exciton (i.e. exciton bound to a neutral acceptor) decay [130] as shown in the integrated decay curve as a function of the wavelength in Figure 5.4c. However, the peak shape is asymmetrical and appears broader at short wavelengths, which suggests an overlap of A^0X luminescence with band-to-band recombination. Unfortunately, due to the limited spectral resolution of the measurement, it was not possible to separate overlapping band-to-band and A^0X peak contributions.

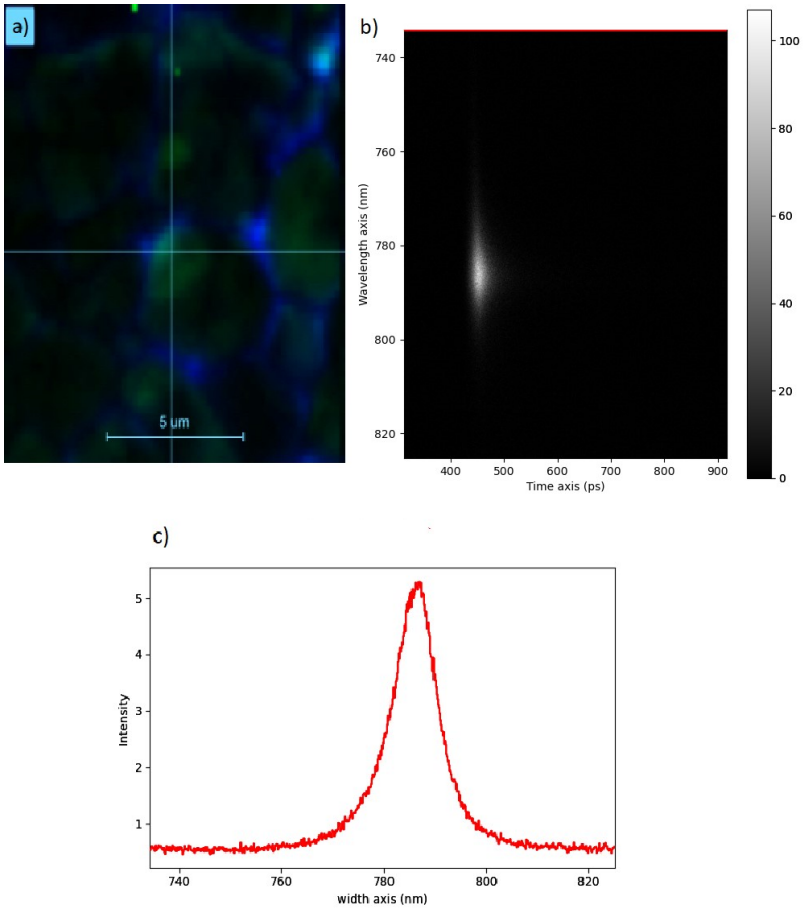

Figure 5.4: *a) Secondary electron image with the electron beam positioned at one of the grain interiors in the CdTe layer, b) Streak camera image as a function of wavelength, c) The time integrated CL spectrum at the grain interior.*

Based on Equation 5.2.1, the CL decay curve was least squares fitted to a function of the form:

$$I(t) = I_0 \, \mathbf{exp}(\frac{-t}{\tau}) + c \tag{5.3.1}$$

where the additional constant 'c' is used to model the background. I_0, τ and c are therefore

fitting 'variables'. Time $t = 0$ is defined as the peak intensity position of the CL decay curve. The result of this exponential fitting is shown in Figure 5.5. The black curve represents the raw data, and the red curve is the fitted data. The lifetime was 18.2 ± 0.1 ps.

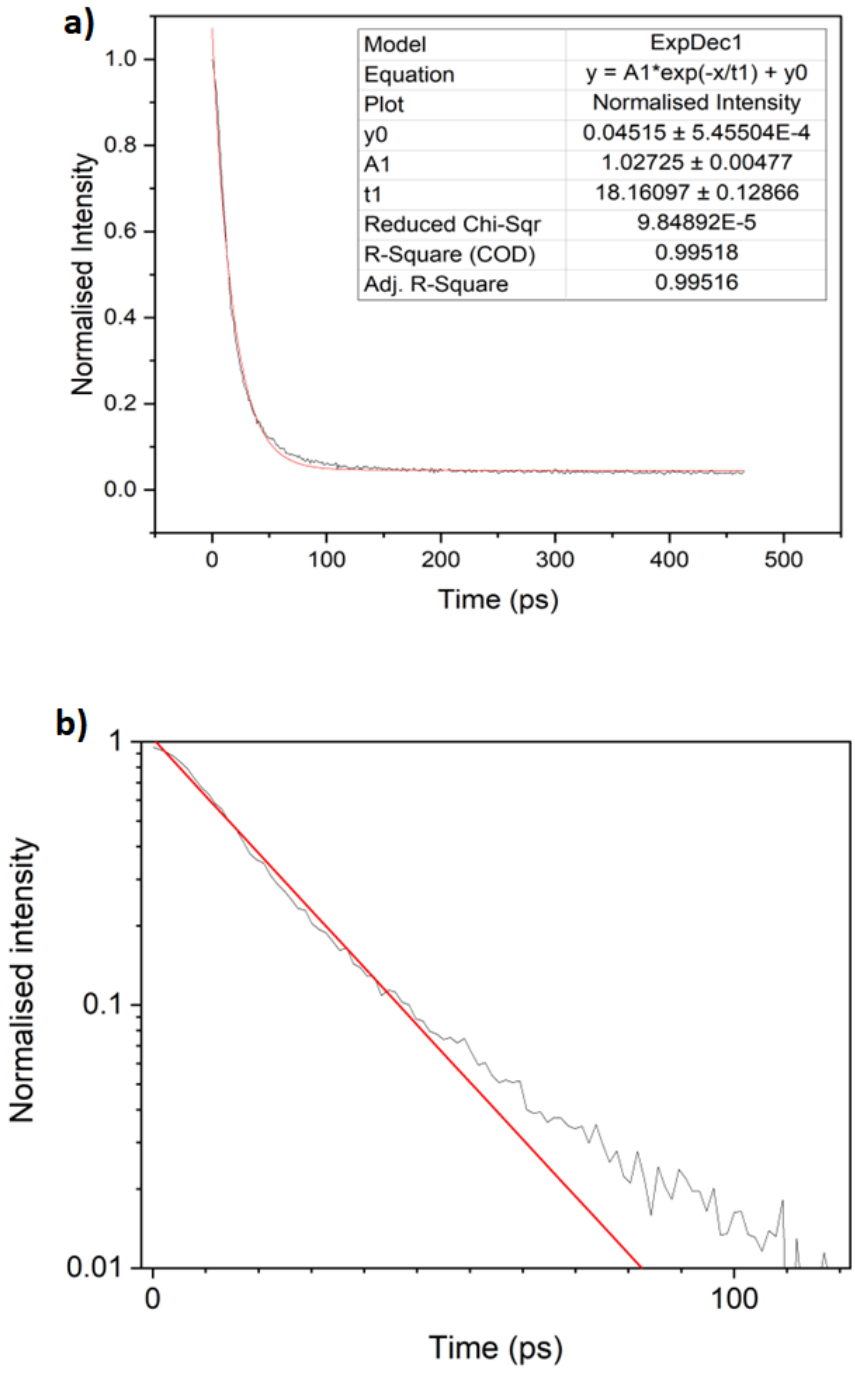

Figure 5.5: *a) The exponential fitting of TRCL decay, b) The exponential decay fitting in logarithmic scale to the streak image in Figure 5.4b (CdTe grain interior).*

An equivalent TRCL result for the same CdTe region is shown in Figure 5.6, but with the

electron beam positioned at one of the grain boundaries. A 13.9 ± 0.2 ps carrier lifetime was calculated from this data set. If we compare this result with the previous 18.2 ps lifetime in the at grain interior, we can conclude that the lifetime at the grain boundary is smaller than the lifetime at the grain interior, and this is because of the defects at the grain boundary which works as non-radiative recombination centres.

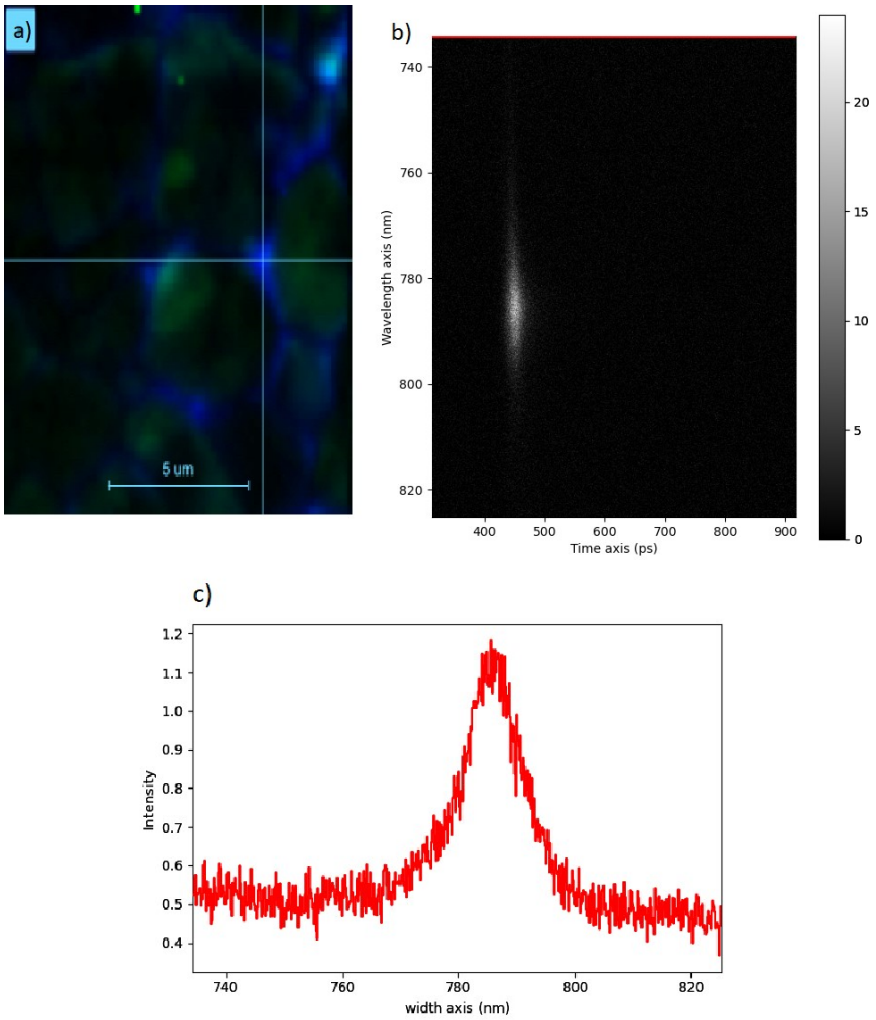

Figure 5.6: *a) Secondary electron image with the electron beam positioned at one of the grain boundaries in the CdTe layer, b) Streak camera image as a function of wavelength, c) The time integrated CL spectrum at the grain boundary.*

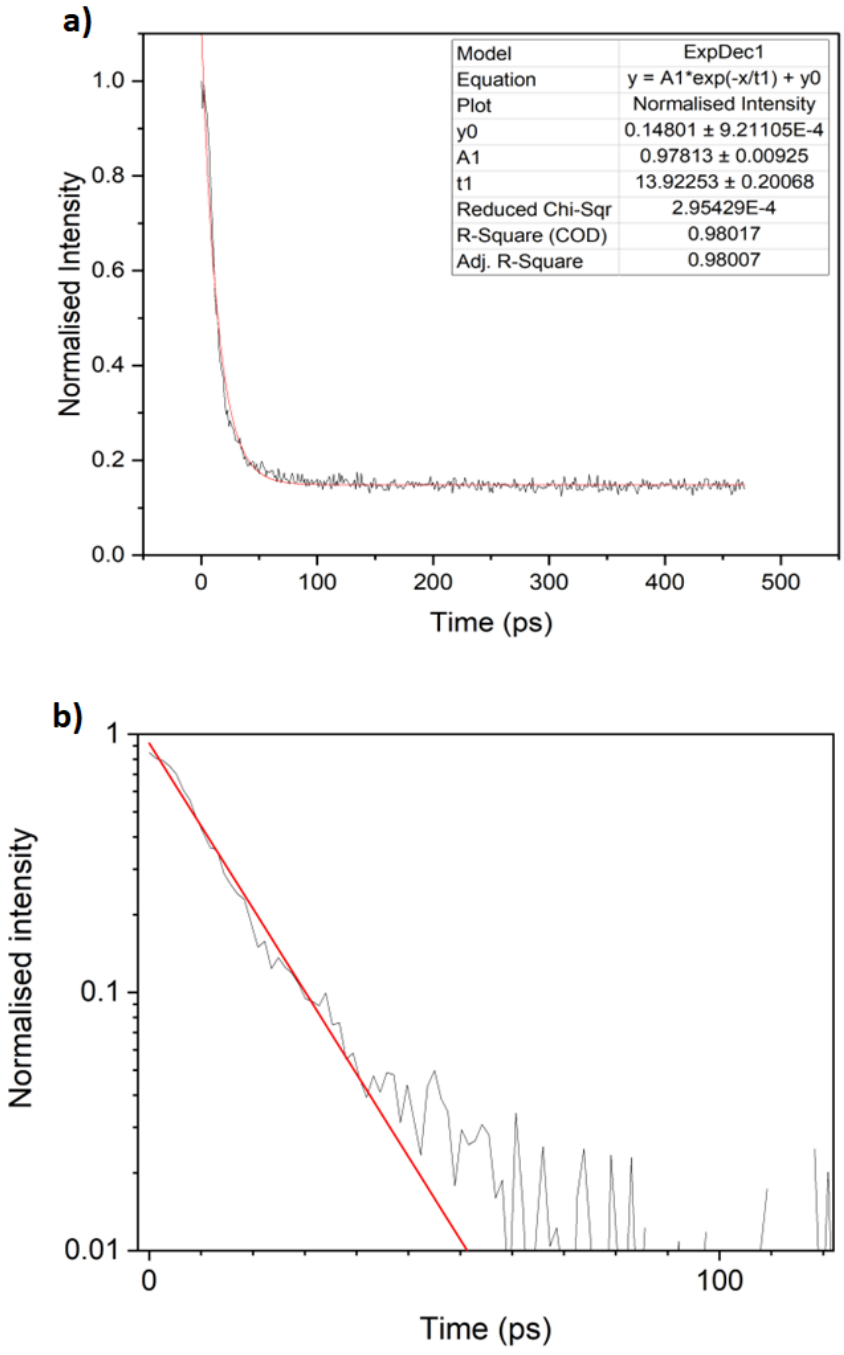

Figure 5.7: *a) The exponential fitting of TRCL decay, b) The exponential decay fitting in logarithmic scale to the streak image in Figure 5.6b (CdTe grain boundary).*

The time-resolved cathodoluminescence results were also collected at the inter-diffusion CdSeTe layer, which has small grains. Figure 5.8 shows the data collected at one of the grain interiors in this layer. The intensity at this layer is lower than the CdTe layer, and the centre of the luminescence peak was at 824 nm with a range from 810 nm to 830 nm. The redshift of the luminescence peak compared to the previous peak position in the CdTe layer was due to the Se alloying. Although these results are collected close to liquid nitrogen temperature,

the high intensity observed is consistent with the room temperature observation of higher panchromatic CL intensity for the CdTe layer compared to the CdSeTe region (Figure 4.21).

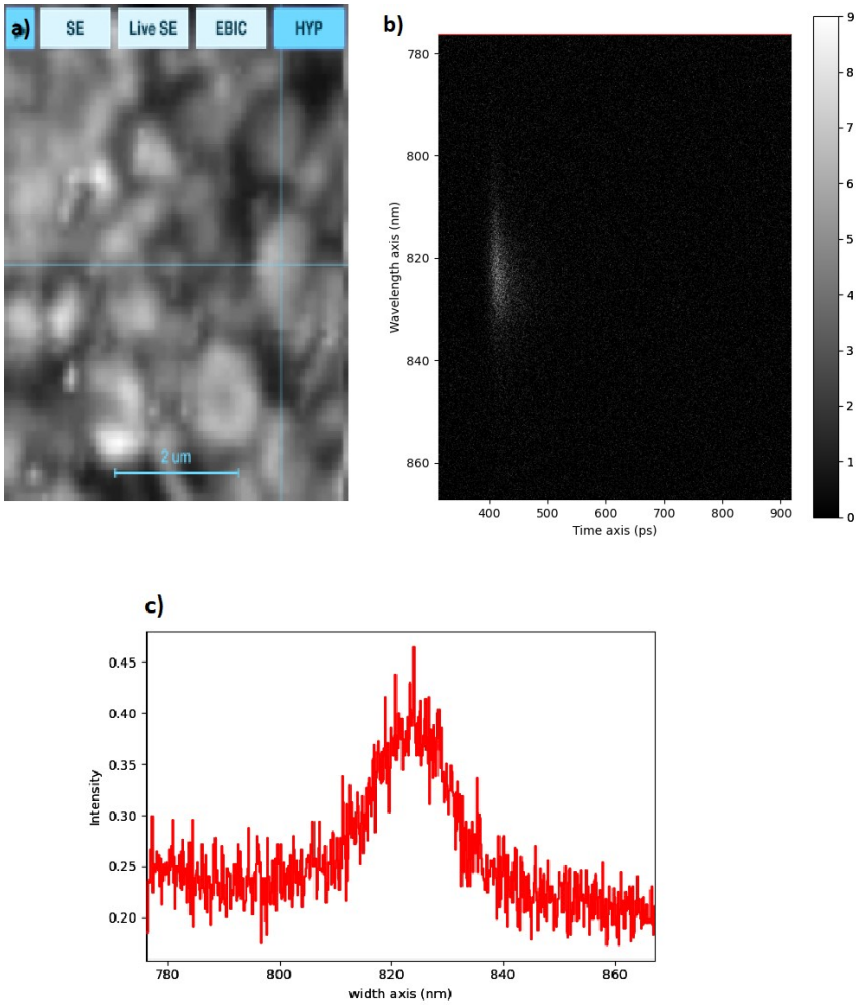

Figure 5.8: *a) Secondary electron image with the electron beam positioned at one of the grain interiors in the inter-diffusion CdSeTe layer, b) Streak camera image as a function of wavelength, c) The time integrated CL spectrum at the grain interior.*

The calculated carrier lifetime for the CdSeTe grain interior was 26.3 ± 0.5 ps as shown in Figure 5.9, which is a longer lifetime than the CdTe layer. At liquid nitrogen temperature, the Cd vacancy A^0 acceptor bound excitonic emission appeared in the steak camera image. The brighter A^0X bound exciton intensity in the CdTe region can be either due to a higher acceptor A^0 concentration in the CdTe layer or due to less non-radiative recombination of the free excitons before they become bound to the A^0 centres. The overall lifetime is governed not just by A^0X recombination, but also by other radiative (e.g. donor-acceptor pair) and non-radiative pathways. Therefore, although there is no increase in the A^0X lifetime in the CdTe layer compared to CdSeTe, we expect the overall lifetime to be longer in the former if

the TRCL measurements were able to detect all luminescence wavelengths.

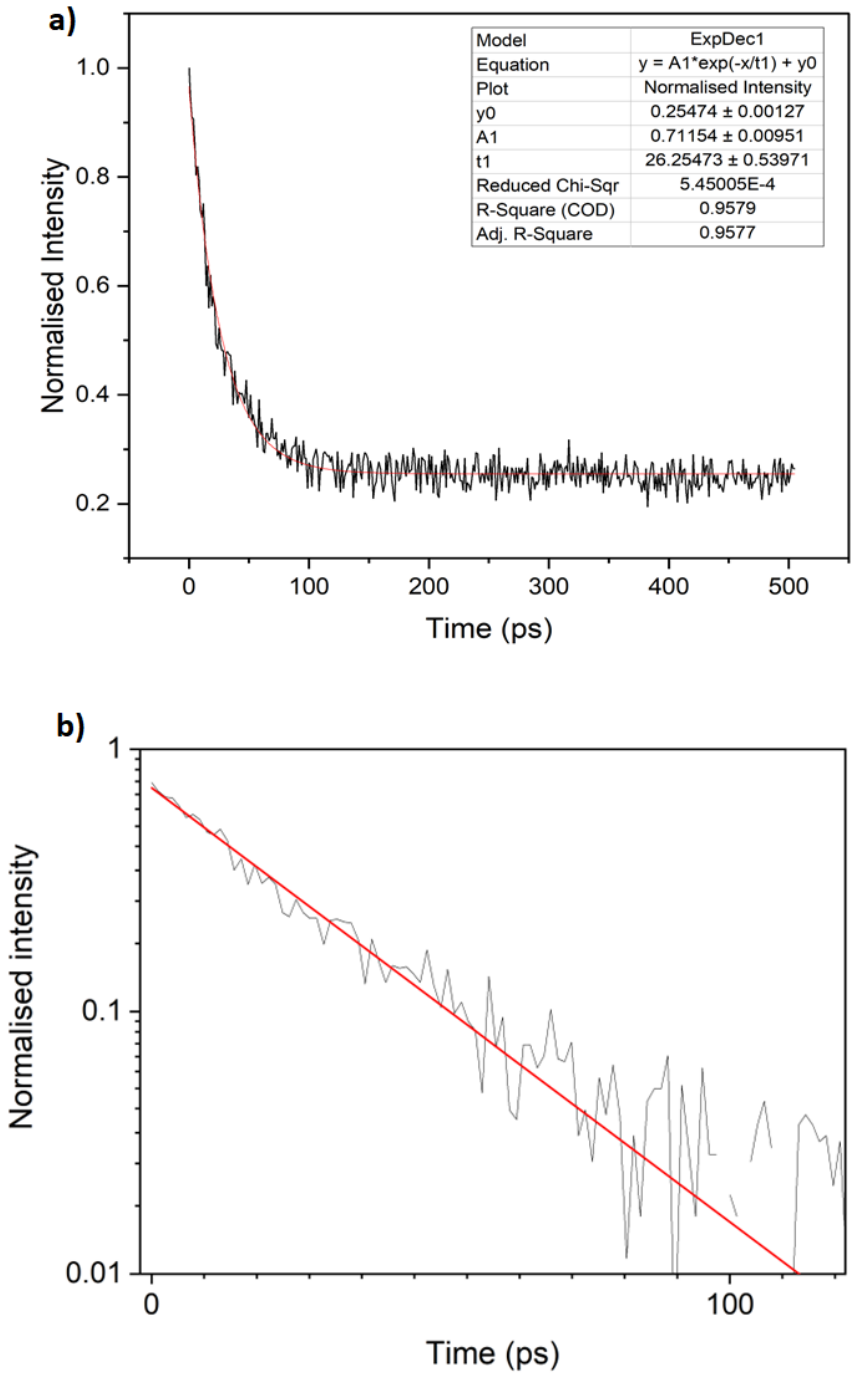

Figure 5.9: *a) The exponential fitting of TRCL decay, b) The exponential decay fitting in logarithmic scale to the streak image in Figure 5.8b (CdSeTe grain interior).*

Another time-resolved cathodoluminescence measurement was acquired at the grain boundary in the same inter-diffusion CdSeTe layer, as shown in Figure 5.10. The estimated carrier lifetime from Figure 5.11 was 24.2 ± 0.4 ps. This is a slightly shorter lifetime than the CdSeTe grain interior, but longer than the CdTe grain boundary lifetime (13.9 ps), suggesting that with Se alloying grain boundaries become more benign to A^0X/ band-to-band recombination.

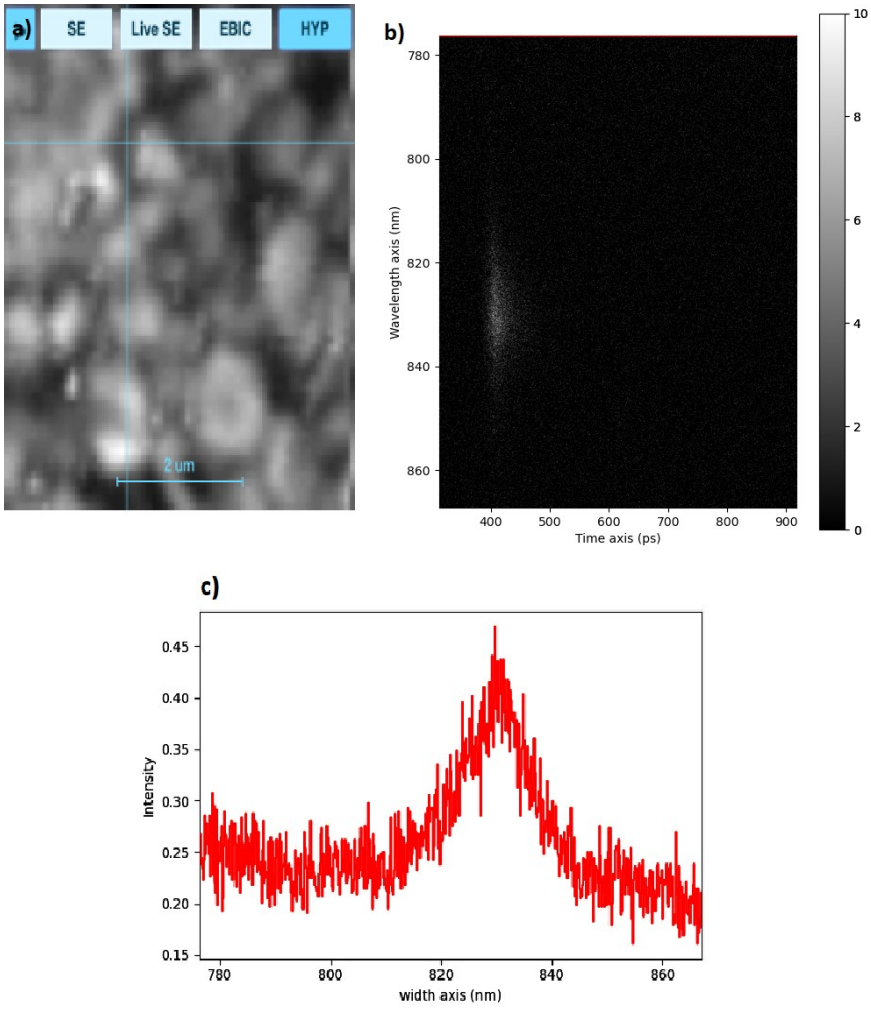

Figure 5.10: *a) Secondary electron image with the electron beam positioned at one of the grain boundaries in the inter-diffusion CdSeTe layer, b) Streak camera image as a function of wavelength, c) The time integrated CL spectrum at the grain boundary.*

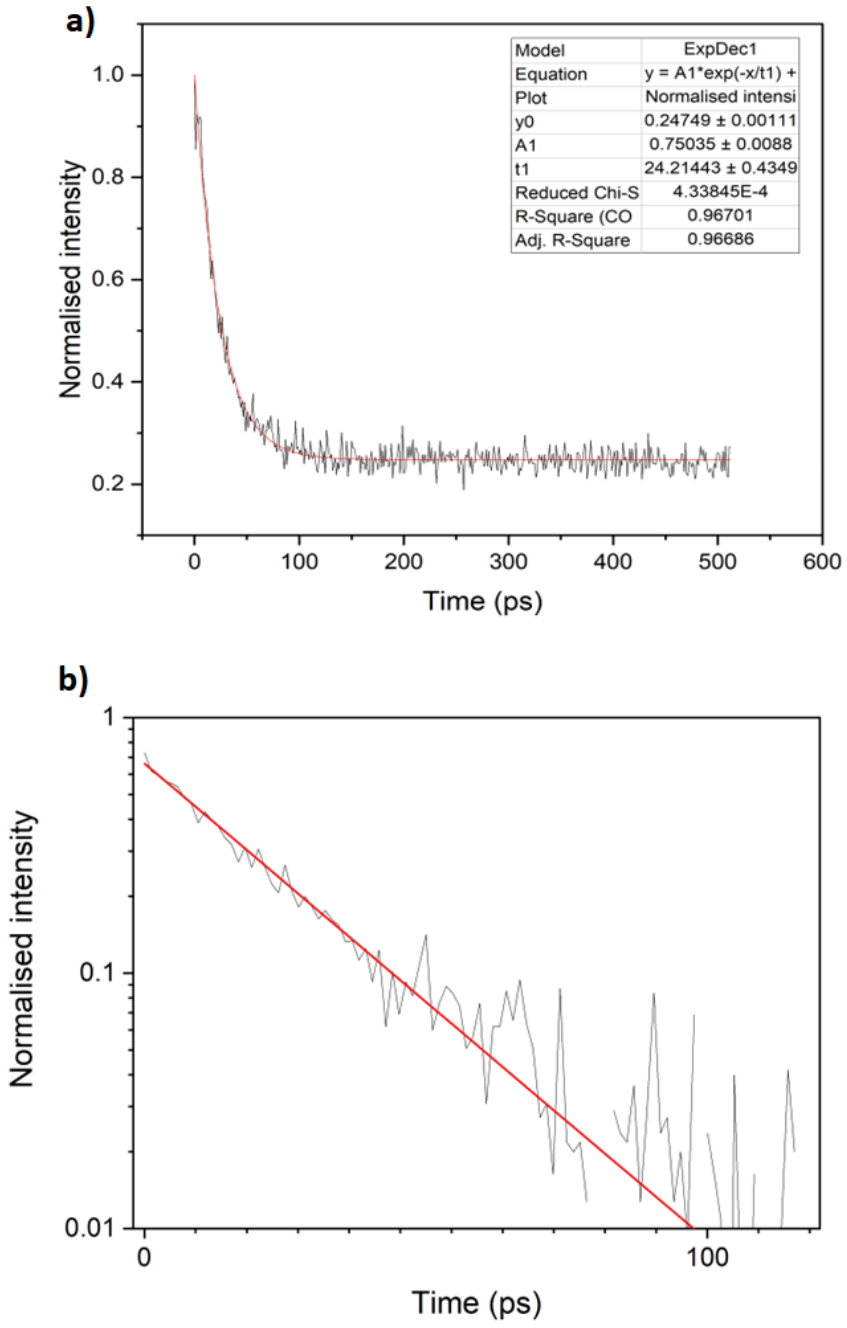

Figure 5.11: *a) The exponential fitting of TRCL decay, b) The exponential decay fitting in logarithmic scale to the streak image in Figure 5.10b (CdSeTe grain boundary).*

Zheng *et al.* [56] used both time-resolved photoluminescence and cathodoluminescence to find that the inter-diffusion CdSeTe layer has a longer lifetime. Ablekim *et al.* [131] recorded a significant increase in carrier lifetime to values exceeding 200 ns in CdSeTe solar cells. This increase in lifetime is achieved by large CdSeTe grains at the interface layer. They suggested several features that lead to this improvement in the carrier lifetime, such as the large CdSeTe

grains at the absorber/emitter interface and grain boundary and intra-grain passivation in the absorber layer. However, in our case because of grain boundary voids and solute drag effect, the grains in the CdSeTe layer could not grow which then led to small grains. The small grains had more grain boundaries area working as non-radiative recombination centres, and this is the reason for the lower panchromatic CL intensity in the CdSeTe layer.

5.4 STEM-EDX analysis of Se diffusion

A diffusion process refers to the phenomenon where particles, such as atoms and molecules spread out and move from regions of higher concentration to regions of lower concentration. For diffusion to occur there needs to be a difference in the concentration of the substance in question between two or more regions. Atoms tend to move from areas of higher concentration to areas of lower concentration, in order to equalise the concentration throughout the system [132]. Fick's Law provides a fundamental mathematical relationship between the rate of diffusion, concentration gradient, and the diffusion coefficient:

$$F = -D\frac{\delta C}{\delta x} \tag{5.4.1}$$

where F represents the rate of diffusion per unit area, C is the concentration of diffusing species at position x, and D is the diffusion coefficient. For an infinitesimally thin surface film the diffusion profile can be shown to be [132]:

$$C(x,t) = \frac{M}{\sqrt{\pi Dt}} \exp \frac{-x^2}{4Dt} \tag{5.4.2}$$

where M is the total amount of substance diffusing, and t is the diffusion time.

The concentration profile of Se from STEM-EDX data has been measured to analyse the Se diffusion. Figure 5.12 shows the EDX line scan that was acquired across the CdSeTe inter-diffusion layer for 400 nm CdSe sample. Cd, Te and Se X-ray counts are shown in Figure 5.13. The Se concentration is high at the CdSe-CdTe interface region and then gradually decreases toward the CdTe layer. The decrease in Se is accompanied by an increase in Te. Furthermore, the diffusion profiles are not smooth; small 'steps' in the X-ray counts are observed as the linescan traverses a grain boundary, signifying that different grains have different Se concentrations. There is also a gradual decrease in the Cd and Te X-ray counts deeper into the CdTe layer. This is likely caused by a non-uniform thickness of the (FIB

prepared) TEM specimen, i.e. thinner regions of the TEM specimen will produce fewer X-rays for a fixed acquisition time.

Figure 5.12: *STEM dark field image showing EDX line scan for 400 CdSe sample.*

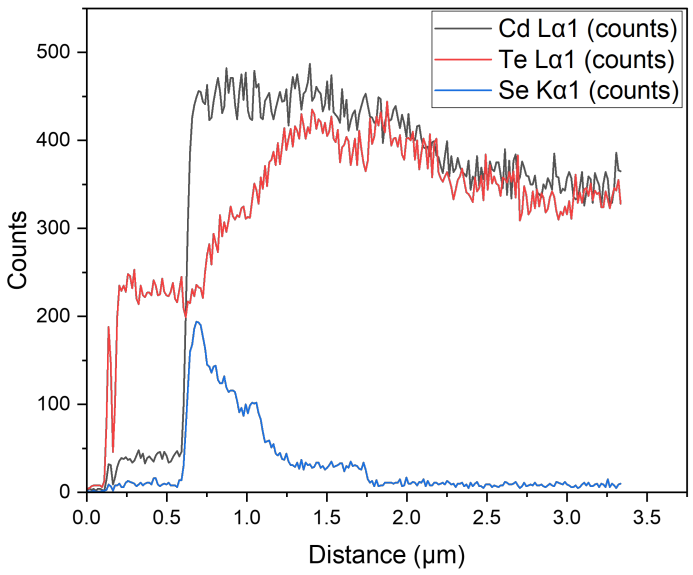

Figure 5.13: *Cd, Te and Se X-ray counts as a function of the distance from the front side of 400 nm CdSe sample.*

In order to study the Se diffusion profile in Figure 5.13, the previous diffusion formula 5.4.2 is linearised to:

$$\ln C = \ln \frac{M}{\sqrt{\pi D t}} - \frac{1}{4Dt} x^2 \tag{5.4.3}$$

where (- $\frac{1}{4Dt}$) is the gradient and ($\ln \frac{M}{\sqrt{\pi Dt}}$) is the intercept.

The EDX data have been corrected for thickness non-uniformity of the TEM specimen by taking the ratio of Se/Cd counts, and binning the data by a factor of 8 in order to have smoother data of the Se diffusion, as shown in Figure 5.14.

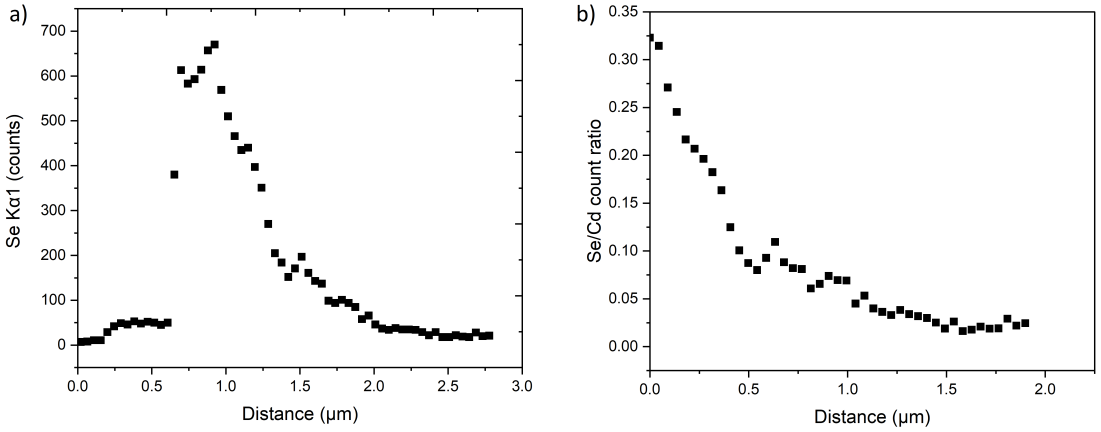

Figure 5.14: *(a) Se X-ray counts as a function of distance from the front side at 8 binning factor, (b) Se/Cd count ratio with origin of the x-axis set to at the onset of Se/Cd ratio decrease.*

Equation (5.4.3) was applied to the STEM EDX data in Figure 5.14b, with 'C' being the Se/Cd EDX count ratio. Figure 5.15 shows the linearised ln(C) vs x^2 plot, which has a gradient of -0.58 μm^2. The calculated diffusion coefficient at 550°C deposition substrate temperature and 10 minutes of deposition time was 7.2×10^{-12} cm^2/s. This result is an order of magnitude smaller than the diffusion coefficient 3.95×10^{-11} cm^2/s that was calculated from the parameterised diffusion coefficients reported in reference [120]. It might be the diffusion in our device is slower due to the pinning and voids across the grain boundaries. Moreover, the Equation 5.4.2 is valid for a single crystal, and our material is polycrystalline, which is likely to result in some error of the diffusion coefficient.

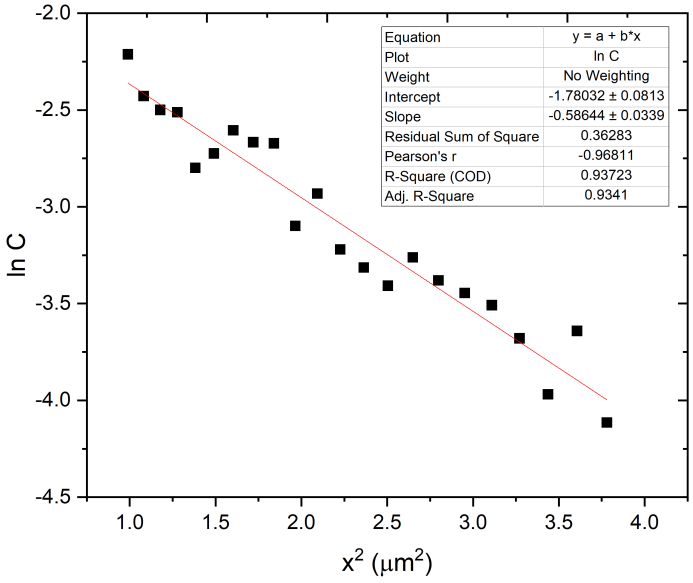

Figure 5.15: *The linear experimental fitting of Se diffusion according to Equation 5.4.3 for 400 nm CdSe sample.*

5.5 CL hyperspectral imaging analysis

CL spectrum imaging across the bevel cross-section at room temperature (300 K) was acquired in order to monitor the Se concentration and band gap variation across the bevel cross-section as shown in Figure 5.16. Figure 5.17 shows the representative CL spectrum acquired from one pixel on the bevel. It shows the band-edge luminescence peak. A wavelength window is selected to calculate the band gap at each individual pixel to the left of the peak position. The intensity for band-to-band luminescence is given by the following formula:

$$I(h\nu) = \sqrt{h\nu - E_g} \quad e^{-}(\frac{h\nu - E_g}{kT}) \tag{5.5.1}$$

where $I(h\nu)$ is the CL intensity at photon energy $(h\nu)$, E_g is the band gap, k is Boltzmann constant, and T is the temperature. A plot of $[\mathrm{I}(h\nu)\exp((h\nu)/kT)]^2$ vs $(h\nu)$ is therefore a straight line. The band gap E_g is equal to the negative of the intercept divided by the gradient. This procedure was used to calculate the band gap at each point in the CL spectrum image.

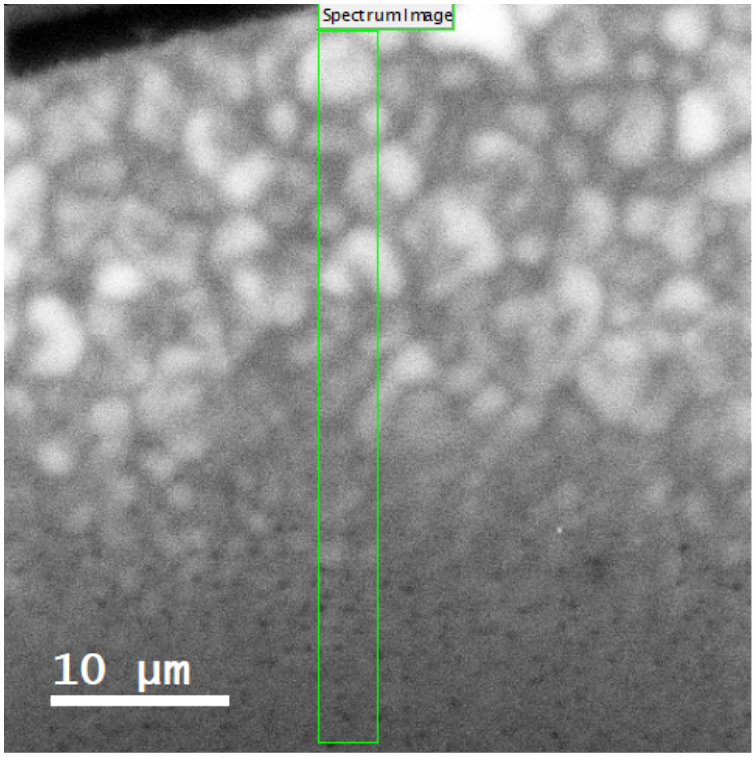

Figure 5.16: *CL panchromatic image showing the spectrum imaging region acquired from the 400 nm CdSe sample.*

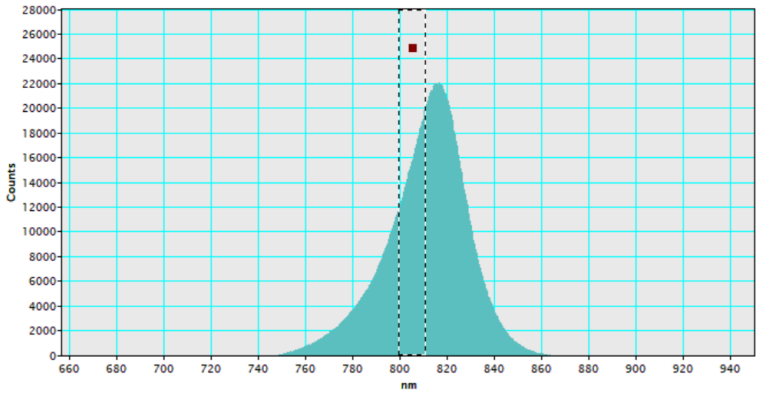

Figure 5.17: *CL spectrum showing wavelength window used for calculating band gap.*

Each pixel in the spectrum image is converted to µm unit of distance, where 1 pixel= 0.250 µm. The distance is multiplied by sin(8°) to correct for the image elongation due to the bevel angle. The plot of the band gap versus the distance across the bevel cross-section is shown in Figure 5.18. The band gap decreased monotonically from the CdTe layer to the CdSeTe inter-diffusion layer as a function of distance. This variation of the band gap with distance across the sample shows how Se alloys the material and affects the optical absorption. At the

top region of the bevel (CdTe layer) the energy gap plateaued around 1.51 eV (i.e. close to the reported band gap of CdTe at 300 K [133]). The band gap decreased further down the bevel towards the CdSeTe inter-diffusion layer till it reached 1.42 eV.

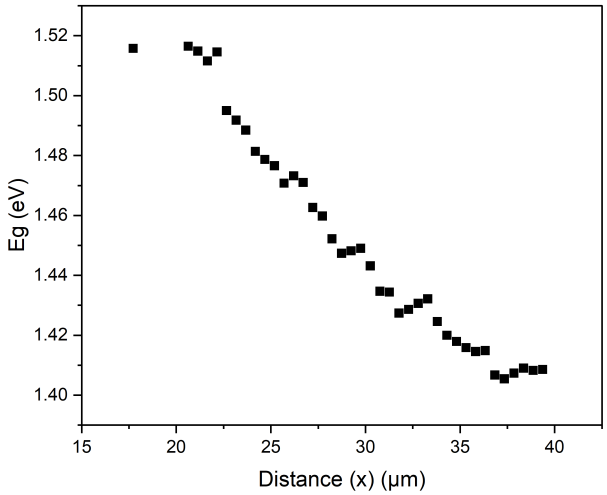

Figure 5.18: *Plot of band gap E_g as a function of distance x along the bevel cross-section from CdTe to CdSeTe layer in 400 nm CdSe sample.*

The band gap energy of CdSe is 1.74 eV [134]. Our measurement did not show this value which indicates that the CdSe layer is completely diffused during annealing to form the CdSeTe inter-diffusion layer. Therefore, the 400 nm CdSe layer is not a large reservoir to provide Se continuously.

Se concentration was then calculated as a function of distance and band gap by using the formula (Equation 5.4.3).

$$E_g(CdSe_XTe_{1-X}) = XE_g(CdSe) + (1-X)E_g(CdTe) - bX(1-X) \tag{5.5.2}$$

where X is the concentration and b is the bowing parameter. The quadratic equation is used to calculate the Se concentration. Our experimental measurement gave 1.51 eV for the CdTe band gap. The CdSe band gap in the literature was 1.74 eV [134] and 0.78 eV was used for the bowing parameter [135]. The plot of the band gap as a function of Se concentration is shown in Figure 5.19; the band gap decreased when CdTe was alloyed with Se which is consistent with Figure 5.18. Figure 5.20 plots the Se concentration profile as function of distance for the bevel cross-section. The plot was derived by applying Equation 5.5.2 to the data in Figure

5.18. The maximum Se concentration in the CdSeTe inter-diffusion layer is X = 0.3. This is again smaller than X = 0.5 for pure CdSe, indicating that the 400 nm CdSe layer has fully dissolved.

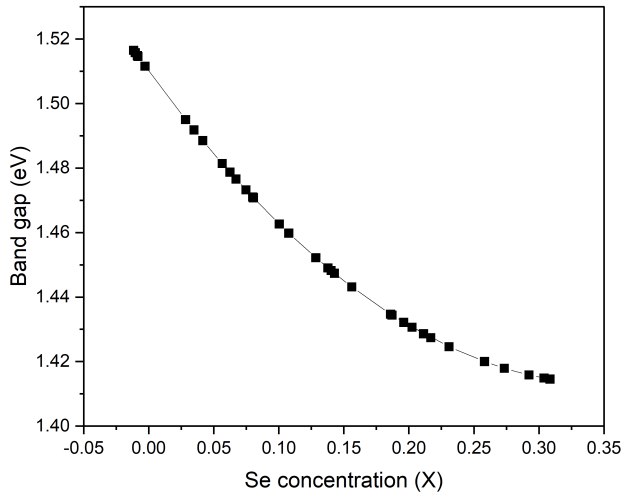

Figure 5.19: *The band gap E_g plot as a function of Se concentration from CdTe to CdSeTe layer in the 400 nm CdSe sample.*

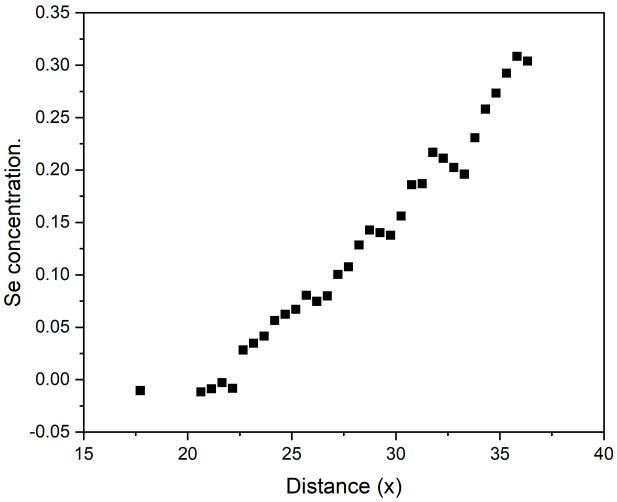

Figure 5.20: *Plot of Se concentration as a function of distance x along the bevel cross-section from CdTe to CdSeTe layer in the 400 nm CdSe sample.*

5.6 Conclusion

In conclusion, the bound exciton/band-to-band peak carrier lifetime of CdTe and CdSeTe inter-diffusion layer for 400 nm CdSe sample was measured using time resolved cathodoluminescence. The results showed higher CL intensity at the CdTe layer, but the measured lifetime at the inter-diffusion CdSeTe was longer than the CdTe layer. The lifetime at grain boundaries was shorter than grain interiors for both layers due to the presence of defects and non-radiative recombination at grain boundaries. Band gap variation across the bevelled cross-section measured using CL spectrum imaging showed that the band gap decreased from 1.51 eV in CdTe layer to 1.42 eV in CdSeTe layer. The Se diffusion coefficient was calculated by STEM-EDX to be 7.2×10^{-12} cm^2/s.

Chapter 6

Summary and future work

6.1 Summary

In this thesis, cadmium telluride-cadmium selenide solar cells were investigated. Two different sets of devices have been used. The first had 100 nm CdSe thickness window layer with 0 torr gas pressure during CdTe close space sublimation (CSS). The second set had a 100 nm and 400 nm CdSe window layer thickness under 5 torr gas pressure during CdTe close space sublimation.

Electron microscopy was carried out to investigate these devices and understand their electrical and optical properties. The samples were imaged using scanning electron microscopy, cathodoluminescence, and also analysed with Electron backscatter diffraction. Furthermore, focused ion beam microscopy was used to prepare the bevel cross-section and thin specimens for transmission electron microscopy. Scanning transmission electron microscopy was used to image grain morphology, characterise crystal structure and was combined with energy dispersive X-ray spectroscopy to measure chemical composition.

In Chapter 3, we combined cathodoluminescence (CL) contrast (optoelectronic properties) and electron backscatter diffraction (crystallographic properties) to investigate the effect of grain boundary misorientation on non-radiative recombination. CL and electron backscatter diffraction (EBSD) correlative investigations of regular and CSL grain boundaries in CdTe-CdSe thin-film have been presented in this chapter. The grain boundaries were assumed to be pure CdTe, as energy dispersive X-ray (EDX) results showed there is no selenium appearing at the back contact surface where the measurements were taken. CL contrast was calculated, and for the regular GBs, the contrast was significantly high in the range between 35°-55° grain boundary misorientation angle. This means that those regular grain boundaries are strong non-radiative recombination centres. The highest CL contrast was observed at 35°, which might indicate this particular misorientation angle is the most harmful to the device. On the other hand low index CSL such as $\Sigma 3$, $\Sigma 5$, $\Sigma 7$ and $\Sigma 9$ showed much lower contrast values which is consistent with the fact that they have high symmetry. The robustness of our results was examined by performing more detailed quantitative analysis of the reduced recombination velocity. The reduced recombination velocity results were consistent with the previous trends, i.e. the high contrast grain boundary has a larger reduced recombination velocity than the lower contrast grain boundary. Our results for the regular grain boundaries had the opposite behaviour reported in Moseley *et al* [60] and this might be due to the contrast calculation being the more accurate analysis rather than the absolute CL intensity used in [60]. The normalised average CL intensity was slightly lower around the range 35°-45°,

while our results showed a high CL contrast in the same misorientation range. Furthermore, Moseley *et al* [60] observed Σ3 CSL had a high intensity which is in agreement with our low contrast values, indicating that the non-radiative recombination is small at Σ3 CSL. However, there was no agreement for other CSLs, with our study reporting low recombination for Σ = 5, 7 and 9 GBs and Moseley et al. reporting recombination rates that were similar to regular GBs. The discrepancy could however be due to the much larger Σ range in Moseley's study ($\Sigma = 5 - 49$). In general, the CL contrast in CdTe-CdSe solar cells varied depending on the type of grain boundary, whether regular grain boundaries or coincidence site lattice grain boundaries. Moreover, Moseley *et al* [60] used automated software to process all the grain boundaries, which is not the case with our work where the grains have been chosen and analysed by hand. Also, they used the absolute CL intensity rather than contrast, which is more susceptible to sample inhomogeneities, such as local doping concentration and porosity.

Chapter 4 presented the second set of devices that have different thicknesses of the CdSe window layer (100 nm and 400 nm). The initial aim of the investigation was to examine if a change in crystal structure could explain the dramatic drop in external quantum efficiency (EQE) for the 400 nm CdSe device. Two devices with different thicknesses 100 nm and 400 nm of CdSe were compared. Both standard and bevel cross-sections were prepared on both samples, and Kirkendall voids were observed in both, although they were more abundant in the 400 nm sample which also had a small grain size in the inter-diffusion region. The 400 nm CdSe sample bevel cross-section showed low cathodoluminescence (CL) intensity at the CdSeTe inter-diffusion region, due to the harmful defects (i.e. grain boundaries, voids) that are causing high carrier non-radiative recombination rates. The CL results reveal that CdSeTe inter-diffusion layer has both small grain size and Kirkendal voids at the grain boundaries. It is proposed that the small grain size is because of the Se solute drag effect on the grain boundaries. The fast speed of Se diffusion also created voids that further pinned the grain boundaries and prevented the grains from growing. The redshift of the CL spectrum at the inter-diffusion layer was observed in both samples, due to Se alloying. EDX mapping in the transmission electron microscope (TEM) across the inter-diffusion layer showed Se diffused more uniformly in the 100 nm CdSe sample compared to 400 nm CdSe. Zinc blende cubic structure observed in our TEM diffraction patterns indicates that the high recombination rate at the inter-diffusion layer is not because of the hexagonal wurtzite structure as previously reported in the literature [54]. Therefore, our investigations in Chapter 4 using bevel cross-section cathodoluminescence and transmission electron microscopy showed the rapid diffusion of Se along the CdTe grain boundaries led to solute pinning and small absorber CdSeTe layer

grains close to the pn-junction. Kirkendall voiding at the grain boundaries was also observed. Together these two effects explain the EQE decrease in these devices.

In Chapter 5 Se diffusion from CdSe layer to CdTe layer has been investigated further to better understand the reason behind the low EQE for the 400 nm CdSe sample. Time-resolved cathodoluminescence (TRCL) technique was used to measure the carrier lifetime on the bevel of 400 nm sample for both CdTe and CdSeTe layers, to understand how fast the charge carriers recombine within each layer. Bound exciton (A^0X)/ band-to-band recombination peak was observed in both layers, with a redshift from CdTe layer to CdSeTe because of Se alloying. The A^0X peak intensity is higher in the CdTe layer than the CdSeTe inter-diffusion layer. Least squares fitting was used to fit the luminescence decay curve and extract the A^0X carrier lifetime at CdTe and CdSeTe layers. The TRCL decay at the CdSeTe inter-diffusion layer was slower than CdTe layer. A small difference was observed in the A^0X lifetime value between the grain boundary and grain interior within each layer. The carrier lifetime was lower at the grain boundary compared to the grain interior because of more defects at the grain boundary. The longer A^0X lifetime in our TRCL measurement for the CdSeTe layer is not consistent with the lower panchromatic CL intensity observed in this region compared to CdTe. It is important however to note that the A^0X lifetime in TRCL is not the same as the overall carrier lifetime, because other radiative mechanisms, such as the donor-acceptor pair, could not be measured due to the limited sensitivity of the streak camera. Moreover, scanning TEM (STEM)-EDX results were also presented in Chapter 5 to measure the Se diffusion coefficient. A Se diffusion coefficient of 7.2×10^{-12} cm^2/s has been calculated using STEM-EDX concentration profile (X-ray counts) at 550 °C and 10 minutes of deposition time. This value is an order of magnitude smaller than the literature values reported in [120]. The band gap and Se diffusion profile were also measured using CL spectrum imaging data acquired over the bevel cross-section. The band gap at each pixel of the bevel cross-section is calculated from the shape of the band edge luminescence peak. The band gap decreased from the bulk CdTe value (1.51 eV) to 1.42 eV within the CdSeTe inter-diffusion layer. The results indicated that the CdSe layer had completely dissolved during inter-diffusion.

6.2 Future Work

There are some avenues which could be explored with regard to future work. For example, to better understand the solute drag effect in CdTe solar cells, molecular dynamics simulations could potentially be performed to model Se grain boundary interactions and compare them

with our experimental results [123]. It would be also valuable to measure the lattice mismatch and strain profile for the 400 nm CdSe sample for a better understanding of how Se diffusion affects the device efficiency through strain and Shockley-Read-Hall recombination. Similarly, the Se diffusion profile can also be used to construct the band bending and local electric fields through the absorber layer and determine its effect of carrier collection. Additional further work using time resolved photoluminescence could be done in measuring the overall carrier lifetime at both the CdTe and CdSeTe regions in the 400 nm CdSe device, in order to see if the overall lifetime is longer in the CdTe region.

Bibliography

[1] Climate change: Global temperature. https://www.climate.gov/news-features/understanding-climate/climate-change-global-temperature. Accessed: 2023-01-01.

[2] Global temperature anomalies. https://svs.gsfc.nasa.gov/4964. Accessed: 2023-01-08.

[3] January 2023 global climate report. https://www.ncei.noaa.gov/access/monitoring/monthly-report/global/202301. Accessed: 2023-11-02.

[4] I. M. Dharmadasa. *Advances in thin-film solar cells*. Jenny Stanford Publishing, 2018.

[5] J. Twidell. *Renewable energy resources*. Routledge, 2021.

[6] G. M. Wilson, M. Al-Jassim, W. K. Metzger, S. W. Glunz, P. Verlinden, G. Xiong, L. M. Mansfield, B. J. Stanbery, K. Zhu, and Y. Yan. The 2020 photovoltaic technologies roadmap. *Journal of Physics D: Applied Physics*, 53(49):493001, 2020.

[7] R. Cariou, J. Benick, F. Feldmann, O. Höhn, H. Hauser, P. Beutel, N. Razek, M. Wimplinger, B. Bläsi, and D. Lackner. III-V-on-silicon solar cells reaching 33% photoconversion efficiency in two-terminal configuration. *Nature Energy*, 3(4):326–333, 2018.

[8] T. Zhang, M. Wang, and H. Yang. A review of the energy performance and life-cycle assessment of building-integrated photovoltaic (BIPV) systems. *Energies*, 11(11):3157, 2018.

[9] M. Green, E. Dunlop, J. Hohl-Ebinger, M. Yoshita, N. Kopidakis, and X. Hao. Solar cell efficiency tables (version 57). *Progress in photovoltaics: research and applications*, 29(1):3–15, 2021.

[10] M. Dhankhar, O. P. Singh, and V.N. Singh. Physical principles of losses in thin film solar cells and efficiency enhancement methods. *Renewable and Sustainable Energy Reviews*, 40:214–223, 2014.

[11] J. Britt and C. Ferekides. Thin-film CdS/CdTe solar cell with 15.8% efficiency. *Applied physics letters*, 62(22):2851–2852, 1993.

[12] X. Wu. High-efficiency polycrystalline CdTe thin-film solar cells. *Solar energy*, 77(6):803–814, 2004.

[13] T. Baines, G. Zoppi, L. Bowen, T. P. Shalvey, S. Mariotti, K. Durose, and J. D. Major. Incorporation of CdSe layers into CdTe thin film solar cells. *Solar Energy Materials and Solar Cells*, 180:196–204, 2018.

[14] D. Abou Ras, S. Wagner, B. J. Stanbery, H. Schock, R. Scheer, L. Stolt, S. Siebentritt, D. Lincot, C. Eberspacher, and K. Kushiya. Innovation highway: Breakthrough milestones and key developments in chalcopyrite photovoltaics from a retrospective viewpoint. *Thin Solid Films*, 633:2–12, 2017.

[15] T. Feurer, B. Bissig, T. P. Weiss, R. Carron, E. Avancini, J. Löckinger, S. Buecheler, and A. N. Tiwari. Single-graded CIGS with narrow bandgap for tandem solar cells. *Science and Technology of advanced MaTerialS*, 19(1):263–270, 2018.

[16] K. H. Ong, R. Agileswari, B. Maniscalco, P. Arnou, C. C. Kumar, J. W. Bowers, and M. B. Marsadek. Review on substrate and molybdenum back contact in CIGS thin film solar cell. *International Journal of Photoenergy*, 2018, 2018.

[17] A. H. Pinto, S. W. Shin, E. S. Aydil, and R. L. Penn. Selective removal of $Cu_{2-x}(S,Se) phases from Cu_2ZnSn(S,Se)_4 thin films$. $Green Chemistry, 18(21) : 5814 - -5821, 2016$.

[18] M. F. Islam, N. M. Yatim, and M. A. Hashim. A review of CZTS thin film solar cell technology. *Journal of Advanced Research in Fluid Mechanics and Thermal Sciences*, 81(1):73–87, 2021.

[19] W. Shockley and H. J. Queisser. Detailed balance limit of efficiency of p-n junction solar cells. *Journal of applied physics*, 32(3):510–519, 1961.

[20] S. Rühle. Tabulated values of the shockley–queisser limit for single junction solar cells. *Solar energy*, 130:139–147, 2016.

[21] M. Iqbal. *An introduction to solar radiation*. Elsevier, 2012.

[22] M. Grundmann. *Physics of semiconductors*, volume 11. Springer, 2010.

[23] S. M. Sze. *Semiconductor devices: physics and technology*. John wiley & sons, 2008.

[24] U. Wijesinghe, G. Longo, and O. S. Hutter. Defect engineering in antimony selenide thin film solar cells. *Energy Advances*, 2023.

[25] G. W. Crabtree and N. S. Lewis. Solar energy conversion. In *AIP Conference Proceedings*, volume 1044, pages 309–321. American Institute of Physics, 2008.

[26] M. A. Cavalcante, A. Bonizzia, and L. C. Gomes. Data acquisition in the physics laboratory: an easy, simple and low-cost method for experiments in mechanics. *Revista Brasileira de Ensino de Fisica*, 30:2501–1, 2008.

[27] A. Kitai. *Principles of Solar Cells, LEDs and Diodes: The role of the PN junction*. John Wiley & Sons, 2011.

[28] A. Smets, K. Jäger, O. Isabella, R. Swaaij, and M. Zeman. *Solar Energy: The physics and engineering of photovoltaic conversion, technologies and systems*. UIT Cambridge, 2015.

[29] I. Yahyaoui. *Advances in renewable energies and power technologies: volume 1: solar and wind energies*. Elsevier, 2018.

[30] D. Kiermasch, L. Gil-Escrig, H. J. Bolink, and K. Tvingstedt. Effects of masking on open-circuit voltage and fill factor in solar cells. *Joule*, 3(1):16–26, 2019.

[31] J. Poortmans and V. Arkhipov. *Thin film solar cells: fabrication, characterization and applications*, volume 18. John Wiley & Sons, 2006.

[32] T. D. Lee and A. U. Ebong. A review of thin film solar cell technologies and challenges. *Renewable and Sustainable Energy Reviews*, 70:1286–1297, 2017.

[33] K. W. Böer. *Handbook of the physics of thin-film solar cells*. Springer Science & Business, 2014.

[34] L. Kranz, C. Gretener, J. Perrenoud, R. Schmitt, F. Pianezzi, F. La Mattina, P. Blösch, E. Cheah, A. Chirilă, and C. M. Fella. Doping of polycrystalline CdTe for high-efficiency solar cells on flexible metal foil. *Nature communications*, 4(1):1–7, 2013.

[35] A.D. Compaan, A. Gupta, S. Lee, S. Wang, and J. Drayton. High efficiency, magnetron sputtered CdS/CdTe solar cells. *Solar Energy*, 77(6):815–822, 2004.

[36] W.A. Pinheiro, V.D. Falcão, L.R.O. Cruz, and C.L. Ferreira. Comparative study of CdTe sources used for deposition of CdTe thin films by close spaced sublimation technique. *Materials Research*, 9:47–49, 2006.

[37] G. Gordillo, J.M. Florez, and L.C. Hernandez. Preparation and characterization of CdTe thin films deposited by CSS. *Solar Energy Materials and Solar Cells*, 37(3-4):273–281, 1995.

[38] C. Doroody, K.S. Rahman, S.F. Abdullah, M.N. Harif, H.N. Rosly, S.K. Tiong, and N. Amin. Temperature difference in close-spaced sublimation (CSS) growth of CdTe thin film on ultra-thin glass substrate. *Results in Physics*, 18:103213, 2020.

[39] I. Kaur, Y. Mishin, and W. Gust. *Fundamentals of grain and interphase boundary diffusion.* John Wiley, 1995.

[40] A. Reinders, P. Verlinden, W. Van Sark, and A. Freundlich. *Photovoltaic solar energy: from fundamentals to applications.* John Wiley & Sons, 2017.

[41] V. Randle. *The role of the coincidence site lattice in grain boundary engineering.* Number 659. Maney Pub, 1996.

[42] L. A. Mora. *2D and 3D grain growth modeling and simulation.* Cuvillier Verlag, 2008.

[43] D. A. Porter. KE easterling phase transformations in metals and alloys, 1992.

[44] K. Wang, W. Zhang, J. Xu, and W. Dan. The impact of misorientation on the grain boundary energy in bi-crystal copper: an atomistic simulation study. *Journal of Molecular Modeling*, 28(2):47, 2022.

[45] L. Priester. *Grain boundaries: from theory to engineering*, volume 172. Springer Science & Business Media, 2012.

[46] D. B. Holt and B. G. Yacobi. *Extended defects in semiconductors: electronic properties, device effects and structures.* Cambridge University Press, 2007.

[47] K. Durose and G.J. Russell. Twinning in CdTe. *Journal of crystal growth*, 101(1-4):246–250, 1990.

[48] T. A. Fiducia, B. G. Mendis, K. Li, C. R. M. Grovenor, A. H. Munshi, K. Barth, W. S. Sampath, L. D. Wright, A. Abbas, and J. W. Bowers. Understanding the role of selenium in defect passivation for highly efficient selenium-alloyed cadmium telluride solar cells. *Nature Energy*, 4(6):504–511, 2019.

[49] J. D. Major, M. Al Turkestani, L. Bowen, M. Brossard, C. Li, P. Lagoudakis, S. J. Pennycook, L.J. Phillips, R.E. Treharne, and K. Durose. In-depth analysis of chloride treatments for thin-film CdTe solar cells. *Nature communications*, 7(1):13231, 2016.

[50] J. D. Major. Grain boundaries in CdTe thin film solar cells: a review. *Semiconductor Science and Technology*, 31(9):093001, 2016.

[51] D. Mao, C.E. Wickersham, and M. Gloeckler. Measurement of chlorine concentrations at CdTe grain boundaries. *IEEE Journal of Photovoltaics*, 4(6):1655–1658, 2014.

[52] A. Abbas, D. Swanson, A. Munshi, K. Barth, W. S. Sampath, G.D. West, J. W. Bowers, P. M. Kaminski, and J.M. Walls. The effect of a post-activation annealing treatment on thin film CdTe device performance. In *2015 IEEE 42nd Photovoltaic Specialist Conference (PVSC)*, pages 1–6. IEEE, 2015.

[53] A. H. Munshi, J. Kephart, A. Abbas, J. Raguse, J. Beaudry, K. Barth, J. Sites, J. Walls, and W. Sampath. Polycrystalline CdSeTe/CdTe absorber cells with 28 ma/cm 2 short-circuit current. *IEEE Journal of Photovoltaics*, 8(1):310–314, 2017.

[54] J. D. Poplawsky, W. Guo, N. Paudel, A. Ng, K. More, D. Leonard, and Y. Yan. Structural and compositional dependence of the $CdTe_xSe_{1-x}$ alloy layer photoactivity in CdTe-based solar cells. *Nature communications*, 7(1):1–10, 2016.

[55] N. R. Paudel and Y. Yan. Enhancing the photo-currents of CdTe thin-film solar cells in both short and long wavelength regions. *Applied Physics Letters*, 105(18):183510, 2014.

[56] X. Zheng, D. Kuciauskas, J. Moseley, E. Colegrove, D. S. Albin, H. Moutinho, J. N. Duenow, T. Ablekim, S. P. Harvey, and A. Ferguson. Recombination and bandgap engineering in CdSeTe/CdTe solar cells. *APL Materials*, 7(7):071112, 2019.

[57] T. Shimpi, C. Reich, A. Danielson, A. Munshi, A. Kindvall, R. Pandey, K. Barth, and W. Sampath. Influence of process parameters and absorber thickness on efficiency of polycrystalline CdSeTe/CdTe thin film solar cells. In *2020 47th IEEE Photovoltaic Specialists Conference (PVSC)*, pages 1933–1935. IEEE, 2020.

[58] D. Abou Ras, S. Schorr, and H. W. Schock. Grain-size distributions and grain boundaries of chalcopyrite-type thin films. *Journal of Applied Crystallography*, 40(5):841–848, 2007.

[59] C. Tong and K. P. McKenna. Passivating grain boundaries in polycrystalline CdTe. *The Journal of Physical Chemistry C*, 123(39):23882–23889, 2019.

[60] J. Moseley, W. K. Metzger, H. R. Moutinho, N. Paudel, H. L. Guthrey, Y. Yan, R. K. Ahrenkiel, and M. Al-Jassim. Recombination by grain-boundary type in CdTe. *Journal of Applied Physics*, 118(2):025702, 2015.

[61] A. Ul-Hamid. *A beginners' guide to scanning electron microscopy*, volume 1. Springer, 2018.

[62] L. Qiu. Scanning electron microscope. *Shanghai Measurement and Testing*, 2003.

[63] D. E. Wolf. The optics of microscope image formation. *Methods in cell biology*, 81:11–42, 2007.

[64] W. Zhou and Z. L. Wang. *Scanning microscopy for nanotechnology: techniques and applications*. Springer Science & Business Media, 2007.

[65] J. I. Goldstein, D. E. Newbury, J. R. Michael, N. W. Ritchie, J. H. Scott, and D. C. Joy. *Scanning electron microscopy and X-ray microanalysis*. Springer, 2017.

[66] L. Reimer. *Transmission electron microscopy: physics of image formation and microanalysis*, volume 36. Springer, 2013.

[67] Electron microscopy. `https://engineering.case.edu/research/centers/swagelok-surface-analysis-materials/image-analysis/electron-microscopy`. Accessed: 2023-01-19.

[68] O. de Oliveira Jr, L. Ferreira, G. Marystela, F. de Lima Leite, and A. L. Da Róz. *Nanocharacterization techniques*. William Andrew, 2017.

[69] E. D. Jones. Forensic investigation of stamped markings using a large-chamber scanning electron microscope and computer analysis for depth determination. 2013.

[70] B. G. Yacobi and D. B. Holt. *Cathodoluminescence microscopy of inorganic solids*. Springer Science & Business Media, 2013.

[71] D. Misell and C. Stolinski. Scanning electron microscopy and X-ray microanalysis. a text for biologists, material scientists and geologists, plenum press, New York and London, 1981. XIII+ 673 pp., 1983.

[72] I. Pelant and J. Valenta. *Luminescence spectroscopy of semiconductors*. OUP Oxford, 2012.

[73] S. J. Bauman, Q. Yan, M. Benamara, and J. B. Herzog. Plasmonic nanogap structures studied via cathodoluminescence imaging. In *Plasmonics: Design, Materials, Fabrication, Characterization, and Applications XV*, volume 10346, pages 6–11. SPIE, 2017.

[74] G. P. Agrawal and N. K. Dutta. Recombination mechanisms in semiconductors. In *Semiconductor Lasers*, pages 74–146. Springer, 1993.

[75] P. T. Landsberg. *Recombination in semiconductors*. Cambridge University Press, 2003.

[76] J. Lee, N. C. Giles, D. Rajavel, and C. J. Summers. Room-temperature band-edge photoluminescence from cadmium telluride. *Physical Review B*, 49(3):1668, 1994.

[77] V. Consonni, G. Feuillet, and S. Renet. Spectroscopic analysis of defects in chlorine doped polycrystalline CdTe. *Journal of applied physics*, 99(5):053502, 2006.

[78] B.G. Mendis, D. Gachet, J.D. Major, and K. Durose. Long lifetime hole traps at grain boundaries in CdTe thin-film photovoltaics. *Physical review letters*, 115(21):218701, 2015.

[79] A. A. Taylor, J. D. Major, G. Kartopu, D. Lamb, J. Duenow, R. G. Dhere, X. Maeder, S. J. Irvine, K. Durose, and B. G. Mendis. A comparative study of microstructural stability and sulphur diffusion in CdS/CdTe photovoltaic devices. *Solar Energy Materials and Solar Cells*, 141:341–349, 2015.

[80] J. Moseley, M. Al-Jassim, D. Kuciauskas, H. R. Moutinho, N. Paudel, H. L. Guthrey, Y. Yan, W. K. Metzger, and R. K. Ahrenkiel. Cathodoluminescence analysis of grain boundaries and grain interiors in thin-film CdTe. *IEEE Journal of Photovoltaics*, 4(6):1671–1679, 2014.

[81] J. Moseley, M. Al-Jassim, H. L. Guthrey, J. M. Burst, J. N. Duenow, R. K. Ahrenkiel, and W. K. Metzger. Cathodoluminescence spectrum imaging analysis of CdTe thin-film bevels. *Journal of Applied Physics*, 120(10):105704, 2016.

[82] T. Biduad, J. Moseley, M. Amarasinghe, M. Al-Jassim, W. K. Metzger, and S. Collin. Imaging $CdCl_2$ defect passivation and formation in polycrystalline CdTe films by cathodoluminescence. *Physical Review Materials*, 5(6):064601, 2021.

[83] M. N. Alam, M. Blackman, and D. W. Pashley. High-angle kikuchi patterns. *Proceedings of the Royal Society of London. Series A. Mathematical and Physical Sciences*, 221(1145):224–242, 1954.

[84] J. A. Venables and C. J. Harland. Electron back-scattering patterns—a new technique for obtaining crystallographic information in the scanning electron microscope. *Philosophical Magazine*, 27(5):1193–1200, 1973.

[85] M. Gintalas and P. E. Rivera-Diaz-del Castillo. Advanced electron microscopy: Progress and application of electron backscatter diffraction. 2022.

[86] A. Winkelmann, C. Trager-Cowan, F. Sweeney, A. P. Day, and P. Parbrook. Many-beam dynamical simulation of electron backscatter diffraction patterns. *Ultramicroscopy*, 107(4-5):414–421, 2007.

[87] A. J. Schwartz, M. Kumar, B. L. Adams, and D. P. Field. *Electron backscatter diffraction in materials science*, volume 2. Springer, 2009.

[88] A. Kelly and K. M. Knowles. *Crystallography and crystal defects*. John Wiley & Sons, 2020.

[89] E. J. Whittaker and C. A. Taylor. *The stereographic projection*. University College Cardiff Press, 1984.

[90] M. Sezen and M. Janecek. Focused ion beams (FIB)—novel methodologies and recent applications for multidisciplinary sciences. *Modern Electron Microscopy in Physical and Life Sciences*, pages 121–140, 2016.

[91] L. A. Giannuzzi. *Introduction to focused ion beams: instrumentation, theory, techniques and practice*. Springer Science & Business Media, 2004.

[92] Focused ion beams: An overview of the technology and its capabilities. `https://analyticalscience.wiley.com/do/10.1002/was.00070009/l`. Accessed: 2023-02-10.

[93] L. Holzer, B. Muench, M. Wegmann, P. Gasser, and R. J. Flatt. FIB-nanotomography of particulate systems—part I: Particle shape and topology of interfaces. *Journal of the American ceramic society*, 89(8):2577–2585, 2006.

[94] H. Ma, K. Shieh, and T. X. Qiao. Study of transmission electron microscopy (tem) and scanning electron microscopy (sem). *Nat. Sci*, 4(3):14–22, 2006.

[95] C. F. Sierra. Fundamentals of transmission electron microscopy, the technique with the best resolution in the world. *screen*, 9:10, 2019.

[96] N. Marturi. *Vision and visual servoing for nanomanipulation and nanocharacterization in scanning electron microscope.* PhD thesis, Université de Franche-Comté, 2013.

[97] D. Shindo and H. Kenji. *High-resolution electron microscopy for materials science.* Springer Science & Business Media, 2012.

[98] D. Biró and P. Barna. Fulleren-like structure of nanocrystalline MoS_2 tribological coatings prepared with composition modulated interfaces. 07 2007.

[99] F. Phillipp. Transmission electron microscopy of optoelectronic materials–basics and advanced techniques. In *CEPHONA WORKSHOP ON MICROSCOPY CHARACTERIZATION OF MATERIALS AND STRUCTURES FOR PHOTONICS. Heisenbergstr, Stuttgart, Germany*, 2003.

[100] B. J. Inkson. Scanning electron microscopy (SEM) and transmission electron microscopy (TEM) for materials characterization. In *Materials characterization using nondestructive evaluation (NDE) methods*, pages 17–43. Elsevier, 2016.

[101] B. Waugh, S. G. Wolf, D. Fass, E. Branlund, Z. Kam, J. W. Sedat, and M. Elbaum. Three-dimensional deconvolution processing for STEM cryotomography. *Proceedings of the National Academy of Sciences*, 117(44):27374–27380, 2020.

[102] Z. Li. Scanning transmission electron microscopy studies of mono-and bimetallic nanoclusters. In *Frontiers of Nanoscience*, volume 3, pages 213–247. Elsevier, 2012.

[103] R. Keyse. *Introduction to scanning transmission electron microscopy.* Routledge, 2018.

[104] M. Elbaum, S. Seifer, L. Houben, S. G. Wolf, and P. Rez. Toward compositional contrast by cryo-STEM. *Accounts of chemical research*, 54(19):3621–3631, 2021.

[105] C. Kittel and P. McEuen. *Introduction to solid state physics.* John Wiley & Sons, 2018.

[106] B. Fultz and J. M. Howe. *Transmission electron microscopy and diffractometry of materials*. Springer Science & Business Media, 2012.

[107] S. J. Pennycook. Transmission electron microscopy: A textbook for materials science, williams david b and carter c barry. springer, new york, 2009, 932 pages. isbn 978-0-387-76500-6 (hardcover), isbn 978-0-387-76502-0 (softcover), 2010.

[108] H. A. Mohamed. Dependence of efficiency of thin-film cds/cdte solar cell on optical and recombination losses. *Journal of applied Physics*, 113(9):093105, 2013.

[109] L. Calvo Barrio and G. Vargas. Photoelectron spectroscopy for surface analysis: X-ray and UV excitation. *Capítol del llibre: Handbook of instrumental techniques for materials, chemical and biosciences research*, 2012.

[110] D. Abou-Ras, T. Kirchartz, and U. Rau. *Advanced characterization techniques for thin film solar cells*, volume 2. Wiley Online Library, 2011.

[111] J. D. Major, L. Bowen, and K. Durose. Focussed ion beam and field emission gun-scanning electron microscopy for the investigation of voiding and interface phenomena in thin-film solar cells. *Progress in Photovoltaics: Research and Applications*, 20(7):892–898, 2012.

[112] A. Romeo and E. Artegiani. CdTe-based thin film solar cells: past, present and future. *Energies*, 14(6):1684, 2021.

[113] B. G. Mendis, L. Bowen, and Q. Z. Jiang. A contactless method for measuring the recombination velocity of an individual grain boundary in thin-film photovoltaics. *Applied Physics Letters*, 97(9), 2010.

[114] C. F. Sanz-Navarro, S. F. Lee, S. S. Yap, C. H. Nee, and S. L. Yap. Electrochemical stability and corrosion mechanism of fluorine-doped tin oxide film under cathodic polarization in near neutral electrolyte. *Thin Solid Films*, 768:139697, 2023.

[115] J. D. Major, Y. Y. Proskuryakov, K. Durose, G. Zoppi, and I. Forbes. Control of grain size in sublimation-grown CdTe, and the improvement in performance of devices with systematically increased grain size. *Solar Energy Materials and Solar Cells*, 94(6):1107–1112, 2010.

[116] W. K. Metzger, S. Grover, D. Lu, E. Colegrove, J. Moseley, C. L. Perkins, X. Li, R. Mallick, W. Zhang, and R. Malik. Exceeding 20% efficiency with in situ group V doping in polycrystalline CdTe solar cells. *Nature Energy*, 4(10):837–845, 2019.

[117] Y. Yin, R. M. Rioux, C. K. Erdonmez, S. Hughes, G. A. Somorjai, and A. P. Alivisatos. Formation of hollow nanocrystals through the nanoscale kirkendall effect. *Science*, 304(5671):711–714, 2004.

[118] C. Li, J. Poplawsky, N. Paudel, T. J. Pennycook, S. J. Haigh, M. Al-Jassim, Y. Yan, and S. J. Pennycook. S–Te interdiffusion within grains and grain boundaries in CdTe solar cells. *IEEE Journal of Photovoltaics*, 4(6):1636–1643, 2014.

[119] T. A. Fiducia, A. H. Munshi, K. Barth, D. Proprentner, G. West, W. S. Sampath, and J. M. Walls. Defect tolerance in as-deposited selenium-alloyed cadmium telluride solar cells. In *2018 IEEE 7th World Conference on Photovoltaic Energy Conversion (WCPEC)(A Joint Conference of 45th IEEE PVSC, 28th PVSEC & 34th EU PVSEC)*, pages 0127–0130. IEEE, 2018.

[120] E. Colegrove, X. Zheng, T. Ablekim, J. N. Duenow, C. L. Perkins, H. R. Moutinho, and W. K. Metzger. Se diffusion in CdTe thin films for photovoltaics. *Journal of Physics D: Applied Physics*, 54(2):025501, 2020.

[121] Y. Mishin. Solute drag and dynamic phase transformations in moving grain boundaries. *Acta Materialia*, 179:383–395, 2019.

[122] J. W. Cahn. The impurity-drag effect in grain boundary motion. *Acta metallurgica*, 10(9):789–798, 1962.

[123] R. K. Koju and Y. Mishin. Direct atomistic modelling of solute drag by moving grain boundaries. *Acta Materialia*, 198:111–120, 2020.

[124] H. Nakajima. The discovery and acceptance of the kirkendall effect: The result of a short research career. *JoM*, 49:15–19, 1997.

[125] S. Collins, C. A. Hsu, V. Palekis, A. Abbas, M. Walls, and C. Ferekides. Se profiles in CST films formed by annealing cdte/cdse bi-layers. In *2018 IEEE 7th World Conference on Photovoltaic Energy Conversion (WCPEC)(A Joint Conference of 45th IEEE PVSC, 28th PVSEC & 34th EU PVSEC)*, pages 0114–0118. IEEE, 2018.

[126] M. Merano, S. Sonderegger, A. Crottini, S. Collin, P. Renucci, E. Pelucchi, A. Malko, M. H. Baier, E. Kapon, and B. Deveaud. Probing carrier dynamics in nanostructures by picosecond cathodoluminescence. *Nature*, 438(7067):479–482, 2005.

[127] Fluorescence lifetime techniques: TCSPC, FRET, TRES, and SSTD. `https://www.horiba.com/rus/scientific/technologies/fluorescence-spectroscopy/fluorescence-lifetime-techniques/`. Accessed: 2023-02-14.

[128] M. Hastenrath, L. J. Balk, K. Löhnert, and E. Kubalek. Time resolved cathodoluminescence in the scanning electron microscope by use of the streak technique. *Journal of Microscopy*, 118(3):303–308, 1980.

[129] C. P. Welsch, H. H. Braun, E. Bravin, R. Corsini, S. Döbert, T. Lefèvre, F. Tecker, P. Urschütz, B. Buonomo, and O. Coiro. Longitudinal beam profile measurements at CTF3 using a streak camera. *Journal of Instrumentation*, 1(09):P09002, 2006.

[130] P. Horodyskỳ and P. Hlídek. Free-exciton absorption in bulk CdTe: temperature dependence. *physica status solidi (b)*, 243(2):494–501, 2006.

[131] T. Ablekim, J. N. Duenow, C. L. Perkins, J. Moseley, X. Zheng, T. Bidaud, B. Frouin, S. Collin, M. O Reese, and M. Amarasinghe. Exceeding 200 ns lifetimes in polycrystalline CdTe solar cells. *Solar RRL*, 5(8):2100173, 2021.

[132] J. Crank. *The mathematics of diffusion*. Oxford university press, 1979.

[133] G. Fonthal, L. Tirado-Mejıa, J. I. Marın-Hurtado, H. Ariza-Calderón, and J. G. Mendoza-Alvarez. Temperature dependence of the band gap energy of crystalline CdTe. *Journal of Physics and Chemistry of Solids*, 61(4):579–583, 2000.

[134] A. Wang, C. Li, J. Zhang, L. Wu, W. Wang, and L. Feng. Annealing temperature dependence of properties of CdSe thin films by RF-sputtering. In *IOP Conference Series: Materials Science and Engineering*, volume 556, page 012006. IOP Publishing, 2019.

[135] M. Lingg, A. Spescha, S. G. Haass, R. Carron, S. Buecheler, and A. N. Tiwari. Structural and electronic properties of CdTe1-xSex films and their application in solar cells. *Science and technology of advanced materials*, 19(1):683–692, 2018.